

DENMARK STRAIT OCEAN CIRCULATION VARIABILITY

by

Mattia Almansi

A dissertation submitted to The Johns Hopkins University
in conformity with the requirements for the degree of
Doctor of Philosophy

Baltimore, Maryland

March 2020

© 2020 by Mattia Almansi

All rights reserved

Abstract

Ocean currents affecting the global climate are sustained by cold and dense water that sinks in the North Atlantic Ocean. A large portion of this water overflows through Denmark Strait, the channel located between Greenland and Iceland. This thesis investigates the physical processes controlling the variability of the circulation in the vicinity of Denmark Strait. As direct measurements are not sufficient to unravel most of these processes, we develop a realistic general circulation model covering the East Greenland shelf and adjacent deep ocean. The model hydrography and circulation agree well with available observations. We find that the yearly mean southward volume flux of dense water is about 30% greater in the presence of mesoscale features known as boluses and pulses. We establish the causal relationship between these features and overflow cyclones observed further south. Most of the cyclones form at the Denmark Strait sill during overflow surges and grow as they move equatorward. A fraction of the cyclones form south of the sill, when anticyclonic vortices formed during high-transport events start collapsing. Finally, the model reveals that the eddy activity north of Denmark Strait regulates the bifurcation of the southward current along the eastern coast of Greenland and the offshore transport of fresh water at the surface.

Thesis Committee

Primary Readers

Thomas W. N. Haine (Primary Advisor)

Professor

Morton K. Blaustein Department of Earth and Planetary Sciences
Johns Hopkins Krieger School of Arts and Sciences

Anand Gnanadesikan

Professor and Chair

Morton K. Blaustein Department of Earth and Planetary Sciences
Johns Hopkins Krieger School of Arts and Sciences

Alternate Reader

Darryn W. Waugh

Professor

Morton K. Blaustein Department of Earth and Planetary Sciences
Johns Hopkins Krieger School of Arts and Sciences

Acknowledgments

First and foremost, I am deeply grateful to my advisor Tom Haine. When I started to work on this thesis, Tom told me, “Think creatively! Be ambitious!” His enthusiasm for science inspired me throughout my PhD and will continue to do so in the future. Marcello Magaldi also played a crucial role. I first became fascinated by the physics of the ocean while working with Marcello in Genova.

I would like to thank Renske Gelderloos, Bob Pickart, Lisbeth Håvik, Anand Gnanadesikan, and Darryn Waugh for inspiring conversations that greatly improved this thesis. I would also like to thank Aleksi Nummelin, Ali Siddiqui, Atousa Saberi, and Miguel Jimenez-Urias for countless stimulating discussions.

Funding sources include the Morton K. Blaustein Department of Earth and Planetary Sciences and the Institute for Data Intensive Engineering and Science (IDIES) at Johns Hopkins University, and the National Science Foundation (NSF) grants number OCE-1433448, OCE-1633124, and OAC-1835640.

To my family, Giulia, and friends from all around the world: Thank you! This would not have been possible without your support. I can’t wait to celebrate with you all!

Table of Contents

Table of Contents	v
List of Tables	viii
List of Figures	ix
List of Acronyms	xxii
1 Introduction	1
1.1 Global relevance of the Denmark Strait Overflow Water	3
1.2 Local circulation in Denmark Strait	5
1.3 Dynamics associated with the Denmark Strait Overflow	8
1.4 Data accessibility: OceanSpy	10
1.5 Outline	11
2 Mesoscale anomalies associated with overflow surges at the sill	13
2.1 Introduction	14
2.2 Materials and methods	16
2.2.1 Numerical setup	16

2.2.2	Validation	19
2.2.3	Detection of mesoscale anomalies	24
2.3	Results	28
2.3.1	Statistics of mesoscale anomalies	28
2.3.2	Time evolution of mesoscale anomalies	31
2.3.3	Spatial evolution of mesoscale anomalies	35
2.4	Summary and discussion	39
3	Evolution of overflow surges south of the strait	43
3.1	Introduction	44
3.2	Materials and methods	49
3.2.1	Numerical setup	49
3.2.2	Vortex detection scheme	50
3.2.3	Identification of high-transport events	55
3.3	Results	57
3.3.1	Relationship between DSO cyclones and overflow surges	57
3.3.2	Downstream evolution of DSO cyclones	64
3.4	Summary and discussion	68
4	East Greenland Current variability north of the strait	71
4.1	Introduction	72
4.2	Comparison with observations	75
4.2.1	The Kögur mooring array	75

4.2.2	Historical hydrographic profiles	77
4.3	Results	80
4.3.1	Relationship between eddy activity and temperature of the intermediate layer	80
4.3.2	Relationship between eddy activity and salinity of the surface layer	84
4.4	Summary and discussion	87
5	Conclusions	90
5.1	Summary	90
5.2	Future Work	93
	References	99
	Curriculum Vitae	115

List of Tables

- 2.1 Summary of boluses and pulses mean properties and thresholds. 40

List of Figures

- 1.1 Schematic along-strait vertical section showing the **Denmark Strait Overflow (DSO)** and sill. The viewer is looking from east (Iceland) to west (Greenland). The red pin on the map indicates Denmark Strait. Source: National Ocean Service website, <https://oceanservice.noaa.gov/facts/largest-waterfall.html>, accessed on January 8, 2020. 2
- 1.2 A simplified schematic of the **Atlantic Meridional Overturning Circulation (AMOC)**. Warm water flows north in the upper ocean (red), gives up heat to the atmosphere (atmospheric flow gaining heat represented by changing color of broad arrows), sinks, and returns as a deep cold flow (blue). Source: Srokosz and Bryden, 2015. 4

1.3	Schematic circulation in the region of the Blosseville Basin, upstream of the Denmark Strait sill, as proposed by Våge et al., 2011 and Våge et al., 2013. Shown in blue are the three proposed pathways of overflow water to the sill: the shelfbreak East Greenland Current (EGC), separated EGC, and North Icelandic Jet (NIJ). The overturning cell proposed by Våge et al., 2011 is also shown. The locations of the moorings in the Kögur array are indicated by the black dots. Source: Harden et al., 2016 . . .	7
1.4	Schematic of the physical processes acting in overflows. Source: Legg et al., 2009.	9
2.1	(a) Plan view of the numerical domain superimposed on seafloor bathymetry. Red lines bound the 2-km resolution area. The Látrabjarg Line (LL) is drawn in magenta. (b) Schematic of the currents flowing in the 2-km resolution area highlighted in (a). Red (blue) stands for warm (cold) currents. Acronyms: East Greenland Current (EGC); North Icelandic Jet (NIJ); North Icelandic Irminger Current (NIIC); Irminger Current (IC) . . .	16
2.2	Time-mean vertical sections obtained from (left) observations (Mastropole et al., 2017) and (right) model outputs: (a, b) potential temperature; (c, d) salinity; (e, f) Brunt-Väisälä frequency. Grey contours represent the potential density anomaly in kg m^{-3} . The DSO interface is highlighted in magenta. . . .	20

2.3	(a) Data coverage of the vertical sections. Anomalies of (b) potential temperature, (c) salinity, and (d) potential density for the regular minus the uneven sampling.	23
2.4	Vertical sections of (a) absolute geostrophic velocity measured in October 2008 (Våge et al., 2011), (b) monthly mean model velocity of October 2007, and (c) mean model velocity on October 1st, 2007.	25
2.5	Comparison of (a) SSH and (b) DSO interface during boluses (orange), pulses (green), and background state (magenta). Black dashed lines bound the region from 15 km west to 15 km east of the deepest part of the sill. Negative (positive) distances correspond to northwest (southeast) of the sill. The viewer is looking to the north.	26
2.6	Composite of boluses minus background state Brunt-Väisälä frequency (N^2). The orange (magenta) line corresponds to the composite of boluses (background state) DSO interface.	28
2.7	Mean velocity of the DSO between 15 km west and 15 km east of the sill in the composites of boluses (orange), pulses (green), and background state (magenta). The thick black line corresponds to the direction of the LL (cross strait).	29

2.8	Seasonality of boluses and pulses. Green (orange) bars show the number of pulses (boluses) in a season. Black bars show the seasonal distribution of boluses + pulses. The numbers on the top of the bars indicate the percentage of boluses, pulses, or boluses + pulses, respectively. The 3-month acronyms for seasons are: September-October-November (SON) ; December-January-February (DJF) ; March-April-May (MAM) ; June-July-August (JJA)	30
2.9	Time evolution of the composites of representative (left) boluses and (right) pulses obtained by averaging (a, b) potential temperature and (c, d) salinity over the area between 15 km west and 15 km east of the sill. The time axis is normalized to the length of the events (57.1 ± 10 h for boluses and 27.5 ± 15.4 h for pulses). The potential density contours are drawn in gray and the DSO interface is highlighted in magenta.	32
2.10	As in Figure 2.9 , but for (a, b) along-stream velocity and (c, d) cross-stream velocity. The along-stream direction for boluses and pulses is defined as the orientation of the mean velocity vectors in Figure 2.7 . Zero velocity contours are drawn in black.	33

2.11	Composites of (left) boluses and (right) pulses minus the background state: (a, b) potential temperature and (c, d) along-strait velocity. Positive velocities are equatorward. The DSO interface during boluses (orange), pulses (green), and background state (magenta) are outlined. Gray contours bound the northward flow at the Iceland shelfbreak during the background state, whereas black contours bound the northward flow during boluses in (c) and pulses in (d).	35
2.12	Composites of DSO interface during (a) boluses and (b) pulses minus the background state. Black contour lines show the SSH composite during boluses and pulses minus the background state (cm). The bathymetric contours (m) are shown in gray. The Látrabjarg Line (LL) is drawn in magenta and the black cross corresponds to the sill. Regions where the entire water column is lighter than the overflow water are masked white. Negative (positive) anomalies correspond to a shallower (deeper) DSO compared to the background state.	36
3.1	Infrared imagery of sea surface temperature on September 24, 1990. Accompanying sketch shows location and shape of eddies and seafloor depth contours in meters. The Denmark Strait sill is at upper right. Source: Bruce, 1995.	44

3.2	Cartoon of the stretching process leading to the generation of cyclonic vorticity. h is the height of the water column, ζ is the relative vorticity, Ro is the Rossby number, and f is the vertical component of the Coriolis parameter. Source: von Appen, 2013.	46
3.3	Seafloor bathymetry in the region of interest for this study. Red lines bound the area fed to the vortex detection algorithm shown in Figure 3.5. Circles indicate the stations along the DSO path (Koszalka et al., 2017). Circles colored in magenta, white, blue, and green indicate where the DSO path crosses hydrographic sections known as the Látrabjarg Line (LL; magenta line), Denmark Strait South (DSS), Transient Tracers in the Ocean (TTO), and Spill Jet (SJ), respectively.	48
3.4	Unfiltered locations of the centers of the detected cyclones (a) and anticyclones (b). The color code indicates the mean nondimensional relative vorticity ($\overline{f^{-1}\zeta}$) of the vortices. ζ has been extracted along the σ -level at a depth of $5H/8$. Black contours show the seafloor depth in meters. The color code convention of the DSO stations is the same used in Figure 3.3.	54
3.5	Location of the centers of the filtered vortices color-coded by their mean nondimensional relative vorticity ($\overline{f^{-1}\zeta}$) at a depth of $5H/8$. Black contours show the bathymetry in meters. Black dashed lines bound the region shown in Figure 3.3. The color code and labeling conventions of the DSO stations are the same used in Figure 3.4.	56

3.6	Seasonal frequency of occurrence of (a) boluses and cyclones, and (b) pulses and anticyclones. Red (blue) hatched bars show the percentage of cyclones (anticyclones) detected in a season compared to the total number of cyclones (anticyclones). Orange (green) bars show the frequency of occurrence of boluses (pulses). The 3-month acronyms for seasons are: September-October-November (SON) ; December-January-February (DJF) ; March-April-May (MAM) ; June-July-August (JJA)	57
3.7	Relative vorticity (a, c) and instantaneous potential density minus the yearly mean (b, d) during a bolus and a pulse. The bolus (a, b) crossed the LL (drawn in magenta) on April 27th, 2008 at midnight. The pulse (c, d) was detected in Denmark Strait on January 30th, 2008 at noon. Dark gray contours indicate the seafloor depth in meters. Dashed lines bound the vortices detected. Fields have been extracted along the σ -level at a depth of $5H/8$	59
3.8	Composite vertical sections along the LL of cyclones (anticyclones) detected within 48 hours from overflow surges minus the yearly averages are shown in the left (right) column: (a and b) potential density; (c and d) along-strait velocity (orthogonal to the LL); (e and f) cross-strait velocity (tangential to the LL). The viewer is looking to the north: Positive along-strait (cross-strait) velocities are towards the pole (Iceland). The dashed line corresponds to the σ -level at a depth of $5H/8$	61

3.9 Nondimensional relative vorticity ($f^{-1}\zeta$) and velocity vectors extracted along the σ -level at a depth of $5H/8$. The region shown is bounded by black dashed lines in Figure 3.5. Labeled circles correspond to the DSO stations. Three consecutive snapshots (a, c, and e) following the pulse in Figures 3.7c and 3.7d, and composites of thirty anticyclonic events (b, d, and f) are shown. The composite of Stage II (d) includes the snapshots where anticyclones have been detected near station #03. The stages are six hours apart. Dark gray contours indicate the seafloor depth in meters. 63

3.10 Composites of area-weighted mean (a) nondimensional relative vorticity and (b) vertical velocity along the DSO path. Positive (negative) vertical velocities correspond to upwelling (downwelling). Lines in black (a, b) correspond to composites of DSO cyclones. Blue and red lines correspond to composites in the regions of the vortices 6 hours before and after the detection, respectively. Error bars represent the area-weighted standard deviation. Labeled circles correspond to composites of yearly averages in the regions of the vortices (background state). The color code and labeling convention of the DSO stations are the same as used in Figure 3.5. Fields have been extracted along the σ -level at a depth of $5H/8$ 65

3.11 Composites of area-weighted mean Ertel Potential Vorticity (green, left vertical axis) and Brunt-Väisälä frequency (orange, right axis) along the DSO path. Error bars represent the area-weighted standard deviation. Fields have been extracted along the σ -level at a depth of $5H/8$	67
4.1 Schematic overview of the currents flowing across the Kögur mooring array marked by the orange line between Greenland and Iceland. The abbreviations are East Greenland Current (EGC), North Icelandic Jet (NIJ), North Icelandic Irminger Current (NIIC).	73

4.2 Comparison of the mean cross-sectional current speed in (a) the mooring observations and (b) the model at Kögur (see Figure 4.1). Positive current speeds are toward the southwest and distance is increasing along the x -axis from the easternmost mooring near the Iceland shelfbreak. On top of (a) the mooring locations are numbered (KGA 1-12), and the measurement levels on each mooring are marked by black dots. A selection of isopycnals is contoured in both panels, and the upper limit of DSOW, the 27.8 kg m^{-3} isopycnal, is marked by the thick black contour. The horizontal dashed line indicates the sill depth at Denmark Strait (650 m), and the vertical dashed lines mark the location where the orientation of the transect changes. The data from the mooring array are interpolated using a Laplacian-spline interpolator, and the data from the model are linearly interpolated in the horizontal. The viewer is looking to the north. 76

- 4.3 Maximum temperature of the Atlantic-origin Water along the 700-m East Greenland isobath averaged over 3-month periods. The black solid line corresponds to the yearly averaged temperatures. The red line is the linear fit of the yearly averaged temperatures. Larger distances correspond to higher latitudes, as shown by the vertical lines. The dashed vertical line marks the latitude of the Kögur section. The 3-month acronyms for seasons are: **September-October-November (SON)**; **December-January-February (DJF)**; **March-April-May (MAM)**; **June-July-August (JJA)**. 78
- 4.4 Temperature anomalies from the annual mean in (a) **March-April-May (MAM)** and (b) **June-July-August (JJA)** in the model at Kögur. (c) and (d) show the cross-sectional current speed in **MAM** and **JJA**, respectively. A selection of isopycnals is contoured in all panels, and the upper limit of the **DSOW** is marked by the thick black contour. The vertical dashed lines mark the location where the orientation of the transect changes (see Figure 4.1). The horizontal dashed lines mark the depth of the Denmark Strait sill. The viewer is looking to the north. . . 79

- 4.5 (a) Average temperature of the Atlantic-origin Water along the shelfbreak EGC path computed for water warmer (red) and colder (blue) than a range of local percentiles (color bar), and (b) corresponding EKE. The black solid line in (a) is the linear fit of the yearly averaged temperatures. Larger distances correspond to higher latitudes, as shown by the vertical lines. The dashed vertical lines mark the latitude of the Kögur section. 81
- 4.6 Cross-sectional current speed at Kögur during (a) the warm mode and (b) the cold mode in the model. (c) and (d) show the EKE during the warm and cold modes, respectively. Note the nonlinear color bar in (c) and (d). A selection of isopycnals is contoured in all panels, and the upper limit of the DSOW is marked by the thick black contour. The vertical dashed lines mark the location where the orientation of the transect changes (see Figure 4.1). The horizontal dashed lines mark the depth of the Denmark Strait sill. The viewer is looking to the north. . . 83
- 4.7 Mean (a) horizontal current speed $\left(\sqrt{u^2 + v^2}\right)$, (b) salinity, (c) EKE, and (d) Pearson correlation coefficient between salinity and EKE in the model over the upper 100 m. The black lines indicate the location of the Kögur transect. The gray contours are 300-, 700-, 1000-, and 2000-m isobaths from the model. Areas shallower than 100 m are masked gray. Hatched areas are not significant at the 5% level (p values < 0.005). 85

5.1	Plan view of the numerical domain of the model in support of the IGP superimposed on seafloor bathymetry. Red lines indicate the square root of the horizontal area of the grid-cells in kilometers.	94
5.2	(left) The hydrographic sections occupied in the Iceland Greenland Seas Project (IGP). (right) The northwest Iceland Sea and the location of intensive surveys where triangular patterns or lines were repeated several times in coordination with the research aircraft. Source: Renfrew et al., 2019.	95
5.3	Monthly mean cross-sectional current speed in (a) February and (b) March at the Kögur section. The monthly mean NAO is positive in February and negative in March. Positive current speeds are toward the southwest. The vertical dashed lines mark the location where the orientation of the transect changes (see Figure 4.1). The viewer is looking to the north.	98

List of Acronyms

- AABW** Antarctic Bottom Water. 5
- AIW** Arctic Intermediate Water. 45
- AMOC** Atlantic Meridional Overturning Circulation. ix, 3–5, 74, 92
- ASR** Arctic System Reanalysis. 49, 74, 96
- CAO** Cold-Air Outbreak. 97
- DJF** December-January-February. xii, xv, xix, 30, 57, 78
- DSO** Denmark Strait Overflow. ix–xiv, xvi, xvii, 1–3, 6, 8, 10–15, 20, 26–30, 32, 35–41, 43–45, 47–56, 60, 62, 64–70, 75, 77, 90–93
- DSOW** Denmark Strait Overflow Water. xviii–xx, 1, 5, 6, 8, 10, 12, 24, 34, 37, 45, 71, 72, 74, 76, 79, 80, 83, 89, 92, 93, 97
- DSS** Denmark Strait South. xiv, 48, 64, 67
- EGC** East Greenland Current. x, xvii, xx, 6–8, 12, 16, 21, 45, 71–75, 77–82, 84, 86–88, 92, 93, 97
- EKE** Eddy Kinetic Energy. xx, 80–88, 92

ERA ECMWF Re-Analysis. 18, 50, 96

FDR False Discovery Rate. 86

HYCOM HYbrid Coordinate Ocean Model. 17, 18

IBCAO International Bathymetric Chart of the Arctic Ocean. 17

IC Irminger Current. x, 16

IGP Iceland Greenland Seas Project. xxi, 94–97

JJA June-July-August. xii, xv, xix, 30, 57, 78–80

LL Látrabjarg Line. x, xi, xiii–xv, 16, 19, 22, 24, 29, 35, 36, 48, 55, 57–61, 64

LNADW Lower North Atlantic Deep Water. 5

MAM March-April-May. xii, xv, xix, 30, 57, 78–80

MITgcm Massachusetts Institute of Technology General Circulation Model.
16, 18, 93

NADW North Atlantic Deep Water. 3, 5

NAO North Atlantic Oscillation. xxi, 8, 96–98

NCODA Navy Coupled Ocean Data Assimilation. 18

NIIC North Icelandic Irminger Current. x, xvii, 8, 16, 24, 38, 41, 60, 73, 75, 80

NIJ North Icelandic Jet. x, xvii, 6–8, 16, 42, 73, 75, 77, 97

OSTIA Operational Sea Surface Temperature and Sea Ice Analysis. 18

OW Okubo-Weiss. 50–52, 68

PSW Polar Surface Water. 72, 86–88

PV Potential Vorticity. xvii, 43, 45, 47, 64, 66–70

Ro Rossby number. xiv, 46

SJ Spill Jet. xiv, 45, 48, 52, 55, 70

SON September-October-November. xii, xv, xix, 30, 57, 78

SSH Sea Surface Height. xi, xiii, 26, 27, 36, 38, 41, 91

TOPAZ Towards an Operational Prediction System for the North Atlantic
European Coastal Zones. 18

TTO Transient Tracers in the Ocean. xiv, 48

Chapter 1

Introduction

Denmark Strait is an ocean channel located between Greenland and Iceland (red pin in Figure 1.1). Although it has a sill depth of just about 650 meters and is only approximately 300 kilometers wide, it plays a key role in the global climate system. Its global importance is primarily due to the [Denmark Strait Overflow \(DSO\)](#), a bottom-trapped current transporting dense water from the Nordic Seas to the subpolar North Atlantic. This overflow is the largest waterfall on Earth (Figure 1.1). After crossing Denmark Strait, the [Denmark Strait Overflow Water \(DSOW\)](#) is colder and denser than the surrounding water and sinks into the deep Irminger Basin. This sinking water is one of the drivers of the thermohaline circulation, a critical system of ocean currents redistributing water and heat on a global scale. Knowing the mechanisms associated with the circulation in Denmark Strait is of key importance for understanding and predicting Earth's climate. Additionally, Denmark Strait is a critical gateway for strategic, political, and economic reasons (["The GIUK Gap's strategic significance" 2019](#)). For example, the hydrography and circulation in the strait affect the marine ecosystem (Astthorsson et al., 2007), and

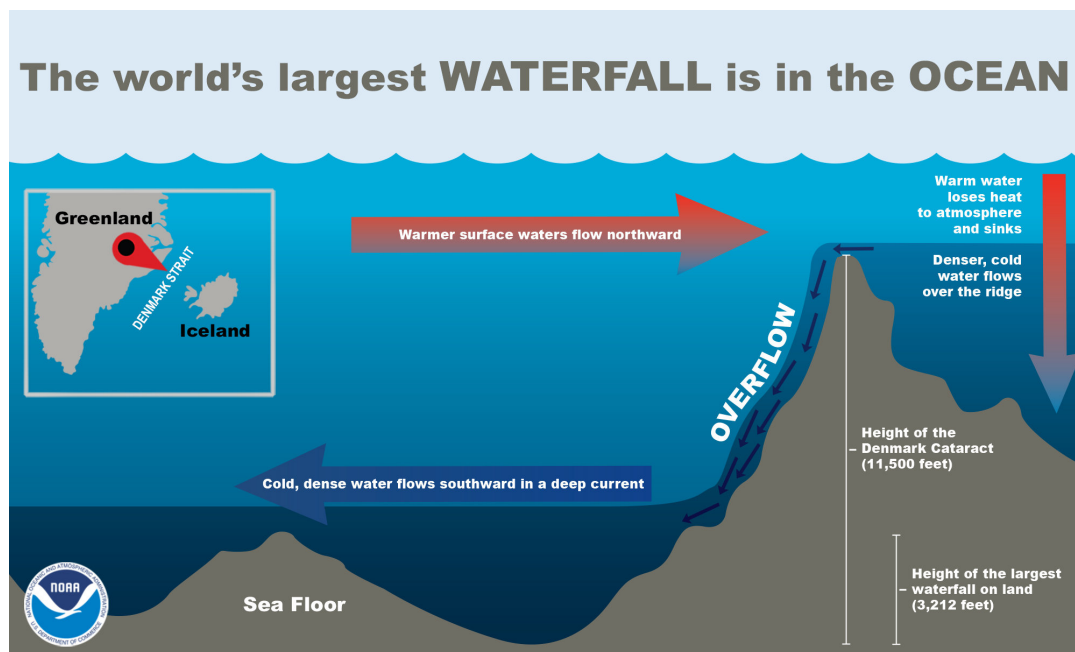


Figure 1.1: Schematic along-strait vertical section showing the Denmark Strait Overflow (DSO) and sill. The viewer is looking from east (Iceland) to west (Greenland). The red pin on the map indicates Denmark Strait. Source: National Ocean Service website, <https://oceanservice.noaa.gov/facts/largest-waterfall.html>, accessed on January 8, 2020.

therefore the coastal communities relying on fisheries (Hamilton et al., 2004).

Large freshwater anomalies (i.e., freshening) have been recently observed in the Arctic Ocean (Haine et al., 2015). However, the current/future global impacts of these changes are hard to assess/predict because the knowledge of the mechanisms controlling the circulation in the subpolar North Atlantic is limited. The numerous open questions about the DSO dynamics motivate this thesis. As direct measurements are not sufficient to unravel most of the underlying physical processes, available observations must be integrated with numerical models. The main goal of this thesis is therefore to design a high-resolution, realistic general circulation model and use it to advance the understanding of the circulation in Denmark Strait.

1.1 Global relevance of the Denmark Strait Overflow Water

The North Atlantic Deep Water (NADW) is the major input of dense water sustaining the Atlantic Meridional Overturning Circulation (AMOC), which refers to the thermohaline circulation in the Atlantic Ocean (Figure 1.2). This dense water is the result of convective and mixing processes occurring in the Arctic Ocean and the Nordic Seas (the Arctic Mediterranean Sea; Aagaard et al., 1985). The AMOC is governed by both wind-driven and buoyancy-driven processes (Kuhlbrodt et al., 2007). The former process causes water masses to rise from the bottom of the ocean to the surface (upwelling), whereas the latter causes dense water formed at the surface to sink into the deep ocean (downwelling). The loop is closed by surface currents transporting relatively



Figure 1.2: A simplified schematic of the Atlantic Meridional Overturning Circulation (AMOC). Warm water flows north in the upper ocean (red), gives up heat to the atmosphere (atmospheric flow gaining heat represented by changing color of broad arrows), sinks, and returns as a deep cold flow (blue). Source: Srokosz and Bryden, 2015.

light water towards the pole and deep currents transporting dense water towards the equator. These currents have a large impact on Earth's climate. For example, the heat transported northward by the warm currents in the North Atlantic is one of the mechanisms responsible for the mild climate of northwestern Europe (Saenko, 2009).

The hydrographic properties of the **NADW** are of critical importance because they determine the **AMOC** response to the ongoing climate change. Four main water masses contribute to the **NADW** (Dickson and Brown, 1994): (i) the Labrador Sea Water; (ii) the water overflowing on the eastern side of Iceland through the Faroe Bank Channel; (iii) the water overflowing through Denmark Strait; (iv) the **Lower North Atlantic Deep Water (LNADW)**. The latter forms from a portion of **Antarctic Bottom Water (AABW)** which crosses the equator and gradually warms, mixes, and shoals. A major role is played by the **DSOW**, as it is the coldest and densest contributor to the **NADW** (Swift et al., 1980). Before entering the global thermohaline circulation, the **DSOW** is modified by several local processes taking place in the Nordic and Irminger Seas, such as air-sea interaction, mixing, and entrainment. The **DSOW** is the most sensitive outflow to environmental changes induced at the sea surface (Swift, 1984; Livingston et al., 1985) and it quickly transfers atmospheric signals to the deep ocean Strass et al., 1993.

1.2 Local circulation in Denmark Strait

Through the years, many studies have been designed to better understand the origins, pathways, and residence times of the dense water entering the global

thermohaline circulation through Denmark Strait. The **DSOW** is commonly defined as a mixture of different water masses with a resulting potential density anomaly of more than 27.8 kg m^{-3} ($\sigma_\theta = \rho - 1000 \text{ kg m}^{-3}$; Dickson and Brown, 1994). In the deepest part of the Denmark Strait trough, the overflow is almost completely composed of dense Arctic-origin water, while less dense Atlantic-origin water and polar surface water contribute to the remainder of the overflow layer (Mastropole et al., 2017).

The **DSO** volume flux (transport) is estimated to be $3.2 \pm 1.5 \text{ Sv}$ close to the sill ($1 \text{ Sv} \equiv 10^6 \text{ m}^3 \text{ s}^{-1}$; Jochumsen et al., 2017), and increases by entrainment as the **DSO** moves southward. The **DSOW** accounts for approximately half of the overflow water export from the Nordic Seas to the subpolar North Atlantic (Dickson and Brown, 1994; Hansen et al., 2016; Jochumsen et al., 2017; Østerhus et al., 2019). Two major currents contribute to the **DSO** transport at the sill (Figure 1.3): (i) the **East Greenland Current (EGC)** system; (ii) the **North Icelandic Jet (NIJ)**. The former involves two separate branches (Våge et al., 2013): (i) the shelfbreak **EGC**; (ii) the separated **EGC**. The shelfbreak **EGC** (Strass et al., 1993) originates north of Fram Strait and continues southward along the East Greenland shelf toward the southern tip of Greenland. Then, it bifurcates at the northern end of Blossville basin forming the separated **EGC** (Våge et al., 2013), which flows southward along the base of the Iceland slope. The entire **EGC** system contributes about two thirds of the **DSO** transport at the sill (Harden et al., 2016). The remaining third of **DSOW** is transported primarily by the **NIJ** (Jonsson and Valdimarsson, 2004; Semper et al., 2019), a recently discovered current that flows towards Denmark Strait along the north

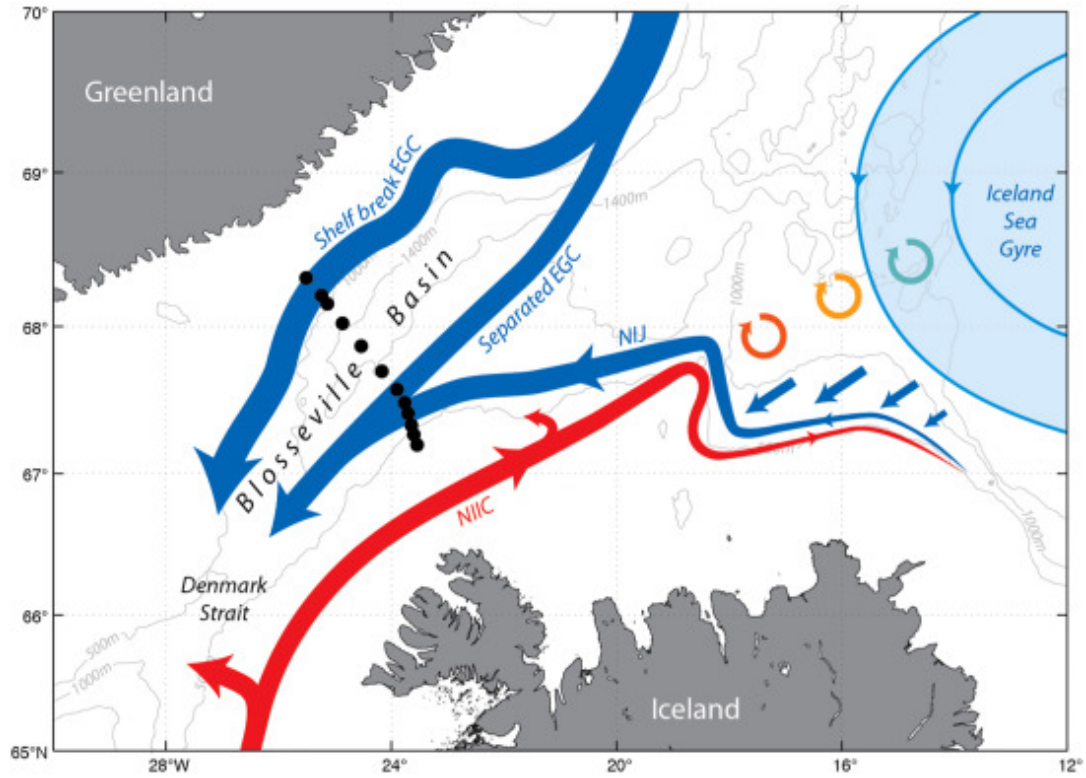


Figure 1.3: Schematic circulation in the region of the Blosseville Basin, upstream of the Denmark Strait sill, as proposed by Våge et al., 2011 and Våge et al., 2013. Shown in blue are the three proposed pathways of overflow water to the sill: the shelfbreak East Greenland Current (EGC), separated EGC, and North Icelandic Jet (NIJ). The overturning cell proposed by Våge et al., 2011 is also shown. The locations of the moorings in the Kögur array are indicated by the black dots. Source: Harden et al., 2016

side of Iceland. The separated EGC and the NIJ partly merge near the Kögur transect and the combined flow follows the deep part of the Iceland slope. Other contributors to the DSOW are the poleward flowing North Icelandic Irminger Current (NIIC), and a pathway identified south of Iceland along the Iceland shelf (Saberi et al., 2020). The latter is highly variable and supplied about one fourth of the DSOW in winter 2008, which had a relatively high North Atlantic Oscillation (NAO) index.

1.3 Dynamics associated with the Denmark Strait Overflow

The main physical processes associated with the DSO are shown in Figure 1.4. Due to the geometry of Denmark Strait, rotating hydraulics theory has been often applied to understand the overflow transport dynamics at the sill (e.g., Whitehead, 1998; Käse and Oschlies, 2000; Girton et al., 2001; Helfrich and Pratt, 2003; Käse et al., 2003; Nikolopoulos et al., 2003; Kösters et al., 2005; Macrandar et al., 2005; Wilkenskjeld and Quadfasel, 2005; Köhl et al., 2007). In these studies, the DSO is treated as a topographically restricted and hydraulically controlled flow, and the volume flux is believed to be modulated by the height of the dense water above the sill level and the density difference between the upstream and downstream water. Downstream of the sill, the DSO is bottom-trapped, entrains a large amount of ambient water, and accelerates (Jungclaus et al., 2001). The strong entrainment is the result of shear instability at the interface of the overflow, which is generated by the velocity difference between the fast DSO and the slow intermediate layer in

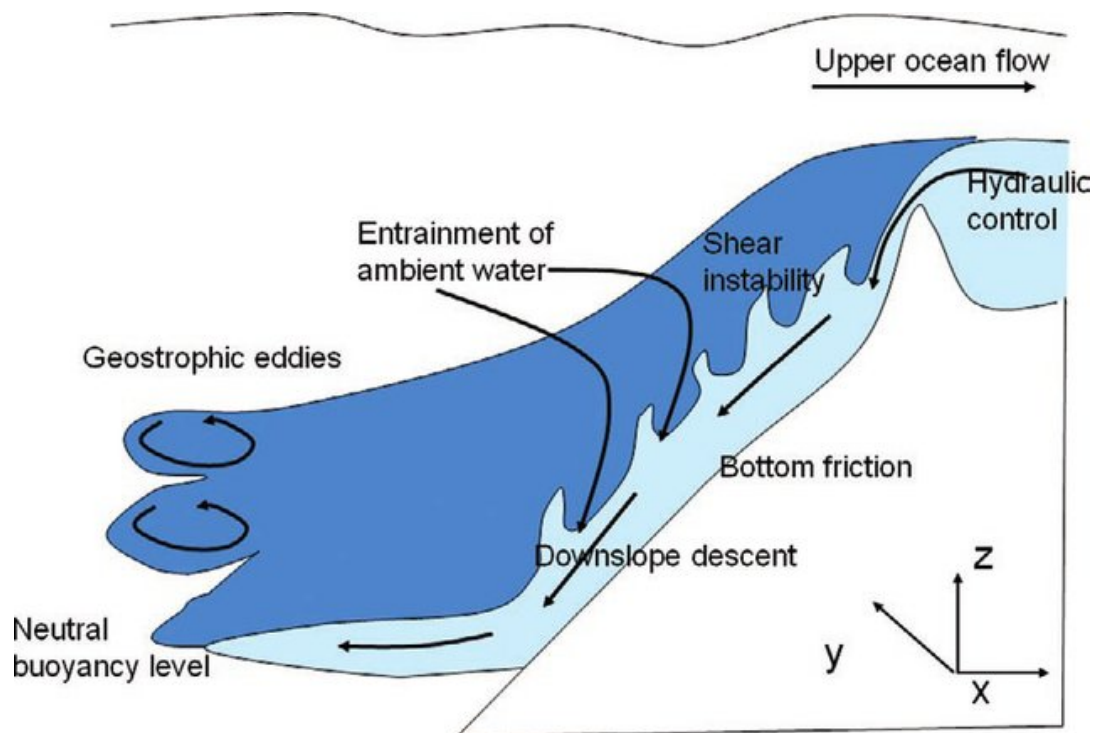


Figure 1.4: Schematic of the physical processes acting in overflows. Source: Legg et al., 2009.

contact with the overflow. Due to geostrophic constraints (balance between pressure gradient and Coriolis forces), the *DSO* tends to follow topographic contours (Legg et al., 2009). However, as the *DSO* is able to move downslope, these constraints are often broken either in the bottom Ekman layer or through baroclinic instability (Cenedese et al., 2004). As the *DSO* descend into the Irminger Basin, it eventually becomes neutrally buoyant. At this stage, the *DSOW* spreading into the ocean interior is enhanced by eddies resulting from baroclinic instability (Legg et al., 2006).

1.4 Data accessibility: OceanSpy

Simulations of ocean currents using numerical circulation models are becoming increasingly realistic. At the same time, these models generate increasingly large volumes of model output data. These trends make analysis of the model data harder for two reasons. First, researchers must use high-performance data-analysis clusters to access these large data sets. Second, they must post-process the data to extract oceanographically-useful information. Moreover, the increasing model realism encourages researchers to compare simulations to observations of the natural ocean. To achieve this task model data must be analyzed in the way observational oceanographers analyze field measurements; and, ideally, by the observational oceanographers themselves.

In order to address these needs we developed OceanSpy, an open-source and user-friendly Python package that enables scientists and interested amateurs to analyze and visualize oceanographic data sets. OceanSpy is published by the Journal of Open Source Software (Almansi et al., 2019). It can be

used as a standalone package for analysis of any general circulation model output, or it can be run on a remote data-analysis cluster, such as the Johns Hopkins University SciServer system (Medvedev et al., 2016). All of the data sets produced for this thesis are available on SciServer, and can be analyzed through OceanSpy to compare with oceanographic observations, and/or portray the kinematic and dynamic space-time properties of the circulation (see <https://oceanspy.readthedocs.io>).

1.5 Outline

We present the year-long, realistic, high-resolution ocean general circulation model designed for this thesis in Chapter 2. In this chapter, we use the model to study the high-frequency variability of the DSO at the sill. We aim to answer the following questions:

- How do the overall hydrography and circulation in the model compare with available observations in Denmark Strait?
- Is the observed high-frequency variability of the DSO well captured by the model?
- How do the hydrography and circulation in Denmark Strait change when overflow surges propagate through the region?

In Chapter 3, we use the model solutions to fill the gaps in the sparse measurements along the DSO path. We aim to better understand the nature of the DSO variability. The ultimate goal of this chapter is threefold:

- To further quantify the characteristics of the high frequency DSO fluctuations.
- To explore the dynamics associated with conservation of potential vorticity and stretching of the water column as the overflow descends from the sill.
- To characterize the life cycle of the so-called DSO cyclones as they progress into the Irminger Basin.

In Chapter 4, we use the model to support and extend an observational analysis focused on the Atlantic-origin Water in the EGC system. We aim to answer the following questions:

- Is there a relationship between the kinematics of the simulated EGC system and the processes altering the Atlantic-origin Water?
- Which dynamics control the variability of the EGC system and the bifurcation of the shelfbreak EGC?
- How does the separation of the EGC affect the properties of the DSOW entering the subpolar North Atlantic?

Finally, we summarize the major findings of this thesis and we provide a plan for future investigations in Chapter 5.

Chapter 2

Mesoscale anomalies associated with overflow surges at the sill

We present a year-long, realistic, high-resolution ocean general circulation model covering the East Greenland shelf, and the Iceland and Irminger Seas. The model is used to advance the understanding of the short-term variability of the [Denmark Strait Overflow \(DSO\)](#). First, we compare the numerical solutions to available observations. Then, we use the model to study [DSO](#) high-transport events occurring frequently at the sill. The hydrography and circulation in our model show good agreement with measurements taken in the vicinity of Denmark Strait. The numerical simulation indicates that mesoscale anomalies play a major role in controlling the amount of overflow water entering the Irminger Basin and its properties.

This chapter is published by the *Journal of Physical Oceanography* (Almansi et al., [2017](#)).

2.1 Introduction

Studies on the DSO transport (volume flux) have found no long-term trends (Jochumsen et al., 2012; Jochumsen et al., 2017). Although the annual mean transport of the DSO is steady, observations and numerical models show a pronounced high-frequency variability (from one day to one week at the sill; Ross, 1984; Macrander et al., 2007; Haine, 2010; von Appen et al., 2017). Using a large number of historical hydrographic sections occupied across Denmark Strait, together with 5 years of mooring data, Mastropole et al., 2017 and von Appen et al., 2017 described two dominant mesoscale features called “boluses” and “pulses”. Both of these features are associated with overflow surges at the sill.

The term bolus was first introduced by Cooper, 1955 and refers to a large lens of cold and weakly stratified overflow water that crosses Denmark Strait. The first direct attempt to observe the features described by Cooper, 1955 was carried out by Harvey, 1961. Mastropole et al., 2017 found that this features are very common and von Appen et al., 2017 found that they are associated with veering of the horizontal current: first toward Iceland, then toward the Irminger Sea, and finally toward Greenland. Numerous other observational and numerical data sets show the existence of these intermittent mesoscale features (e.g., Spall and Price, 1998; Rudels et al., 1999; Girton and Sanford, 2003; Käse et al., 2003; Haine, 2010; Magaldi et al., 2011; Koszalka et al., 2013; Koszalka et al., 2017). However, the mechanisms controlling their formation are still not understood.

The term pulse was introduced more recently by Bruce, 1995 to describe

an intermittent increase in bottom velocity in Denmark Strait. von Appen et al., 2017 demonstrated that these features propagate through the strait approximately every 5 days. Pulses are associated with backing of the horizontal current: first toward Greenland, then toward the Irminger Sea, and finally toward Iceland. The dynamics associated with pulses are also still unexplained.

The high temporal (6 h) and spatial (horizontal: 2-4 km; vertical: 1-15 m) resolutions of our realistic general circulation model allow us to investigate in detail the high-frequency DSO variability. This has not been possible in past models that are not able to properly resolve boluses and pulses. For example, the horizontal resolution used by Logemann et al., 2013 is about 7 km in Denmark Strait, whereas the vertical resolution used by Behrens et al., 2017 decreases from 6 m at the surface to 250 m at the bottom.

In this chapter we aim to answer the following questions: (i) How do the overall hydrography and circulation in our model compare with available observations in Denmark Strait? (ii) Is the observed high-frequency variability of the DSO well captured by the model? (iii) How do the hydrography and circulation in Denmark Strait change when boluses and pulses propagate through the region? The chapter is organized as follows: In Section 2.2, we present the high-resolution realistic simulation and we compare the model hydrography and circulation in Denmark Strait with previous observational results. We also describe the objective method designed to identify mesoscale features in the model. In Section 2.3 we provide significant statistics of boluses and pulses. We show their time evolution and we describe the spatial distribution

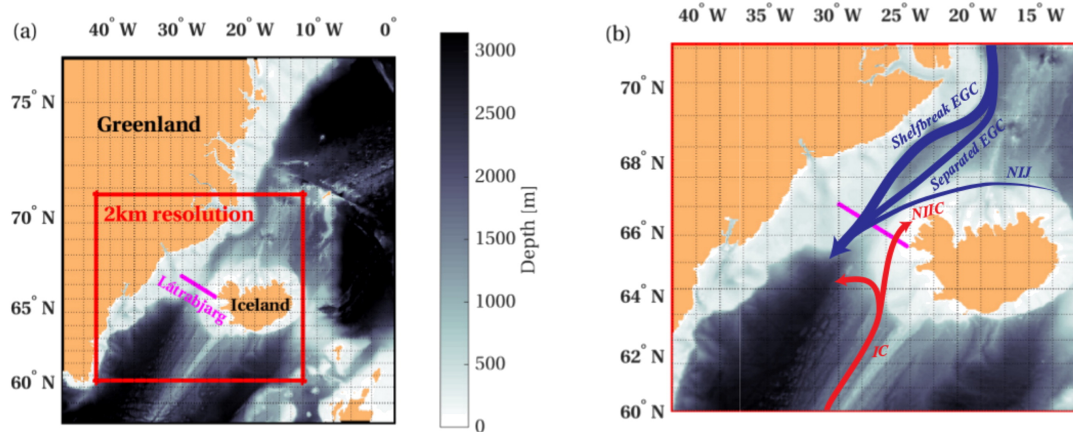


Figure 2.1: (a) Plan view of the numerical domain superimposed on seafloor bathymetry. Red lines bound the 2-km resolution area. The Látrabjarg Line (LL) is drawn in magenta. (b) Schematic of the currents flowing in the 2-km resolution area highlighted in (a). Red (blue) stands for warm (cold) currents. Acronyms: East Greenland Current (EGC); North Icelandic Jet (NIJ); North Icelandic Irminger Current (NIIC); Irminger Current (IC)

of the anomalies associated with these features. We summarize our findings and discuss the physical processes that may be involved in Section 2.4.

2.2 Materials and methods

2.2.1 Numerical setup

We set up a yearlong, high-resolution, realistic general circulation model centered on Denmark Strait (Figure 2.1a). The dynamics are simulated using the [Massachusetts Institute of Technology General Circulation Model \(MIT-gcm; Marshall et al., 1997\)](#). The model solves the hydrostatic Navier-Stokes equations under Boussinesq approximation for an incompressible fluid with a nonlinear free surface (Campin et al., 2004). The realistic but simplified equation of state formula (Jackett and McDougall, 1995) and the K-profile

parameterization (KPP; Large et al., 1994) are implemented.

The model domain covers a larger area compared to previous similar setups (e.g., Haine et al., 2009; Magaldi et al., 2011; Koszalka et al., 2013; von Appen et al., 2014a; Gelderloos et al., 2017). It includes the entire Iceland Sea to the north as well as the southern tip of Greenland (Cape Farewell; 2.1a). The numerical domain is discretized with an unevenly spaced grid of 960×880 points. The resolution is about 2 km over the center of the domain and decreases moving toward the edges (the lowest resolution is about 4 km in the peripheral area). The vertical domain is discretized by 216 levels. The vertical grid uses partial bottom cells and the rescaled height coordinates z^* (Adcroft et al., 2004). The vertical resolution linearly increases from 1 to 15 m in the upper 120 m and is 15 m thereafter. The bathymetry is obtained from the 30 arc-s [International Bathymetric Chart of the Arctic Ocean \(IBCAO version 3.0; Jakobsson et al., 2012\)](#) north of 64°N and from Smith and Sandwell, 1997 elsewhere. Furthermore, the bathymetry is adjusted using depth data derived from deep-diving seals (Sutherland et al., 2013).

After an 8-month spinup started in January 2007, we have run the model storing the numerical solutions every six hours for twelve months (from September 2007 to August 2008). The time period matches a mooring array deployed on the East Greenland shelf and slope about 300 km downstream of Denmark Strait (von Appen et al., 2014b). The model initial conditions are obtained from the global $1/12^\circ$ reanalysis [HYbrid Coordinate Ocean](#)

Model+Navy Coupled Ocean Data Assimilation (HYCOM+NCODA; Cummings and Smedstad, 2013) and the monthly reanalysis Towards an Operational Prediction System for the North Atlantic European Coastal Zones, version 4 (TOPAZv4; Sakov et al., 2012). HYCOM+NCODA is also used to nudge the hydrographic and velocity fields at the four open boundaries. Sea surface temperature is relaxed with daily timescale to the Operational Sea Surface Temperature and Sea Ice Analysis global product (OSTIA; Donlon et al., 2012). Surface atmospheric forcings (air temperature, specific humidity, wind speed, evaporation, precipitation, and radiation) are based on the global atmospheric reanalysis ECMWF Re-Analysis (ERA-Interim Dee et al., 2011).

The oceanic component is coupled with the MITgcm sea ice model (Losch et al., 2010). TOPAZv4 is used to nudge the snow thickness and sea ice area, thickness, salinity, and velocities at the boundaries. The nudging timescale is one day at each boundary and linearly increases toward the interior to reach a maximum value of ten days at twenty grid points from the boundary. The freshwater forcing is significantly improved with respect to previous similar configurations. Surface runoff is estimated from a data set of daily, 1-km resolution Greenland Ice Sheet surface mass balance (Noël et al., 2016). Solid ice discharge is estimated from a combination of climate modeling plus satellite and terrestrial data (Bamber et al., 2012). Freshwater is distributed over the oceanic grid cells adjacent to Greenland (a similar approach has been used by Bakker et al., 2012).

2.2.2 Validation

We compare the model output in Denmark Strait with conductivity-temperature-depth (CTD) data from 111 shipboard transects occupied between March 1990 and August 2012 (Mastropole et al., 2017). Most of the data have been collected by the Marine Freshwater Institute of Reykjavik as part of their quarterly survey. Therefore, there is a good coverage throughout the different seasons. We use the data set processed by Mastropole et al., 2017: Each station has been projected onto the [Látrabjarg Line \(LL\)](#) (66.9°N, 29.8°W; 65.5°N, 24.6°W; [Figure 2.1a](#)), interpolated in depth space in the upper layer, and interpolated in density space in the lower layer. The observational mean hydrographic sections are reproduced in [Figures 2.2a, 2.2c, and 2.2e](#). We process the model output using the same procedure applied to the observational data. Specifically, we extract the model fields at the grid points corresponding to the location of the observational stations. Then, we construct the vertical sections by projecting and interpolating the numerical data using the hybrid interpolator described above. The observational data have been sampled over a ~ 20 -year period, whereas the numerical simulation only covers one year. Therefore, to match the seasonal distribution of the observations, we subsample the model at the same relative yearday corresponding to the stations. The mean hydrographic sections obtained from the model output are shown in [Figures 2.2b, 2.2d, and 2.2f](#).

Overall, the agreement between the model and the observations is excellent. The model captures all of the major water masses in Denmark Strait: the warm and salty subtropical-origin Irminger Water on the Iceland shelf; the

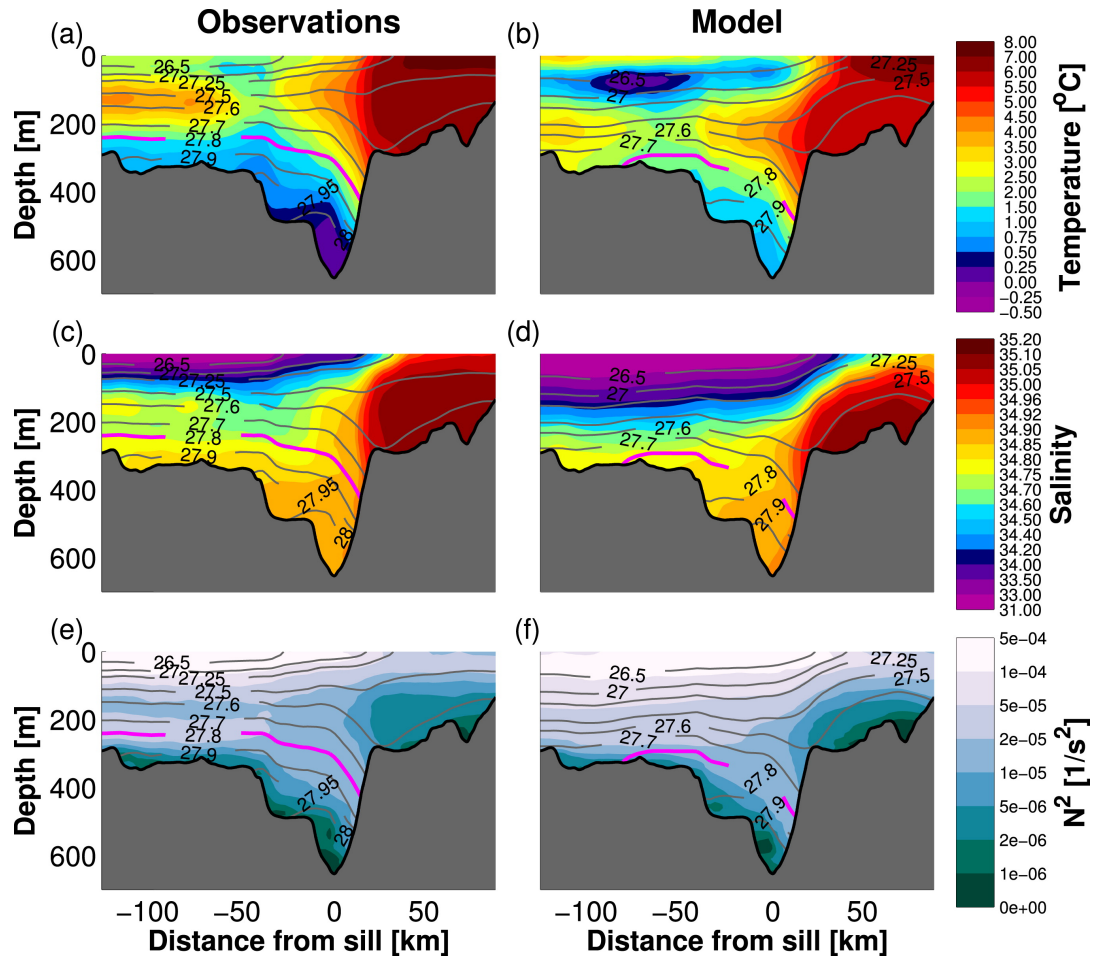


Figure 2.2: Time-mean vertical sections obtained from (left) observations (Mastropole et al., 2017) and (right) model outputs: (a, b) potential temperature; (c, d) salinity; (e, f) Brunt-Väisälä frequency. Grey contours represent the potential density anomaly in kg m^{-3} . The DSO interface is highlighted in magenta.

cold and fresh Arctic-origin Water extending from the western boundary into the strait; the relatively warm recirculated Irminger Water on the Greenland shelf; and the cold and dense overflow water in the trough. In addition, the model isopycnal structure across the strait is very similar to that seen in the observations. We also compare the spatial distribution of the simulated Brunt-Väisälä frequency (Figure 2.2f) with observations (Figure 2.2e). In both data sets, the overflow water and the deep portion of the Irminger Water on the Iceland shelf are weakly stratified. Quantitatively, there are some differences between the model fields and the observations. The Arctic-origin Water on the East Greenland shelf in the model is colder and fresher, whereas the model overflow is warmer by about 1°C in the deepest part of the trough. Because of this, the measured overflow interface (27.8 kg m⁻³ isopycnal) corresponds approximately to the 27.7 kg m⁻³ isopycnal in the model (contours in Figure 2.2). These biases could be due to both interannual variability and model errors. Indeed, Macrander et al., 2005 and Jochumsen et al., 2012 found warm overflow events in the 2000s. The overflow temperatures measured in this period were warmer by about 0.5°C than the average temperature.

Mastropole et al., 2017 described two fronts in their mean hydrographic sections (Figures 2.2a and 2.2c). Both of these fronts exist in our model and are located in roughly the same area as the observations (Figure 2.1): (i) One front is located in the center of the strait and corresponds to the separated **East Greenland Current (EGC)**. (ii) The second front is located near the Greenland shelfbreak and corresponds to the shelfbreak **EGC**. The fronts are particularly evident in the model temperature section (Figure 2.2b), which shows that

the coldest water in the upper layer is located west of the East Greenland shelfbreak, whereas the warmest water is confined to the Iceland shelf.

Hereafter, we estimate the Denmark Strait properties by fully sampling the model at the grid points along the LL. We find that the mean annual properties of the sections constructed using a 6-h regular sampling are consistent with the sections obtained using the uneven sampling described above (Figure 2.3). This is especially true on the Iceland shelf, where the majority of the measurements have been taken (Figure 2.3a). With a mean absolute anomaly of approximately 1°C , temperature is the most biased field (Figure 2.3b). Regularly sampled temperatures are colder on the Greenland shelf by about 2°C and the eastern flank of the trough is slightly warmer. By contrast, biases in salinity and density are generally small and very localized (Figures 2.3c and 2.3d). The regular sampling produces slightly fresher and lighter water in the westernmost area of the strait, whereas we find denser and saltier water in the upper 100 m in the center of the strait. Biases on the western side of Denmark Strait are mainly due to the dearth of measurements, whereas biases in the center of the strait are mainly due to the uneven temporal distribution of the observations. For example, fall is the season with the largest number of samples (about 33% of the transects). Figure 2.3d shows that the uneven sampling in Mastropole et al., 2017 produces densities in the deepest part of the trough and below ~ 200 m on the Greenland shelf that are consistent with the regular sampling. Therefore, the isopycnal contours in Figure 2.2 accurately represent the yearly mean densities in the strait.

Using data from a shipboard survey carried out in October 2008, Våge

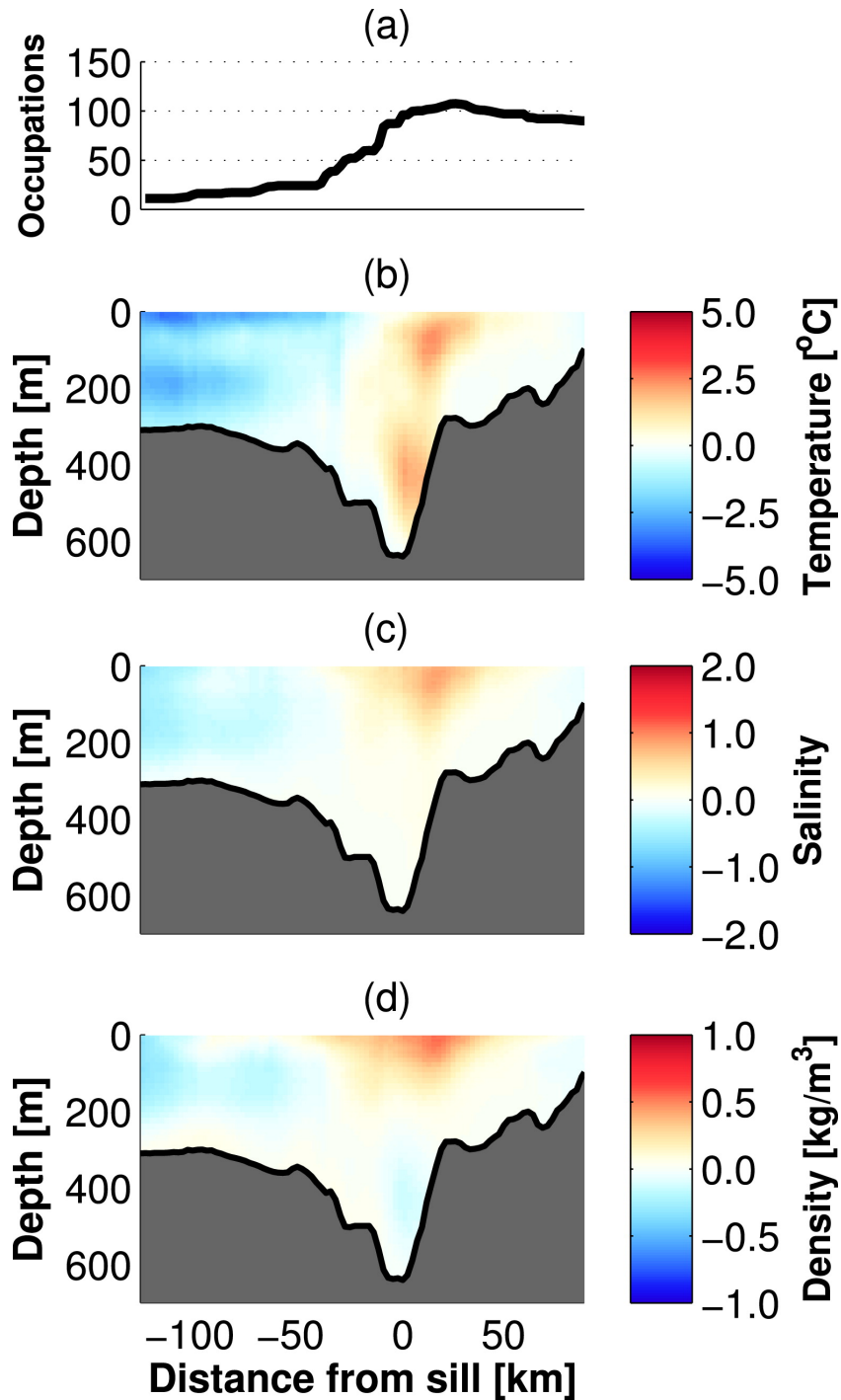


Figure 2.3: (a) Data coverage of the vertical sections. Anomalies of (b) potential temperature, (c) salinity, and (d) potential density for the regular minus the uneven sampling.

et al., 2011 computed the absolute geostrophic velocity normal to the LL (Figure 2.4a). This synoptic realization shows that the Denmark Strait Overflow Water (DSOW) flowing southward is banked against the Greenland side of the trough, whereas the subtropical-origin water flows northward on the eastern side of the trough in the North Icelandic Irminger Current (NIIC). These two currents are well captured in the mean October 2007 velocity section extracted from the model (Figure 2.4b). The mean model section also shows lighter DSOW flowing equatorward near the Greenland shelfbreak, which is consistent with the results of Mastropole et al., 2017, who demonstrated that Atlantic-origin DSOW is found in this region. The 2008 synoptic section of Våge et al., 2011 contains more complex flow structures than the mean model section. This is due to the energetic short time scale variability of the dynamics in Denmark Strait. Indeed, model snapshots display similar mesoscale variability, such as the October 1st, 2007 realization (Figure 2.4c).

2.2.3 Detection of mesoscale anomalies

Mastropole et al., 2017 characterized the structure and properties of boluses using a large collection of hydrographic sections occupied across Denmark Strait. Then, von Appen et al., 2017 augmented this data set with mooring data to compare the hydrographic and kinematic structure of boluses and pulses. Both boluses and pulses increase the southward transport of the overflow. In the former case, the large volume flux is primarily dictated by the increase in cross-sectional area of the water denser than 27.8 kg m^{-3} , whereas in the latter case it is mainly due to an enhancement of the near bottom flow.

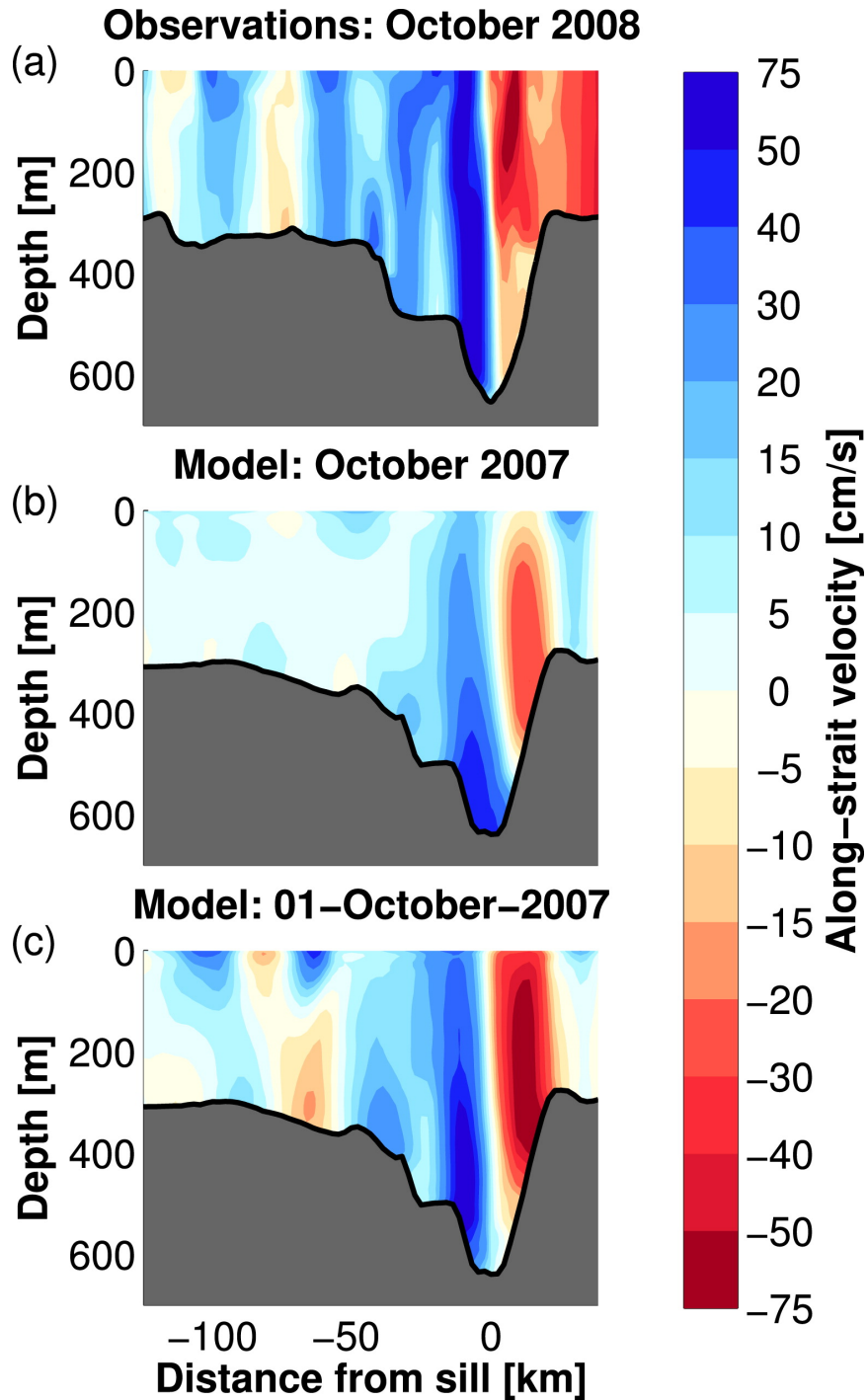


Figure 2.4: Vertical sections of (a) absolute geostrophic velocity measured in October 2008 (Våge et al., 2011), (b) monthly mean model velocity of October 2007, and (c) mean model velocity on October 1st, 2007.

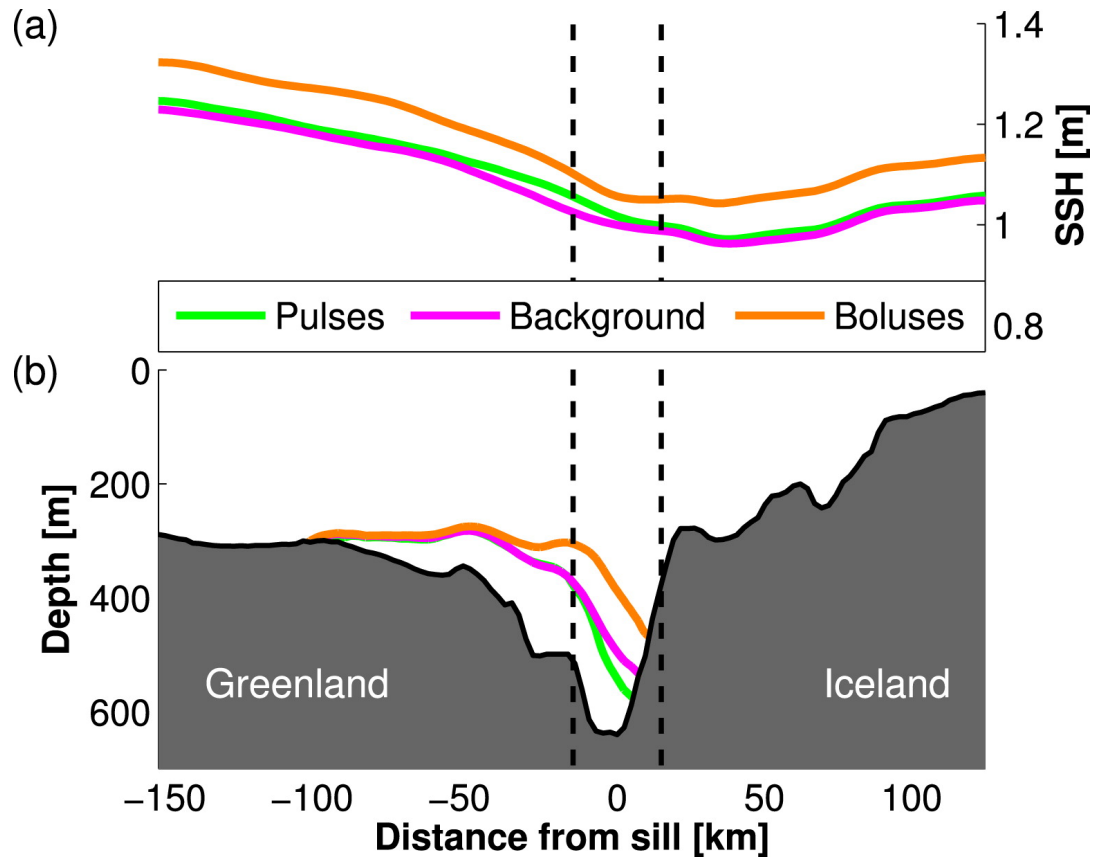


Figure 2.5: Comparison of (a) SSH and (b) DSO interface during boluses (orange), pulses (green), and background state (magenta). Black dashed lines bound the region from 15 km west to 15 km east of the deepest part of the sill. Negative (positive) distances correspond to northwest (southeast) of the sill. The viewer is looking to the north.

We use an objective method to identify boluses and pulses and we apply it to vertical sections across Denmark Strait extracted from our model. Nevertheless, this technique can be used to identify mesoscale features from observational data sets as well. The method consists of a set of thresholds calibrated using measured statistics and applied in the region from 15 km west to 15 km east of the deepest part of the sill (black dashed lines in Figure 2.5). In step 1, a vertical section is defined as containing a potential mesoscale

feature if the southward overflow transport is greater than the 25th percentile (considering the equatorward transport positive). In step 2, if the overflow cross-sectional area is smaller (larger) than the yearly 35th (65th) percentile, then the vertical section is deemed to contain a pulse (bolus). If the overflow transport or cross-sectional area thresholds are not exceeded, then the vertical section is considered to be representative of the background state. Therefore, we consider background state cases where there is a large *DSO* transport but the overflow interface does not deepen or shoal. Furthermore, we consider background state cases where the cross-sectional area of the overflow changes with a low *DSO* transport.

The mean cross-strait structures of the interface height for the two types of model mesoscale features extracted using this method are consistent with the observations. Figure 2.5b reveals that the maximum displacement of the *DSO* interface occurs in the middle of the strait for both types of features. Furthermore, the *Sea Surface Height (SSH)* across Denmark Strait rises everywhere by 4-10 cm during the passage of boluses and by up to 5 cm in the western side of the strait during pulses (Figure 2.5a). This is consistent with the correspondence between fluctuations in the time series of the Denmark Strait transport and *SSH* anomalies found by Haine, 2010. Another characteristic feature of the boluses described by Mastropole et al., 2017 is their weak stratification. Although our identification method does not employ any stratification thresholds, the overflow Brunt-Väisälä frequency (N^2) is lower during boluses in the model as well. This is particularly true on the eastern side of the trough, where N^2 is lower than the background state by about

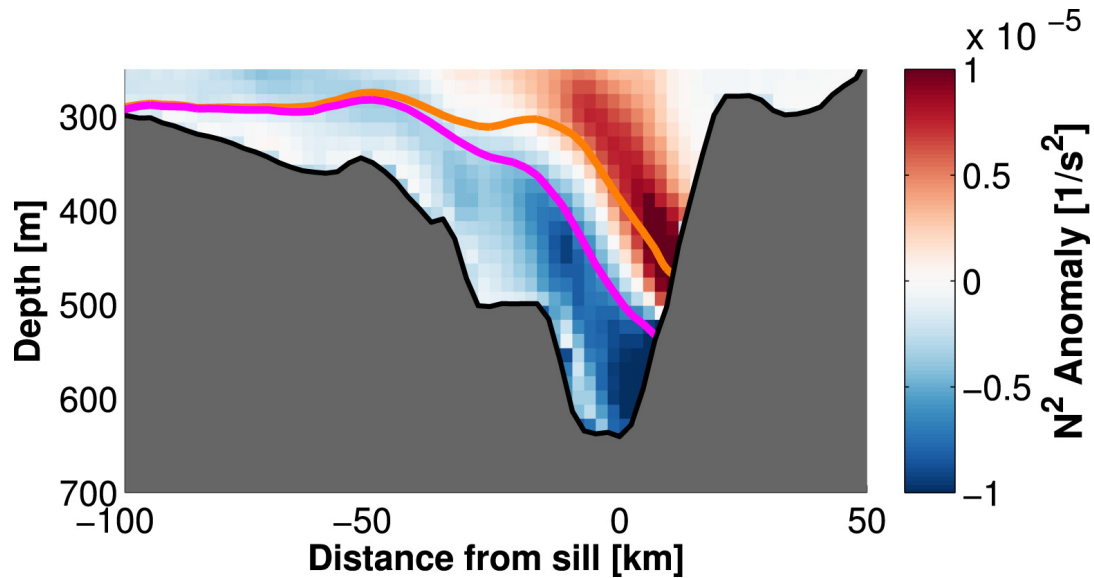


Figure 2.6: Composite of boluses minus background state Brunt-Väisälä frequency (N^2). The orange (magenta) line corresponds to the composite of boluses (background state) DSO interface.

10^{-5} s^{-2} (Figure 2.6).

2.3 Results

2.3.1 Statistics of mesoscale anomalies

On average, boluses occur in the model every 3.2 days, whereas pulses pass through Denmark Strait every 5.5 days. This is remarkably similar to the measurements analyzed by von Appen et al., 2017 (3.4 and 5.4 days for boluses and pulses, respectively). 31% (18%) of the vertical sections have been labeled as boluses (pulses), whereas about half of them do not contain any pronounced mesoscale feature. Pulses are associated with stronger southward velocities than boluses, which is also consistent with observations. Averaging over the area from 15 km west to 15 km east of the deepest part of the sill (black dashed

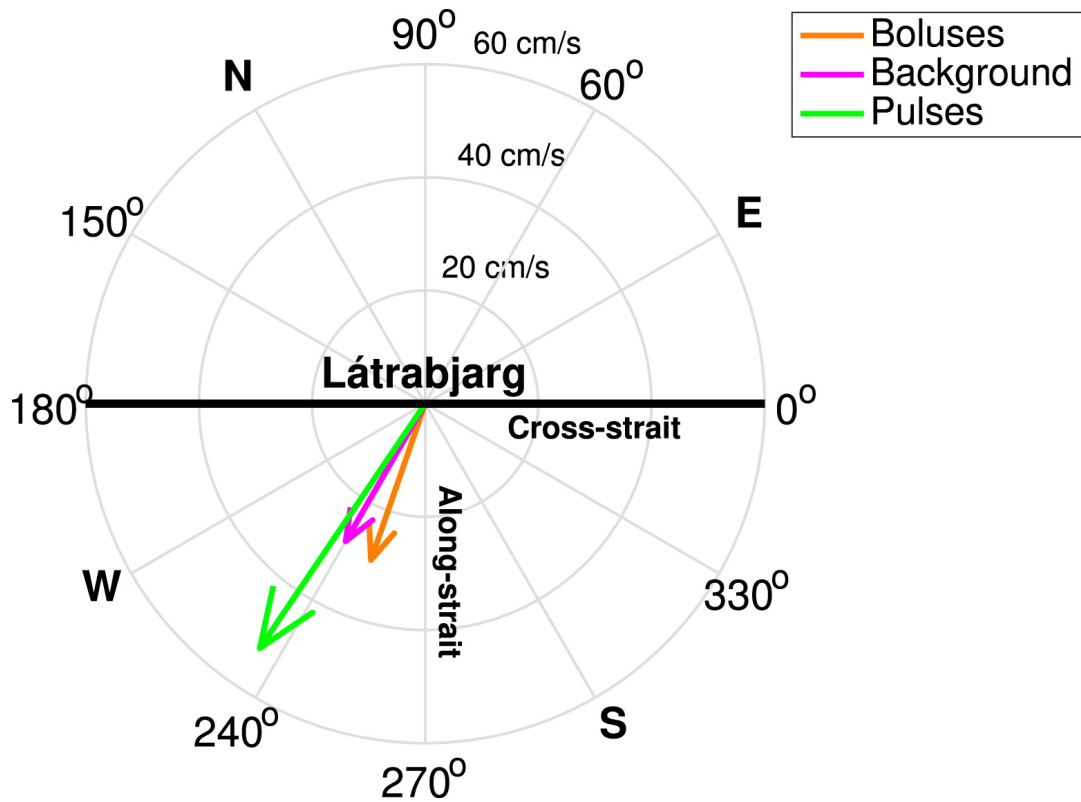


Figure 2.7: Mean velocity of the DSO between 15 km west and 15 km east of the sill in the composites of boluses (orange), pulses (green), and background state (magenta). The thick black line corresponds to the direction of the LL (cross strait).

lines in Figure 2.5), the mean along-strait equatorward speed of a pulse is 0.43 versus 0.27 m s^{-1} for a bolus (background state is 0.24 m s^{-1}). The mean cross-strait westward speed of a pulse is 0.29 versus 0.09 m s^{-1} for a bolus (background state is 0.14 m s^{-1}). The model reveals that the direction of the DSO is skewed relative to the along-strait direction (Figure 2.7). Furthermore, Figure 2.7 shows that the direction of boluses (pulses) is slightly tilted toward Iceland (Greenland). The mean southward DSO transport excluding boluses and pulses is by definition smaller than the mean transport estimated using all of the vertical sections. However, the model allows us to quantify the

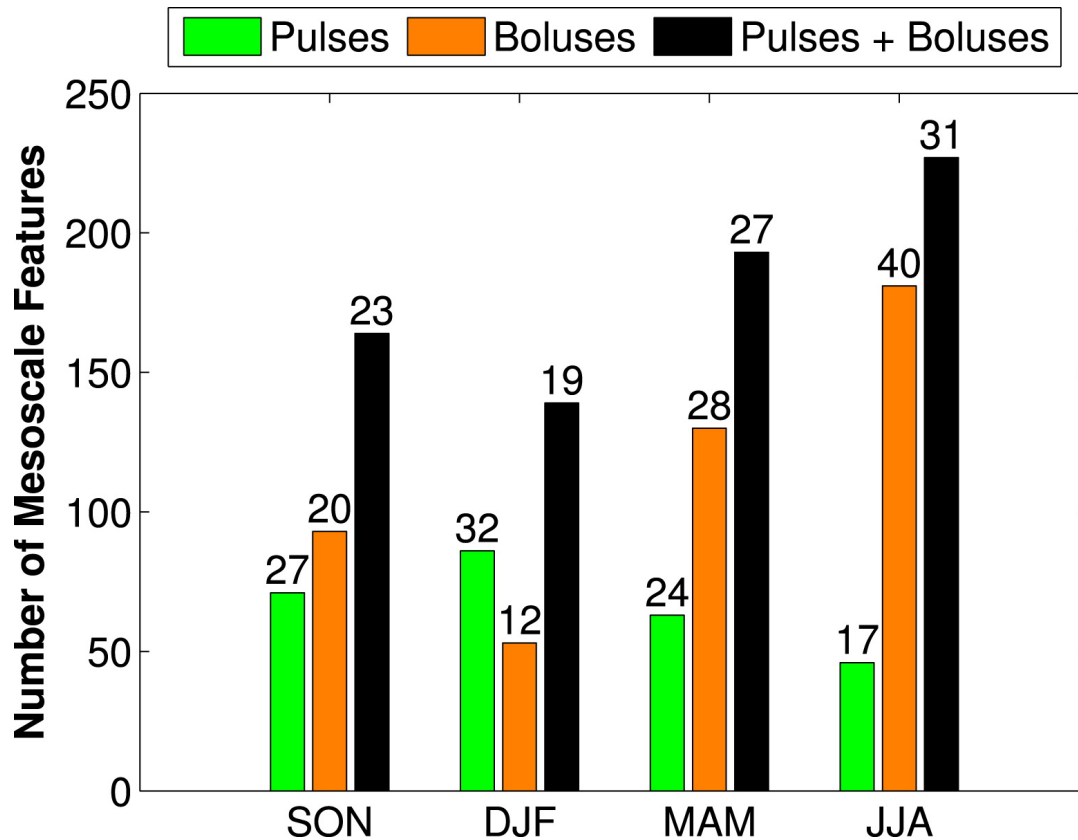


Figure 2.8: Seasonality of boluses and pulses. Green (orange) bars show the number of pulses (boluses) in a season. Black bars show the seasonal distribution of boluses + pulses. The numbers on the top of the bars indicate the percentage of boluses, pulses, or boluses + pulses, respectively. The 3-month acronyms for seasons are: [September-October-November \(SON\)](#); [December-January-February \(DJF\)](#); [March-April-May \(MAM\)](#); [June-July-August \(JJA\)](#).

contribution of boluses and pulses to the yearly mean [DSO](#) volume flux. We estimate that, excluding the mesoscale features, the transport is lower by about 30%.

In contrast with [Mastropole et al., 2017](#) and [von Appen et al., 2017](#), who did not find any seasonal signal, the model suggests that between September 2007 and August 2008 boluses and pulses are not evenly distributed throughout the year ([Figure 2.8](#)). Model boluses are more frequent during summer 2008 and

pulses occur more frequently in winter 2007-2008. Roughly 40% of boluses cross Denmark Strait between June and August 2008 and the minimum occurs between December 2007 and February 2008. Conversely, more than 30% of pulses occur in winter 2007-2008 and only 17% cross the strait in summer 2008. While these trends offset each other to some extent, the model suggests that the majority of the energetic mesoscale features occur in summer 2008 ($\sim 30\%$).

2.3.2 Time evolution of mesoscale anomalies

On average, bolus events are 57.1 ± 48.7 h long (\pm indicates standard deviations), whereas pulses are 27.5 ± 15.4 h long. We construct a composite of each type of event to shed light on their temporal evolution. We average together all of the boluses whose duration is between 47.1 and 67.1 h, which results in 13 events. Some of the pulses are asymmetric in their along-strait structure, so we exclude these from the pulse composite (we consider 12 events). Our rationale is to focus on the canonical features and to have similar numbers of realizations in each average. The time depth composites are shown in Figure 2.9 for hydrography and Figure 2.10 for circulation. These are obtained by averaging spatially over the area between 15 km west and 15 km east of the deepest part of the sill (black dashed lines in Figure 2.5). We normalize each bolus and pulse before creating composites and we use a normalized time axis corresponding to the length of the events.

Boluses correspond to an enhanced presence of cold and weakly stratified overflow water and a shallowing of the 27.8 kg m^{-3} interface (Figures 2.9a

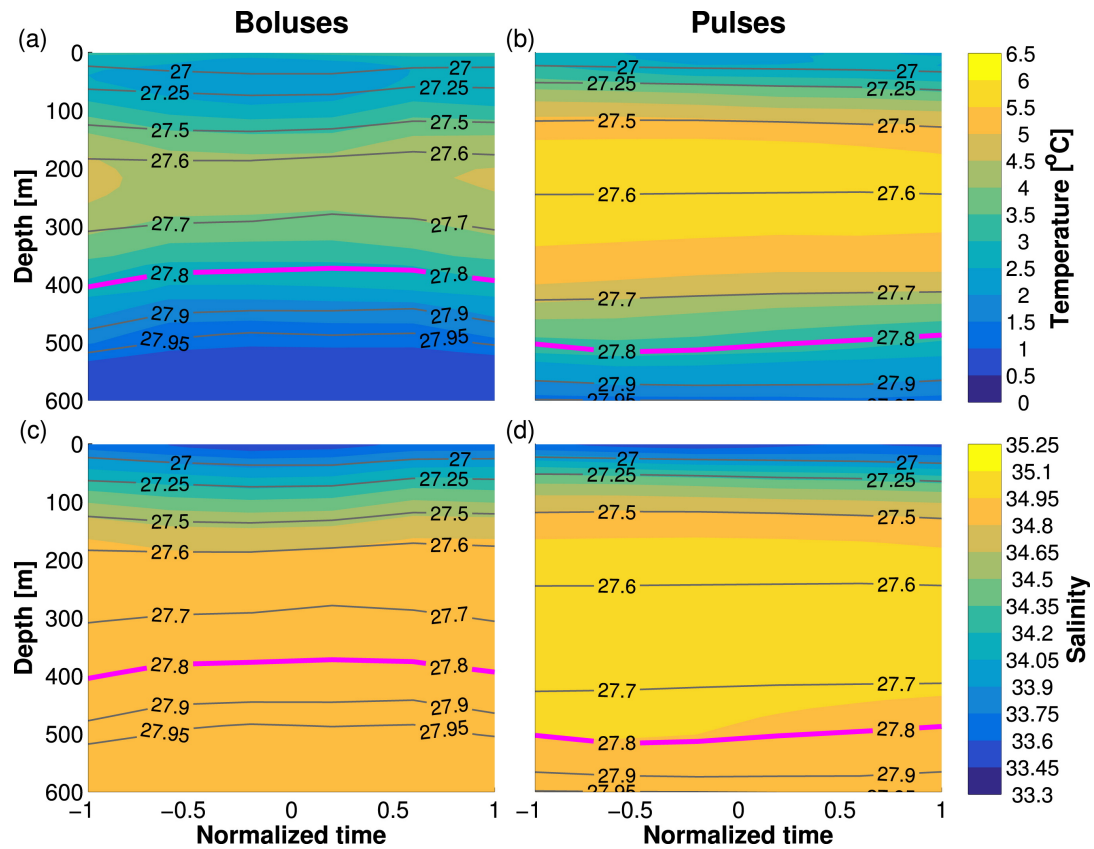


Figure 2.9: Time evolution of the composites of representative (left) boluses and (right) pulses obtained by averaging (a, b) potential temperature and (c, d) salinity over the area between 15 km west and 15 km east of the sill. The time axis is normalized to the length of the events (57.1 ± 10 h for boluses and 27.5 ± 15.4 h for pulses). The potential density contours are drawn in gray and the DSO interface is highlighted in magenta.

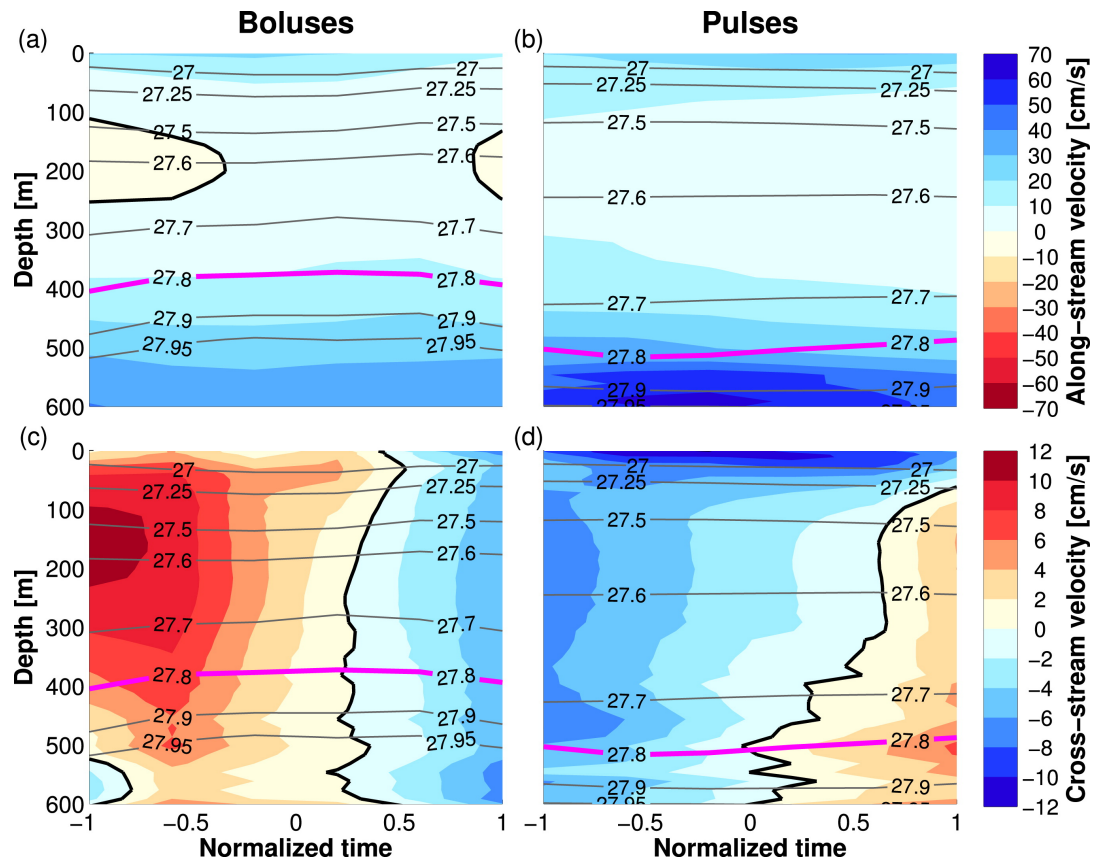


Figure 2.10: As in Figure 2.9, but for (a, b) along-stream velocity and (c, d) cross-stream velocity. The along-stream direction for boluses and pulses is defined as the orientation of the mean velocity vectors in Figure 2.7. Zero velocity contours are drawn in black.

and 2.9c). By contrast, pulses are characterized by a thinning of the overflow layer due to the depression of its interface (Figures 2.9b and 2.9d). There are clear differences in the middle of the water column and between the two features: Boluses contain slightly colder and fresher water, while there is a large presence of warm and salty Irminger Water at mid-depth during a pulse.

For the time-depth velocity composites we show the along-stream and cross-stream velocities (instead of the along-strait and cross-strait components). The reason is that boluses and pulses cross the strait with slightly different directions (Figure 2.7). As the mean velocity vectors in the overflow layer of the composites in Figure 2.10 agree with the mean velocity vectors computed considering every bolus and pulse, the along-stream direction for boluses and pulses is defined as the orientation of the mean velocity vectors in Figure 2.7. This revealed a kinematic structure that is in line with the observations. For boluses, there is not consistent variation in the along-stream flow of DSOW. However, there is a clear pattern in the cross-stream velocity for the upper layer that extends into the overflow layer as well. Specifically, the flow is toward Iceland at the leading edge of the bolus and toward Greenland at the trailing edge. This indicates that boluses are associated with veering of the horizontal circulation. For pulses, the along-stream flow of DSOW is significantly faster in the center of the feature, while the cross-stream flow is associated with backing: first toward Greenland, then toward Iceland. All of these characteristics are in line with the available observations (von Appen et al., 2017).

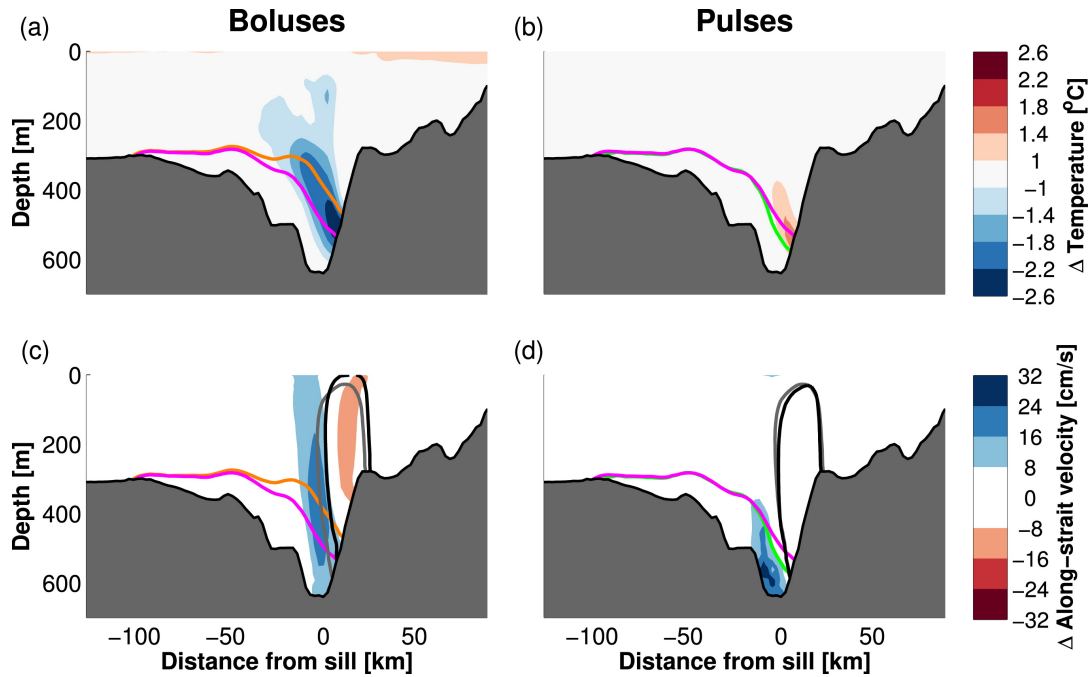


Figure 2.11: Composites of (left) boluses and (right) pulses minus the background state: (a, b) potential temperature and (c, d) along-strait velocity. Positive velocities are equatorward. The DSO interface during boluses (orange), pulses (green), and background state (magenta) are outlined. Gray contours bound the northward flow at the Iceland shelfbreak during the background state, whereas black contours bound the northward flow during boluses in (c) and pulses in (d).

2.3.3 Spatial evolution of mesoscale anomalies

We use composites to examine the spatial distribution of boluses and pulses as they progress through the strait (both in the vertical and horizontal plane). These composites include every snapshot identified as bolus, pulse, or background. Therefore, the averages in Figures 2.11 and 2.12 represent the mesoscale features when they are centered at the LL.

As shown in Figures 2.9c and 2.9d, the intermediate water is slightly saltier during pulses and fresher during boluses ($\Delta S \leq 0.05$), whereas anomalies in the overflow layer are negligible. These small salinity anomalies of the

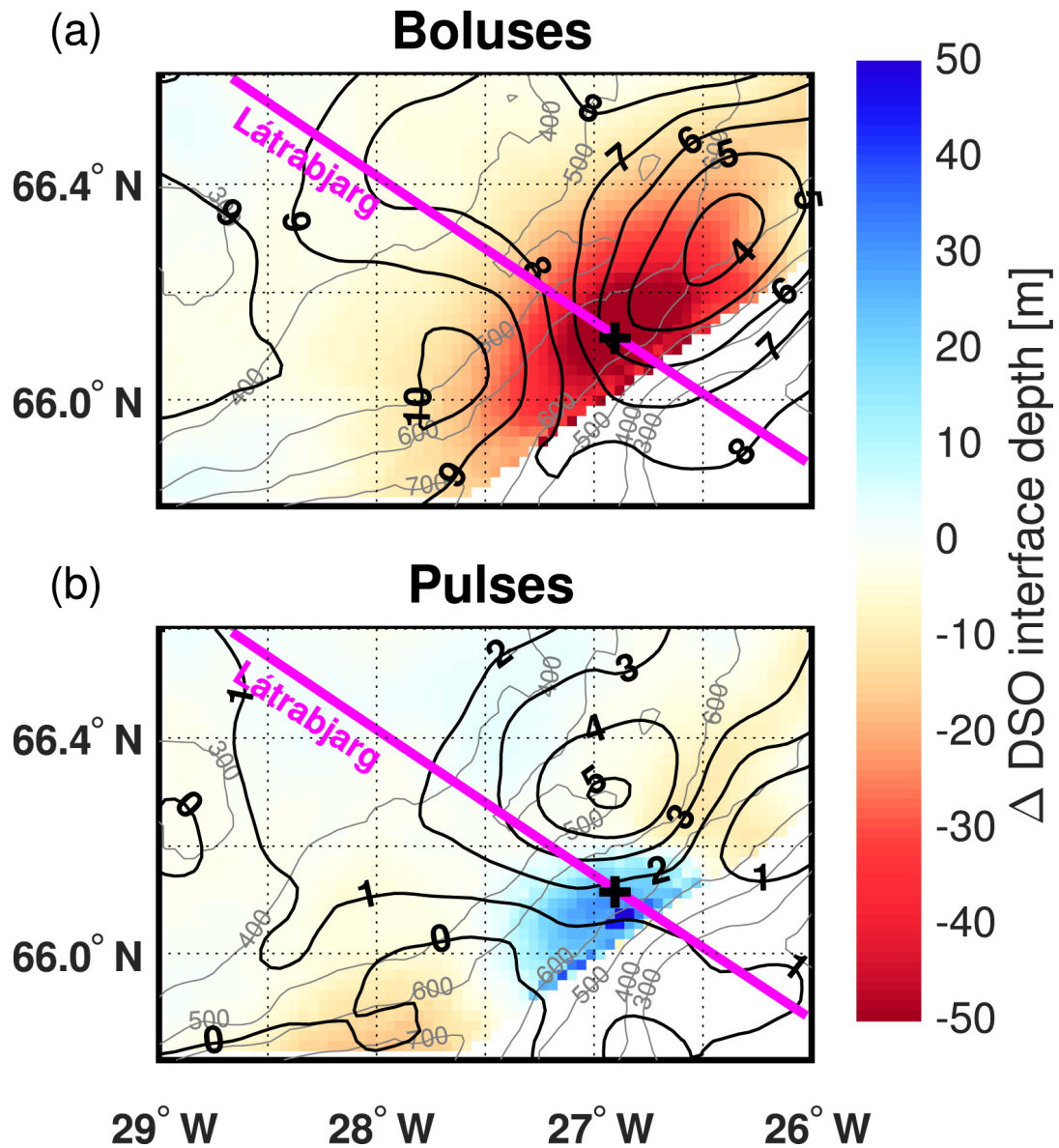


Figure 2.12: Composites of DSO interface during (a) boluses and (b) pulses minus the background state. Black contour lines show the SSH composite during boluses and pulses minus the background state (cm). The bathymetric contours (m) are shown in gray. The Látrabjarg Line (LL) is drawn in magenta and the black cross corresponds to the sill. Regions where the entire water column is lighter than the overflow water are masked white. Negative (positive) anomalies correspond to a shallower (deeper) DSO compared to the background state.

intermediate water are uniformly distributed across Denmark Strait, so salinity is omitted in Figure 2.11. However, there is a clear temperature anomaly in the vertical plane associated with each feature. The temperature in the trough is up to 2.6°C colder during bolus events. The cold water is mainly concentrated around the overflow (Figure 2.11a), although the anomaly extends more than 200 m above the 27.8 kg m⁻³ isopycnal. The largest temperature difference occurs on the eastern flank of the trough. By contrast, the temperature at the overflow interface increases by up to 1.8°C during pulses (Figure 2.11b). The largest difference again occurs on the eastern flank (same as boluses), but it is smaller.

Interestingly, there is no surface temperature signal within the trough during the passage of boluses and pulses (Figures 2.11a and 2.11b). Indeed, the time series in the region where our thresholds are applied do not show any clear link between surface temperature variability and mesoscale features (Figures 2.9a and 2.9b). Surface temperature anomalies are only present in the composite of boluses and are located on the Iceland shelf, where the surface water is warmer by up to 1.4°C. There are also well-defined anomalies in the vertical plane for the along-strait velocity. While the flow of DSOW is enhanced in each case, the composites reveal that there are differences in structure. During pulses, the signature is confined to the overflow layer (Figure 2.11d). The DSO increases by more than 30 cm s⁻¹ and the maximum anomaly occurs on the western flank of the trough. This large increase in speed is associated with the enhancement of the overflow transport together with the compression of the overflow layer. By comparison, the along-strait

velocity anomaly of the boluses is smaller ($<2.5 \text{ cm s}^{-1}$; Figure 2.11c), although the entire water column is impacted and there is anomalous northward flow as well. The enhanced southward flow is located in the center of the strait, whereas the northward anomaly is near the Iceland shelfbreak. This suggests that there is a link between boluses and the poleward flow of the NIIC.

Finally, we construct composites of the DSO interface height and SSH, and difference these from the background state to create anomalies (Figure 2.12). In agreement with the vertical plane perspectives shown above, the interface deflection at the sill is much more pronounced for boluses than pulses. On average, the DSO interface shoals by up to 85 m during boluses and deepens by up to 50 m during pulses. Therefore, boluses occupy a larger cross-sectional area than pulses. Both mesoscale features have elongated shape: The along-strait horizontal length scale is larger than the cross-strait horizontal length scale. Notably, the lateral scales of the two features are quite different and boluses also occupy a larger horizontal area. Furthermore, during the passage of a bolus, the interface height is elevated throughout the Denmark Strait. This is markedly different than pulses, where the interface is depressed over a relative confined region and is surrounded by a modest increase of layer height. SSH anomaly contours reveal a relative minimum upstream of the sill for a bolus and a relative maximum upstream of the sill for a pulse (black contours in Figure 2.12). These surface anomalies and the DSO interface anomalies are offset in the along-strait direction.

2.4 Summary and discussion

In this chapter we present results from a yearlong simulation of a high-resolution numerical model centered on Denmark Strait. This data set is publicly available on the Johns Hopkins SciServer system (Medvedev et al., 2016). The code to reproduce the results is also publicly available (<https://doi.org/10.7281/T1Q52MS4>).

Our goals are to characterize and better understand the variability of the hydrography and circulation in Denmark Strait associated with boluses and pulses. These are the two dominant mesoscale features in the strait, both of which occur during overflow surges. To detect boluses and pulses, we use an objective method based on transport and cross sectional area of the DSO. We use statistics measured by von Appen et al., 2017 to calibrate our thresholds.

The general properties of boluses and pulses in the model are summarized in Table 2.1. Boluses occur more frequently than pulses and are of longer duration. The DSO interface shoals during boluses and deepens during pulses. The along-strait length scale of boluses is larger compared to pulses. Seasonally, boluses are more common in summer 2008, whereas pulses appear more often in winter 2007-2008.

We quantify the temporal and spatial structure of boluses and pulses by constructing composite averages. On average, boluses correspond to a thicker, colder, and more weakly stratified DSO layer with moderately enhanced equatorward velocity. Above the overflow water, the Atlantic layer becomes slightly colder and fresher, and there is a strong cross-stream velocity signature

Table 2.1: Summary of boluses and pulses mean properties and thresholds.

Thresholds and properties	Boluses	Pulses
DSO transport threshold (percentile)	>25	>25
Cross-sectional area threshold (percentile)	>65	<35
Mean duration (h)	57.1	27.5
Frequency of occurrence (days)	3.2	5.5
Mean along-strait velocity (m s^{-1})	0.27	0.43
Mean cross-strait velocity (m s^{-1})	0.09	0.29
Maximum Δ DSO interface depth (m) ^a	-85	+50
Δ SSH (cm)	4-10	0-5
Δ T at the DSO interface ($^{\circ}\text{C}$)	-2.6	+1.8
Δ S of the DSO	≈ 0	≈ 0
Rotation of the DSO direction over time	Veering	Backing

^a Negative anomaly corresponds to shallower DSO interface relative to the background state.

indicative of veering. By contrast, pulses are characterized by a thinning of the DSO layer and a stronger increase in equatorward velocity. Warm and salty Irminger Water appears in the middle of the water column and the cross-stream flow is again strong above the overflow layer (except in this case it is indicative of backing). These results are in line with the measurements of Mastropole et al., 2017 and von Appen et al., 2017.

The high-resolution, three-dimensional model fields allow us to go beyond the available observations. We find that the temperature anomalies are strongest near the overflow interface. Specifically, water near the interface of the overflow layer is colder by about 2.6°C during boluses and warmer by about 1.8°C during pulses. The enhanced equatorward flow during pulses is confined to the overflow layer on the western side of the trough, whereas for boluses it extends throughout the water column in the center of the trough.

Interestingly, the poleward flow of the NIIC (Figure 2.1) increases during bolus events. The lateral extent of boluses is much greater than that of pulses and the DSO interface is raised throughout Denmark Strait. By contrast, the interface is depressed over a much smaller region during pulses and in the surrounding area it is slightly raised. We estimate that the mean southward transport of the DSO is about 30% lower in the absence of boluses and pulses. Therefore, these features play a major role in controlling the variability of the DSO transport.

We find that boluses and pulses have a clear signature in SSH anomaly. Boluses are associated with a relative minimum upstream of the sill (bowl), whereas pulses are associated with a relative maximum upstream of the sill (dome). Assuming that the flow is in geostrophic balance, these anomalies imply enhanced DSO flow toward Iceland during boluses (cyclonic) and toward Greenland (anticyclonic). This is consistent with the flow vectors shown in Figure 2.7. Similar to the western tilt with height that occurs in mid-latitude weather systems, the SSH and DSO interface anomalies are not in phase. Idealized models of baroclinic instability (e.g., Eady, 1949) show how this lag implies the release of available potential energy and conversion to eddy kinetic energy (e.g., Pedlosky, 1979; Vallis, 2017; Klinger and Haine, 2019). It is still uncertain if boluses and pulses are triggered by different dynamical processes. The formation of pulses may be explained by the baroclinic destabilization of density-driven abyssal flows theorized by Reszka et al., 2002. On the other hand, boluses are associated with an enhanced equatorward flow throughout the whole water column and, as hypothesized by Mastropole et al., 2017, may

be related to the North Icelandic Jet (NIJ).

Chapter 3

Evolution of overflow surges south of the strait

Using a realistic numerical model, we find new evidence of the causal relationship between high-transport events at the Denmark Strait sill and [Denmark Strait Overflow \(DSO\)](#) cyclones observed downstream. Most of the cyclones form at the sill during overflow surges and, because of [Potential Vorticity \(PV\)](#) conservation and stretching of the water column, grow as they move equatorward. A fraction of the cyclones form downstream of the sill, when anticyclonic vortices formed during high-transport events start collapsing. Regardless of their formation mechanism, [DSO](#) cyclones weaken starting roughly 150 km downstream of the sill, and [PV](#) is only materially conserved during the growth phase.

This chapter is published by the journal *Geophysical Research Letters* Almansi et al., [2020](#).

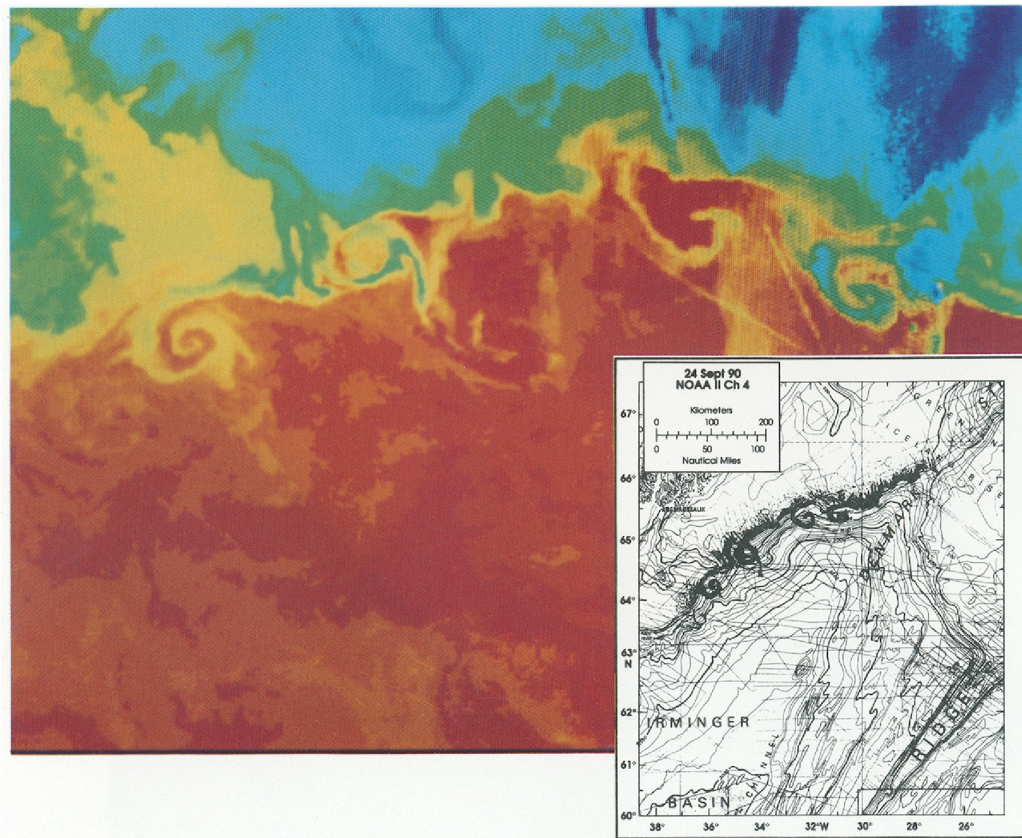


Figure 3.1: Infrared imagery of sea surface temperature on September 24, 1990. Accompanying sketch shows location and shape of eddies and seafloor depth contours in meters. The Denmark Strait sill is at upper right. Source: Bruce, 1995.

3.1 Introduction

Downstream of Denmark Strait, the high-frequency variability of the overflow is dominated by the presence of energetic cyclones. The first studies of these features, known as *DSO* cyclones, used laboratory experiments (Whitehead et al., 1990), satellite imagery (Figure 3.1; Bruce, 1995), and surface drifter trajectories to describe some of their basic characteristics (Krauss, 1996). Several studies using idealized models then explored the underlying dynamics of

the cyclones (Spall and Price, 1998; Krauss and Käse, 1998; Jungclaus et al., 2001; Reszka et al., 2002). Spall and Price, 1998 formulated the so called “PV Outflow Hypothesis”. Cyclogenesis in their three-layer model was explained via conservation of PV in the presence of strong vortex stretching. The three layers defined by Spall and Price, 1998 are composed of relatively (i) fresh, cold, and light East Greenland Current (EGC) water at the surface; (ii) dense Denmark Strait Overflow Water (DSOW) at the bottom; and (iii) Arctic Intermediate Water (AIW) in between, which is not as cold and dense as the DSOW (Figure 3.2). These layers are stretched downstream of Denmark Strait, particularly the intermediate layer as the other layers are constrained to the bottom/surface. Therefore, assuming the absence of diabatic and frictional processes, positive relative vorticity is generated to conserve PV in each layer.

Magaldi et al., 2011 used a high-resolution realistic model to relate DSO cyclones with the East Greenland Spill Jet, which is a current banked against the upper East Greenland continental slope downstream of the Denmark Strait sill (Pickart et al., 2005). Koszalka et al., 2017 performed Lagrangian simulations to investigate the hydrographic and mixing anomalies associated with mesoscale eddies. von Appen et al., 2014b used data from a mooring array in conjunction with satellite fields to characterize DSO cyclones at the so-called Spill Jet (SJ) section, which is located about 300 km downstream of Denmark Strait and extends from the continental shelfbreak to a depth of 1000 m. They found that DSO cyclones represent the largest source of variability at this location.

Although the model results of Spall and Price, 1998 indicate that these

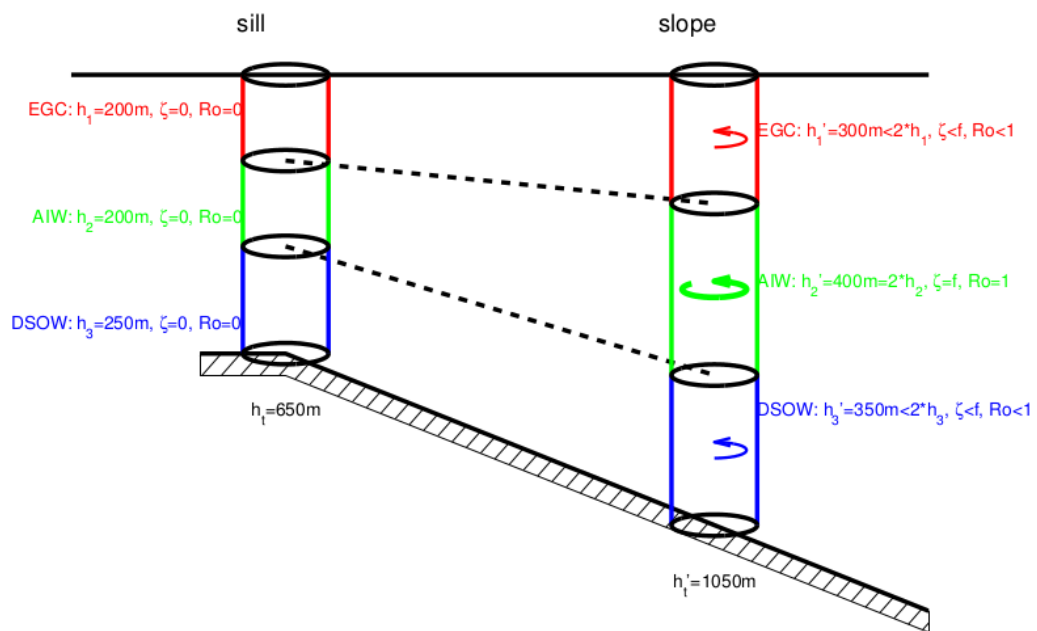


Figure 3.2: Cartoon of the stretching process leading to the generation of cyclonic vorticity. h is the height of the water column, ζ is the relative vorticity, Ro is the Rossby number, and f is the vertical component of the Coriolis parameter. Source: von Appen, 2013.

features can form from a steady overflow, von Appen et al., 2017 hypothesized a one-to-one connection between the passage of the boluses/pulses discussed in Chapter 2 and the formation of DSO cyclones. The authors argued that boluses lead to strong DSO cyclones downstream, while pulses result in weaker cyclones. The idea is that the cyclonic vorticity generated by the stretching of the water column downstream of the sill enhances the initially cyclonic boluses, and overcomes the initially anti-cyclonic pulses. The notion of a causal relationship between the mesoscale variability at the sill and the downstream cyclones proposed by von Appen et al., 2017 was based on simple correlations using two different moored data sets. However, at present it remains a hypothesis which needs to be investigated further.

In this chapter, we use an improved version of the general circulation model presented in Chapter 2 to fill the gaps in the sparse measurements along the DSO path (Figure 3.3) and better understand the nature of the DSO variability. The goal of the study is threefold: (i) To further quantify the characteristics of the high frequency DSO fluctuations; (ii) To explore the dynamics associated with PV conservation and stretching of the water column as the overflow descends from the sill; and (iii) To characterize the life cycle of DSO cyclones as they progress into the Irminger Basin. The chapter is organized as follows: In Section 3.2 we describe the materials and methods used, including the setup of the numerical model, its comparison with observations, and the criteria used to detect DSO mesoscale features. In Section 3.3 we present new evidence of the causal relationship between DSO cyclones and high-transport events, and we use composite averages to

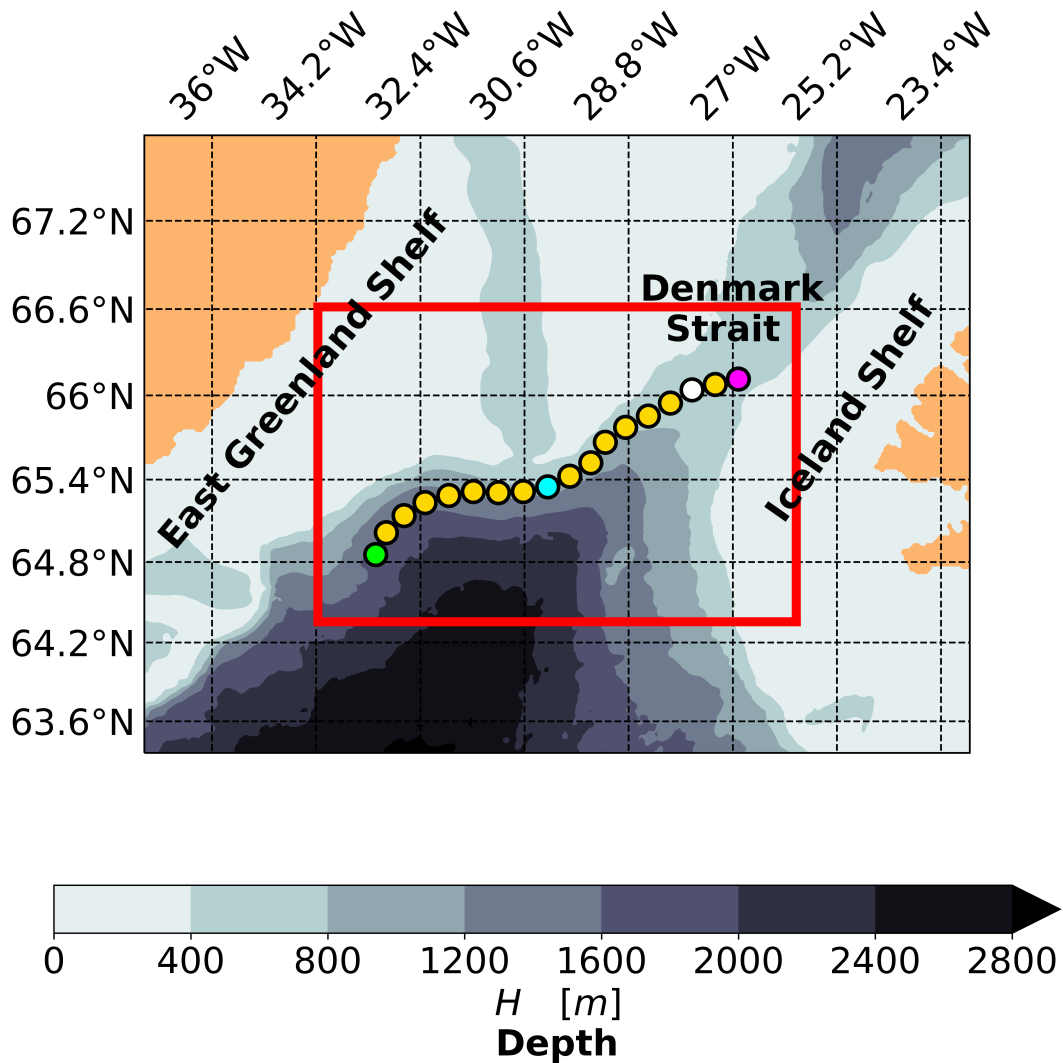


Figure 3.3: Seafloor bathymetry in the region of interest for this study. Red lines bound the area fed to the vortex detection algorithm shown in Figure 3.5. Circles indicate the stations along the DSO path (Koszalka et al., 2017). Circles colored in magenta, white, blue, and green indicate where the DSO path crosses hydrographic sections known as the Látrabjarg Line (LL; magenta line), Denmark Strait South (DSS), Transient Tracers in the Ocean (TTO), and Spill Jet (SJ), respectively.

investigate the evolution of the cyclones along the [DSO](#) path. We summarize and discuss our findings in [Section 3.4](#).

3.2 Materials and methods

3.2.1 Numerical setup

The results presented in this chapter are based on the numerical solutions of a yearlong, high-resolution, realistic circulation model. An identical configuration with different atmospheric forcing is explained in detail in [Chapter 2](#). The numerical solutions are publicly available on the Johns Hopkins SciServer system ([Medvedev et al., 2016](#)). Additional fields have been computed, extracted, and visualized offline using OceanSpy v0.1 ([Almansi et al., 2019](#)) and several packages from the Pangeo software ecosystem (e.g., [Dask Development Team, 2016](#); [Hoyer and Hamman, 2017](#)).

The model is particularly well suited to study mesoscale features occurring on short timescales (1-10 days; [Almansi et al., 2017](#); [Spall et al., 2019](#)). The horizontal resolution is 2 km in the vicinity of Denmark Strait, and the vertical resolution is 15 m or better throughout the water column. Snapshots have been stored from September 2007 to August 2008 at 6-hour frequency. [Haine et al., 2009](#) found that the spatial resolution of the atmospheric fields used to force high-resolution models significantly affects the ocean circulation in Denmark Strait. Therefore, we use the 15-km resolution [Arctic System Reanalysis \(ASRv2; Bromwich et al., 2018\)](#), which represents a significant improvement in horizontal resolution of the atmospheric forcing previously implemented

(ERA-Interim; Dee et al., 2011). It has been shown that, compared to global reanalyses, higher-resolution regional reanalyses reduce the wind-speed biases with respect to atmospheric observations (Bromwich et al., 2016).

Compared to Figure 2.2, annual mean model vertical sections of hydrographic and velocity fields do not show differences relevant to this study. The major currents and water masses measured in Denmark Strait are well captured by the model. The small hydrographic biases of the overflow in the previous version of the model are improved, but not eliminated. The DSO is slightly warmer and lighter in the model compared to the historical observations analyzed by Mastropole et al., 2017. Density and temperature biases do not exceed 0.1 kg m^{-3} and 1°C , respectively. The model solutions used in this chapter have also been compared to drifter pathways by Saberi et al., 2020 and to data collected upstream of Denmark Strait by Håvik et al., 2019 (see Chapter 4). Overall, the agreement between the model and the available observations around Denmark Strait is excellent.

3.2.2 Vortex detection scheme

We designed an automatic vortex detection scheme based on the Okubo-Weiss (OW) parameter (Okubo, 1970; Weiss, 1991) to isolate DSO cyclones:

$$\text{OW} = S_n^2 + S_s^2 - \zeta^2. \quad (3.1)$$

S_n , S_s , and ζ are, respectively, the normal component of the strain, the shear component of the strain, and the relative vorticity of the horizontal velocity

field:

$$\begin{aligned}
 S_s &= \frac{\partial v}{\partial x} + \frac{\partial u}{\partial y}, \\
 S_n &= \frac{\partial u}{\partial x} - \frac{\partial v}{\partial y}, \\
 \zeta &= \frac{\partial v}{\partial x} - \frac{\partial u}{\partial y}
 \end{aligned} \tag{3.2}$$

where $\mathbf{u} = (u, v, w)$ is the vector velocity field written as a function of Cartesian position $x\hat{\mathbf{x}} + y\hat{\mathbf{y}} + z\hat{\mathbf{z}}$. Several methods have been used in previous studies to detect mesoscale features (Lian et al., 2019). Most of them are based on sea surface fields. The following arguments motivated our choice to use the **OW** parameter: (i) Strain and relative vorticity can be computed from the velocity field in the middle of the water column (Equation 3.2), where the signal of **DSO** cyclones is strongest (von Appen et al., 2014b); (ii) **DSO** cyclones are characterized by high relative vorticity, and the **OW** scheme allows one to discern vorticity-dominated features ($\text{OW} < 0$) from the background state; (iii) The typical magnitude of the **OW** parameter does not vary significantly in the water column, and we can define a depth-independent threshold to detect **DSO** cyclones along terrain-following levels.

Dense overflows are known to vary in their proximity to the seafloor (Shapiro et al., 2003). Therefore, the detection algorithm operates on three terrain-following levels (σ -levels). We extracted the σ -levels using a nearest-neighbor vertical interpolation. Defining H as the seafloor depth, the uppermost level is located at a depth of $H/2$ (where measurements show the strongest signal of **DSO** cyclones; von Appen et al., 2014b), the deepest level

is located at $3H/4$ (in proximity to the **DSO** interface), and the mid-level is halfway between the top and bottom levels. Unless otherwise specified, the results shown and discussed hereafter refer to the mid-level ($5H/8$).

Our detection algorithm includes several filters to overcome the sensitivity to noise of the **OW** parameter (Souza et al., 2011). In line with most of the **OW** schemes designed to detect ocean eddies (e.g., Isern-Fontanet et al., 2006), the first step of the algorithm locates vorticity dominated regions with $\text{OW} < -0.2\sigma_{\text{OW}}$, where σ_{OW} is the spatial standard deviation of the **OW** parameter calculated at each snapshot and σ -level. For each of the terrain-following levels, closed contours bounding these regions have been deemed as vortices and fit to ellipses. A size filter excludes features with semi-minor axis smaller than 7.8 km, which is the mean radius of **DSO** cyclones measured by von Appen et al., 2014b at the **SJ** section. Furthermore, ellipses with area larger than $4\pi^2 L_D^2$, which tend not to be mesoscale features, are excluded (Klocker and Abernathey, 2014; Martínez-Moreno et al., 2019), where $L_D = 7.7$ km is the nearest first-baroclinic Rossby radius of deformation computed by Chelton et al., 1998 (note that the observational radius is consistent with the theoretical radius). More permissive size filters mainly affect the number of vortices detected near the **SJ** section, where the vortices are smaller, but do not impact the results discussed in this chapter. Furthermore, because of the model horizontal resolution, the mean properties of vortices with axes lower than the threshold chosen might be significantly impacted by noise. Finally, in order to exclude potential **DSO** cyclones without vertical coherence, the algorithm only retains features with a signal in the entire lower half of the water column

(overlapping ellipses in all σ -levels).

Figure 3.4 shows the location of the centers of the mesoscale vortices detected. Although the vertical component of the Coriolis parameter (f) does not change significantly within the study region, we present and discuss the nondimensional relative vorticity ($f^{-1}\zeta$). The majority of the cyclones ($\overline{f^{-1}\zeta} > 0$; overlined quantities correspond to spatial averages in the regions occupied by the vortices and f is the vertical component of the Coriolis parameter) are located in proximity to the DSO path and move southward along the continental slope (Figure 3.4a). By contrast, most of the anticyclones ($\overline{f^{-1}\zeta} < 0$) are located over Dohrn Bank and on the western side of the Denmark Strait trough (Figure 3.4b). These anticyclones move southwestward following the edge of the East Greenland shelf.

We applied a set of additional filters to exclude features unrelated to the DSO. Only mesoscale features covering regions with \overline{H} greater than 450 m are retained. This threshold excludes the vortices on the East Greenland shelf that do not interact with the DSO. Furthermore, we applied a distance threshold to exclude the cyclones far from the DSO path. Downstream of station #04, where the DSO moves along the continental slope, we excluded vortices with centers located farther than 20 km from the DSO path. Specifically, this filter excludes the cyclones in the Kangerdlugssuaq Trough and the anticyclones on the edge of the East Greenland shelf. Upstream of station #05, where the isobaths are far apart, we applied the same spatial filter exclusively to the vortices detected on the southeast side of the DSO path. This filter retains the anticyclones that cross Denmark Strait on the western side of the trough,

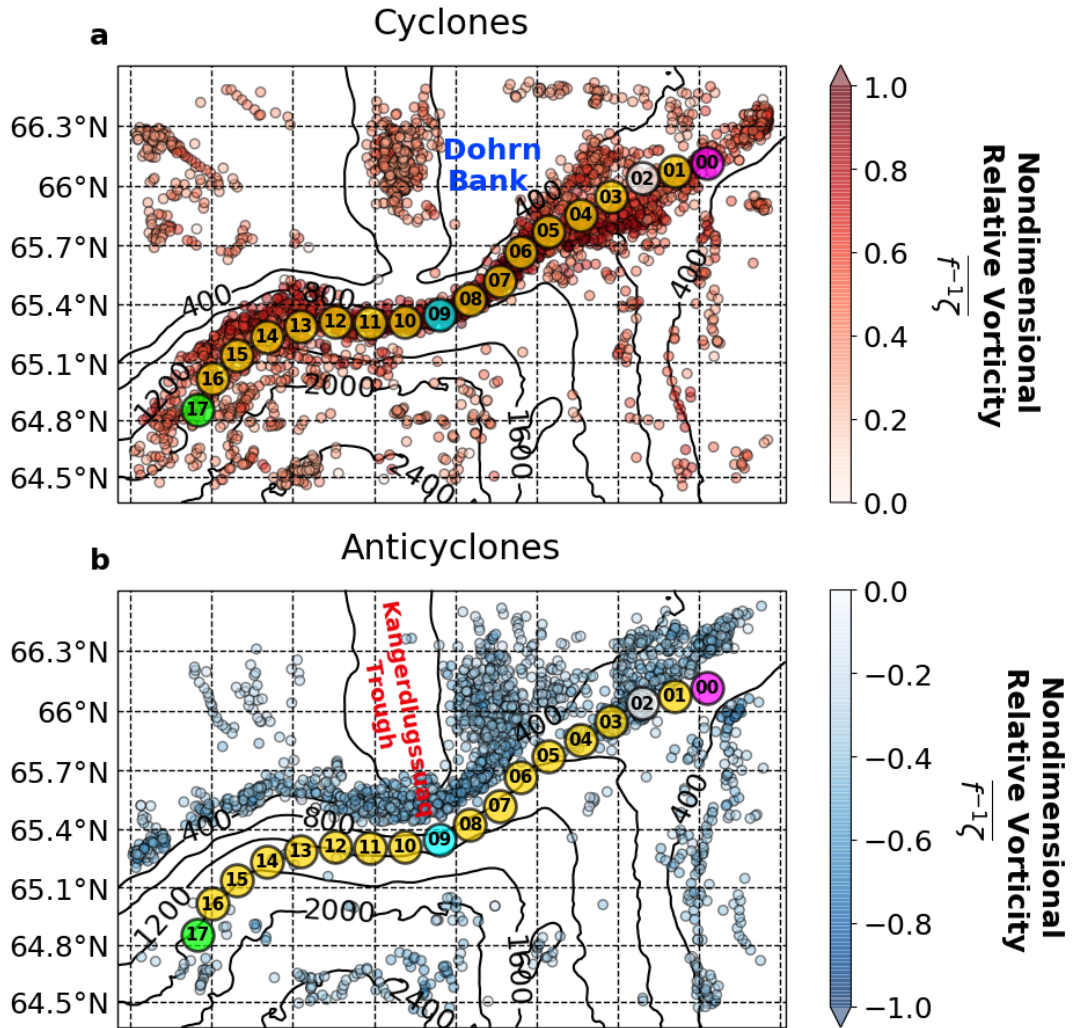


Figure 3.4: Unfiltered locations of the centers of the detected cyclones (a) and anticyclones (b). The color code indicates the mean nondimensional relative vorticity ($f^{-1}\zeta$) of the vortices. ζ has been extracted along the σ -level at a depth of $5H/8$. Black contours show the seafloor depth in meters. The color code convention of the DSO stations is the same used in Figure 3.3.

which are related to a fraction of **DSO** cyclones observed at the **SJ** section (von Appen et al., 2017).

Figure 3.5 shows the location of the centers of the filtered vortices. The cyclones ($\overline{f^{-1}\zeta} > 0$) are located in proximity to the **DSO** path and move southward along the continental slope. The anticyclones ($\overline{f^{-1}\zeta} < 0$), which are thought to be related to a fraction of **DSO** cyclones observed at the **SJ** section (station #17 von Appen et al., 2017), are located on the western side of the Denmark Strait trough.

3.2.3 Identification of high-transport events

We conducted a census of boluses and pulses using the same criteria defined in Chapter 2. First, we extracted vertical sections at the **Látrabjarg Line (LL)** in the region from 15 km west to 15 km east of the deepest part of the sill (magenta line in Figure 3.4). Next, we excluded snapshots where the volume flux of the overflow is lower than the yearly 25th percentile. Lastly, we deemed the remaining snapshots to contain a bolus (pulse) if the cross-sectional area covered by the overflow is larger (smaller) than the yearly 65th (35th) percentile. In line with previous studies, the **DSO** interface corresponds to $\sigma_\theta = 27.8 \text{ kg m}^{-3}$ ($\sigma_\theta = \rho - 1000 \text{ kg m}^{-3}$; Dickson and Brown, 1994). It is important to note that high-transport events and **DSO** cyclones have been detected independently, and none of the criteria used to characterize boluses and pulses have been implemented in the vortex detection algorithm.

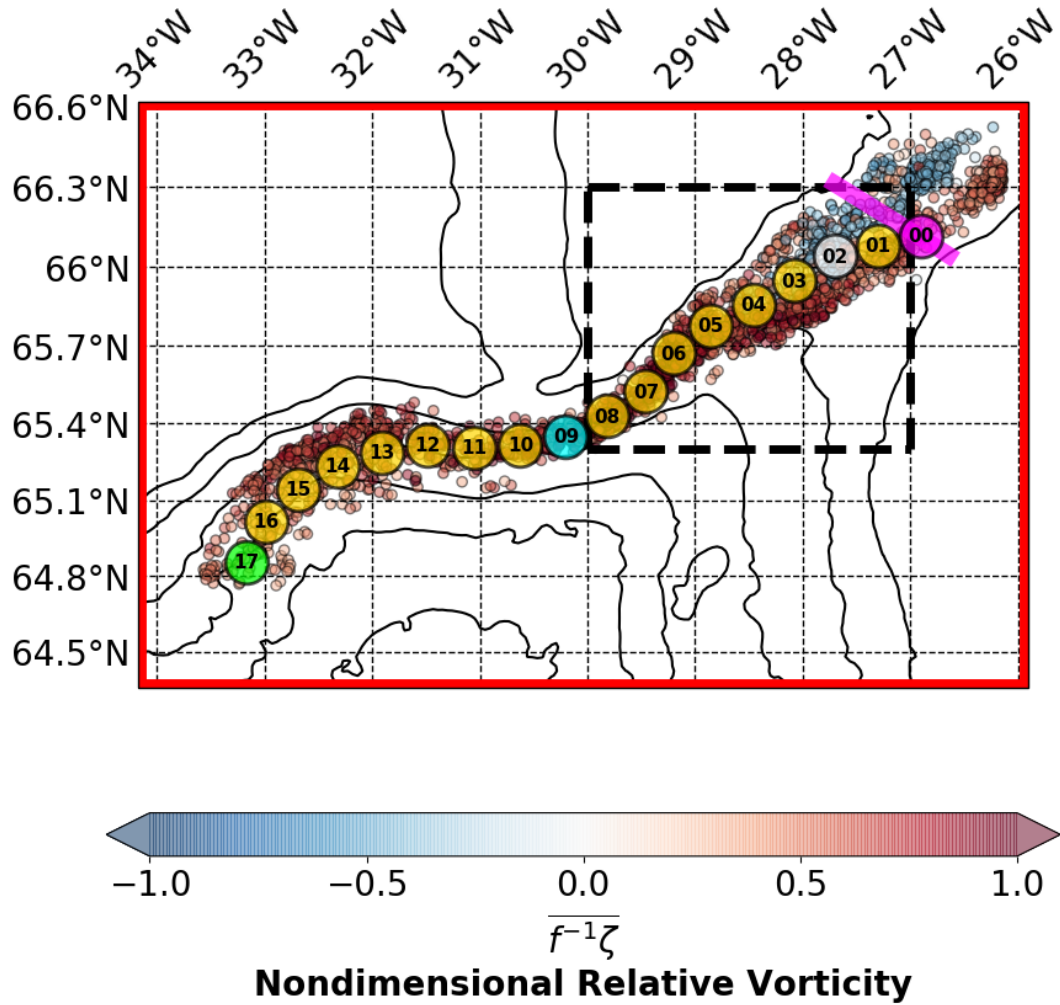


Figure 3.5: Location of the centers of the filtered vortices color-coded by their mean nondimensional relative vorticity ($\overline{f^{-1}\zeta}$) at a depth of $5H/8$. Black contours show the bathymetry in meters. Black dashed lines bound the region shown in Figure 3.3. The color code and labeling conventions of the DSO stations are the same used in Figure 3.4.

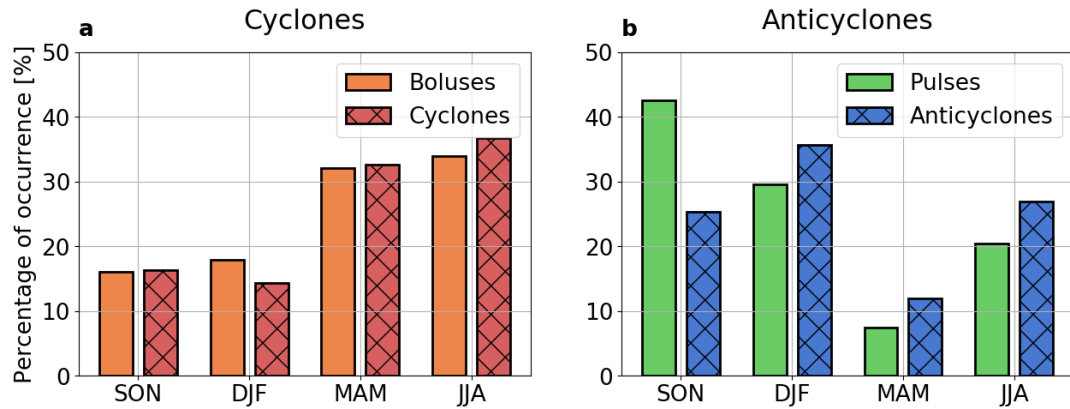


Figure 3.6: Seasonal frequency of occurrence of (a) boluses and cyclones, and (b) pulses and anticyclones. Red (blue) hatched bars show the percentage of cyclones (anticyclones) detected in a season compared to the total number of cyclones (anticyclones). Orange (green) bars show the frequency of occurrence of boluses (pulses). The 3-month acronyms for seasons are: September-October-November (SON); December-January-February (DJF); March-April-May (MAM); June-July-August (JJA).

3.3 Results

3.3.1 Relationship between DSO cyclones and overflow surges

In contrast to the measurements analyzed by Mastropole et al., 2017 and von Appen et al., 2017, the mesoscale features in the model are not evenly distributed across the year. Therefore, we can use the seasonal signal to indicate the link between boluses/pulses and vortices. We find that the temporal distribution of the cyclones and anticyclones detected near the LL station are consistent with the statistics of boluses and pulses, respectively (Figure 3.6). The variability of overflow surges in the annual cycle simulated is discussed in more detail in Chapter 2. More than 50% of the boluses and cyclones were detected between March 2008 and August 2008 (Figure 3.6a), while the frequency of occurrence of pulses and anticyclones is low in spring

2008 (Figure 3.6b). The distribution of boluses matches very well the frequency of occurrence of the cyclones in all seasons. Some biases exist between the seasonal distribution of pulses and anticyclones. Specifically, a lower fraction of anticyclones was detected between September 2007 and November 2007 compared to the pulse events. Nevertheless, the distribution of pulses across the year matches the frequency of occurrence of the anticyclones reasonably well (particularly from December 2007 to August 2008).

We selected two events that highlight the connection between boluses/cyclones (Figures 3.7, and 3.7b), and pulses/anticyclones (Figures 3.7c and 3.7d). Specifically, we investigate their spatial and temporal evolution along terrain-following levels. The vorticity field (Figure 3.7a) shows a cyclone crossing Denmark Strait over the deepest part of the sill. At the same time, a bolus was detected at the LL. The density difference between the snapshot exhibiting the cyclone and the background state (yearly average) highlights positive density anomalies within the perimeter of the cyclone (Figure 3.7b). As we are investigating density fields along terrain-following levels, higher densities ($\Delta\sigma_\theta > 0$) are the result of the shoaling of the deep isopycnals. These anomalies are consistent with the thickening of the overflow layer characteristic of boluses. Figure 3.7c shows an anticyclone detected near the LL during a pulse event (January 30th, 2008). In contrast to the cyclone described above, the anticyclone corresponds to a region with instantaneous density lower than the background state (Figure 3.7d). The deepening of the isopycnals is consistent with the presence of pulses, which enhance the southward volume flux of the overflow and reduce its thickness.

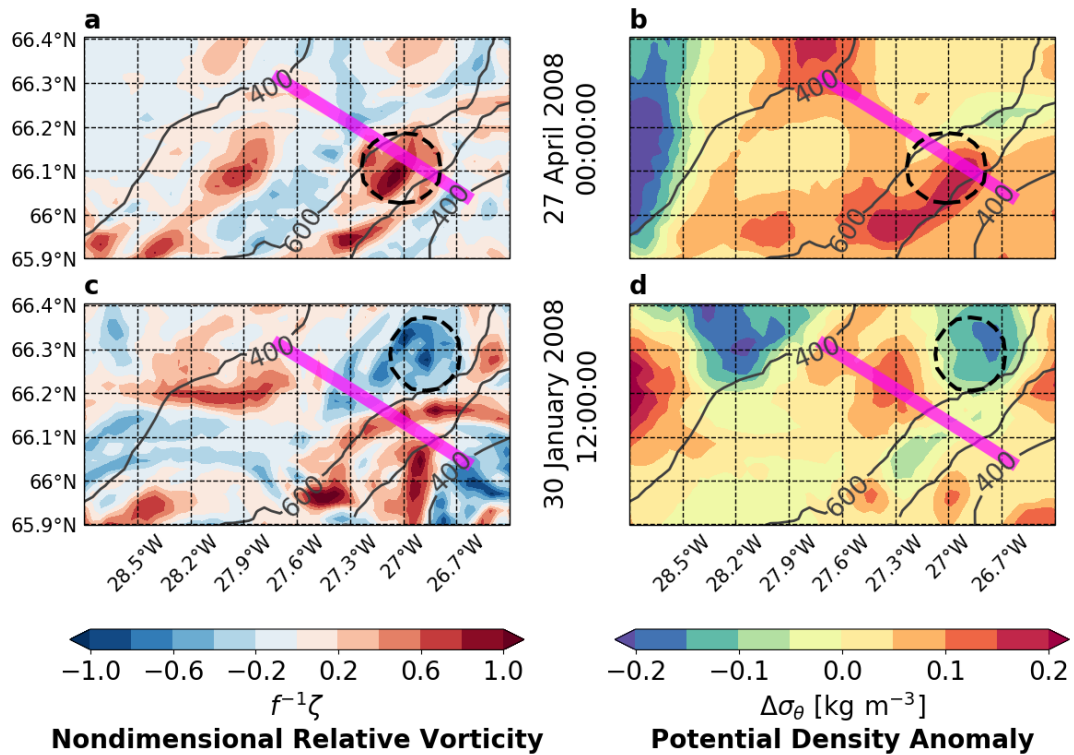


Figure 3.7: Relative vorticity (a, c) and instantaneous potential density minus the yearly mean (b, d) during a bolus and a pulse. The bolus (a, b) crossed the LL (drawn in magenta) on April 27th, 2008 at midnight. The pulse (c, d) was detected in Denmark Strait on January 30th, 2008 at noon. Dark gray contours indicate the seafloor depth in meters. Dashed lines bound the vortices detected. Fields have been extracted along the σ -level at a depth of $5H/8$.

Composite vertical sections of the cyclones (Figures 3.8a, 3.8c, and 3.8e) and anticyclones (Figures 3.8b, 3.8d, and 3.8f) at the LL also support the existence of a causal relation with overflow surges. During cyclones, the water near the eastern side of the trough is denser compared to the yearly average (Figure 3.8a), while it is lighter during anticyclones (Figure 3.8b). Denser (lighter) water is the result of the shoaling (deepening) of the DSO interface characteristic of boluses (pulses). During anticyclones, the enhanced equatorward flow is confined to the deepest part of the trough (Figure 3.8d), whereas during cyclones it extends throughout the whole water column. In the latter case, the strongest velocity anomalies are located at the interface of the overflow layer (Figure 3.8c). On the Iceland shelf, the poleward flow of the North Icelandic Irminger Current (NIIC) strengthens during cyclones (Figure 3.8c). Finally, anticyclones coincide with an enhanced cross-sectional flow toward Greenland within the overflow layer (Figure 3.8f). All of these anomalies in the composites of cyclones and anticyclones are consistent with the anomalies associated with boluses and pulses, respectively (Almansi et al., 2017; Mastropole et al., 2017; von Appen et al., 2017).

It has been previously shown that mesoscale features associated with high-transport events act to relax the NIIC hydrographic front in the model (i.e., they are the product of baroclinic instability; Spall et al., 2019). The location of the detected cyclones (Figure 3.5) and the front in the along-strait velocity anomalies (Figure 3.8c) indicate that the cyclones are centered on the eastern side of the trough. The front intersects the whole water column, is located between equatorward anomalies at the centre of the trough and

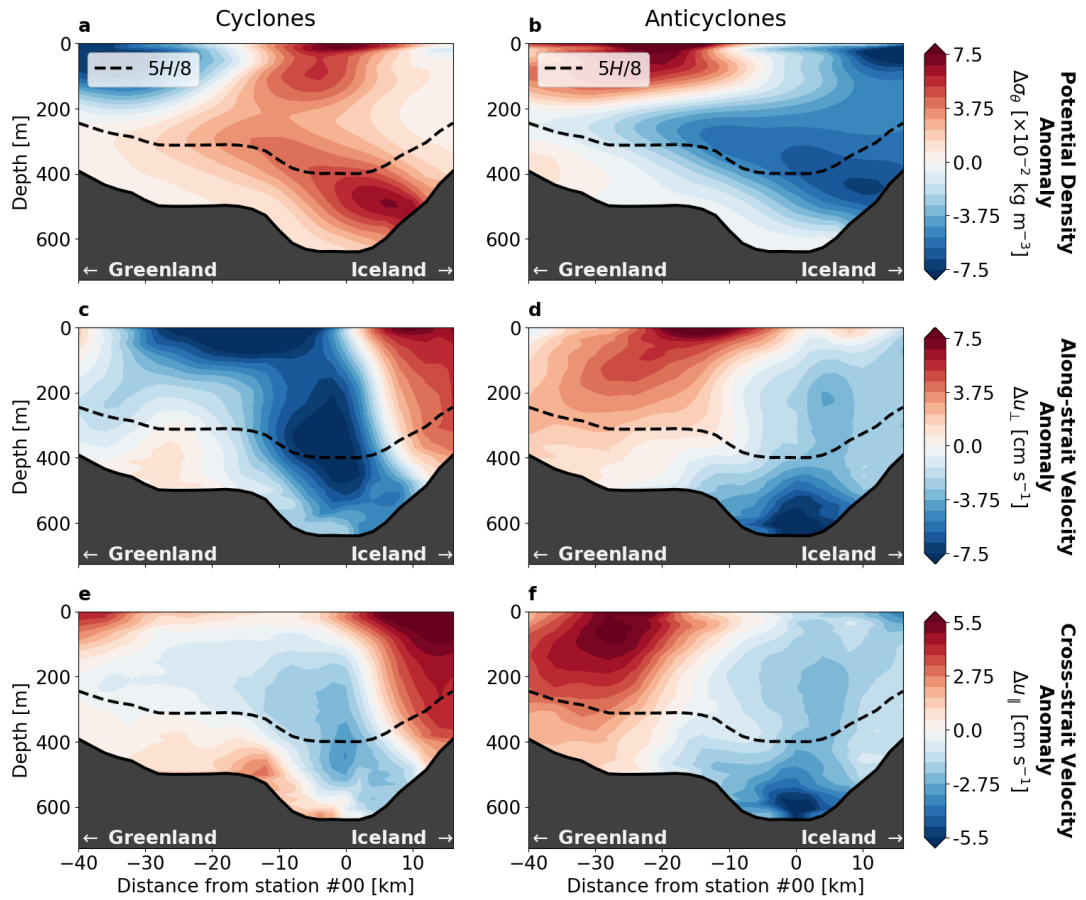


Figure 3.8: Composite vertical sections along the LL of cyclones (anticyclones) detected within 48 hours from overflow surges minus the yearly averages are shown in the left (right) column: (a and b) potential density; (c and d) along-strait velocity (orthogonal to the LL); (e and f) cross-strait velocity (tangential to the LL). The viewer is looking to the north: Positive along-strait (cross-strait) velocities are towards the pole (Iceland). The dashed line corresponds to the σ -level at a depth of $5H/8$.

poleward anomalies on the eastern side, and is more pronounced at mid-depths (including the σ -level at a depth of $5H/8$; Figure 3.8c). As the cyclones move downstream following the DSO path (southwestward), their relative vorticity grows. The height of the water column also increases along the path (i.e., stretching of the water column), suggesting that positive relative vorticity is added to the mesoscale features due to vortex stretching.

As opposed to the cyclones, the location of the detected anticyclones (Figure 3.5) and the along-strait velocity anomaly front (Figure 3.8d) show that the anticyclones cross Denmark Strait on the western side of the trough. The front is located between equatorward anomalies at the centre of the trough and poleward anomalies on the western side (Figure 3.8d). The DSO direction is slightly tilted towards northwest (Figure 3.8f), which causes the anticyclones to slowly veer towards Greenland. The paths followed by the anticyclones suggest that the 400-meter isobath prevents the anticyclones from reaching the East Greenland shelf. As the vortices move towards the shelf, the anticyclonic relative vorticity is sustained by the shrinking of the water column. When the anticyclones reach the edge of the shelf, new cyclones form south of them (Figure 3.9). The plots in the left column of Figure 3.9 show this process for a single event corresponding to the pulse shown in Figures 3.7c and 3.7d. The right column corresponds to composites of anticyclones detected near station #03. First, bands of positive relative vorticity surround the slowly-moving core of the anticyclones (Stage I; Figures 3.9a and 3.9b). Then, the peripheral bands of positive relative vorticity strengthen and converge, triggering the formation of cyclones south of the collapsing anticyclones (Stage II; Figures 3.9c and

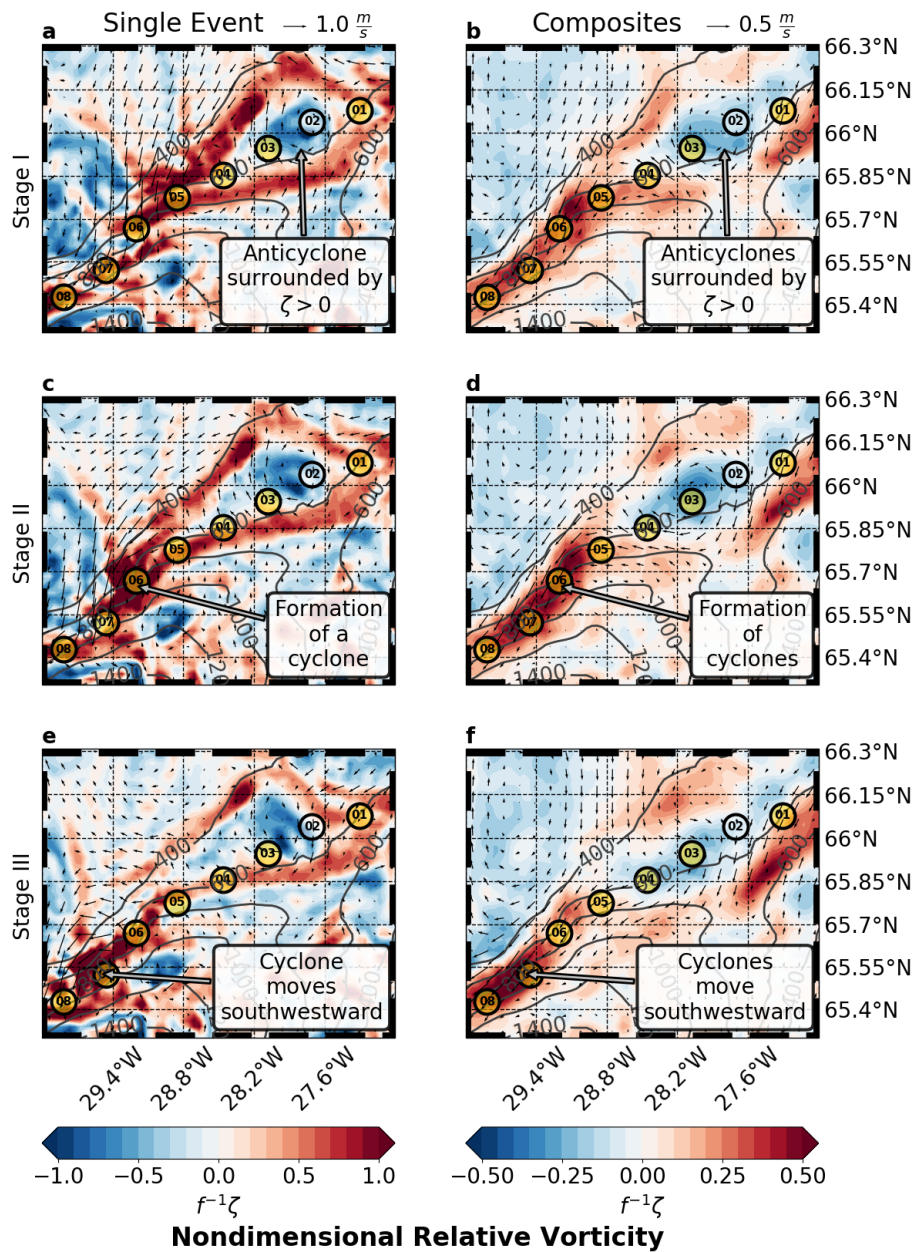


Figure 3.9: Nondimensional relative vorticity ($f^{-1}\zeta$) and velocity vectors extracted along the σ -level at a depth of $5H/8$. The region shown is bounded by black dashed lines in Figure 3.5. Labeled circles correspond to the DSO stations. Three consecutive snapshots (a, c, and e) following the pulse in Figures 3.7c and 3.7d, and composites of thirty anticyclonic events (b, d, and f) are shown. The composite of Stage II (d) includes the snapshots where anticyclones have been detected near station #03. The stages are six hours apart. Dark gray contours indicate the seafloor depth in meters.

3.9d). Last, the anticyclones vanish and the cyclonic features triggered by the anticyclones move southwestward following the **DSO** path (Stage III; Figures 3.9e and 3.9f). As these cyclones move downstream, they gain positive relative vorticity due to stretching of the water column.

3.3.2 Downstream evolution of **DSO** cyclones

The geometry and relative vorticity magnitude of the cyclones associated with pulses are similar to the properties of the cyclones formed during the bolus events. Therefore, to investigate their evolution as they move downstream, we created composites at fixed stations along the **DSO** path including all of the detected cyclones (Figure 3.10). The **DSO** stations are spaced ~ 20 km apart. They overlap the **DSO** pathway mapped by Koszalka et al., 2017 using the time- and depth-averaged trajectories of synthetic Lagrangian particles.

The background relative vorticity downstream of Denmark Strait is cyclonic along the entire **DSO** path (labeled circles in Figure 3.10a). The anticyclones associated with pulses impact the background relative vorticity, which decreases moving from the **LL** to the **Denmark Strait South (DSS)** station. Downstream of station #02, where most of the anticyclones spin down, the background relative vorticity monotonically increases moving towards station #07. This is consistent with the hypothesis that **PV** conservation governs the dynamics in this region (Spall and Price, 1998; von Appen et al., 2014b; von Appen et al., 2017). Positive relative vorticity is generated in response to the stretching of the water column. Downstream of Denmark Strait, the light upper layer is constrained at the surface, while the dense **DSO** is constrained

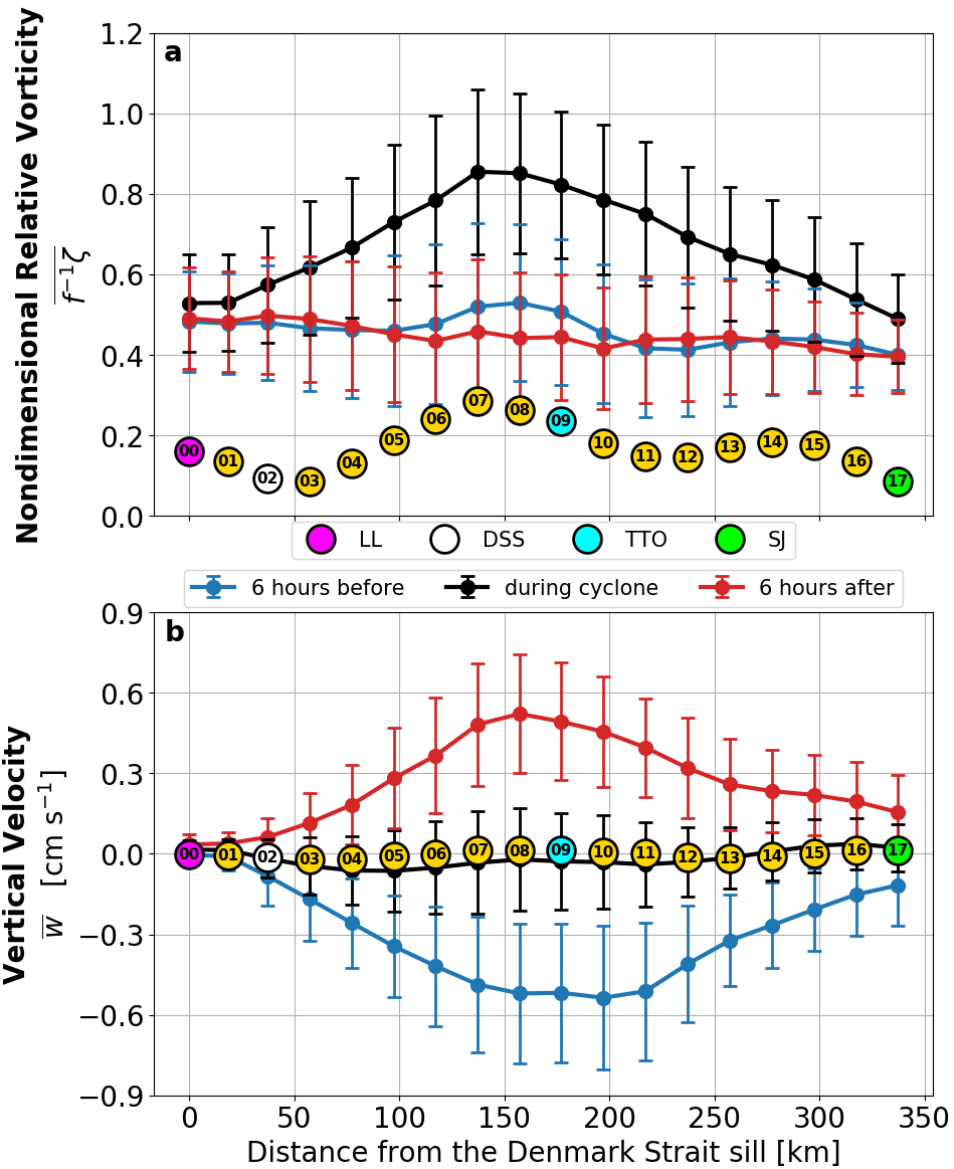


Figure 3.10: Composites of area-weighted mean (a) nondimensional relative vorticity and (b) vertical velocity along the DSO path. Positive (negative) vertical velocities correspond to upwelling (downwelling). Lines in black (a, b) correspond to composites of DSO cyclones. Blue and red lines correspond to composites in the regions of the vortices 6 hours before and after the detection, respectively. Error bars represent the area-weighted standard deviation. Labeled circles correspond to composites of yearly averages in the regions of the vortices (background state). The color code and labeling convention of the DSO stations are the same as used in Figure 3.5. Fields have been extracted along the σ -level at a depth of $5H/8$.

at the bottom. As a result, the mid-level layer is stretched the most, and the relative vorticity peaks near the σ -level along which we extracted the properties of the cyclones. Downstream of station #07, the background relative vorticity decreases as the DSO descends into the Irminger Basin, while the height of the water column continually increases from stations #00 to #17. Therefore, PV conservation is not the dominant mechanism in the region beyond 150 km downstream of the Denmark Strait sill (past station #07).

The composites of relative vorticity show the growth and decay phases of the DSO cyclones (black line in Figure 3.10a). The growth phase of the DSO cyclones occurs within the first 150 km downstream of Denmark Strait. The decay phase takes place between station #08 and the southernmost station. Near the latter, the relative vorticity of the cyclones is similar to $\overline{f^{-1}\zeta}$ of the cyclones detected near the northernmost station. The DSO cyclones growth and decay phases are also evident in the vertical component of the velocity field (w ; Figure 3.10b). There is a clear signal in the vertical velocities immediately before and after the detection of the cyclones (blue and red lines, respectively). Six hours before the detection of DSO cyclones, the regions occupied by the vortices are characterized by downwelling ($w < 0$). Conversely, upwelling occurs six hours after the detection. This characteristic behaviour has been also found in the the spilling events analyzed by Magaldi et al., 2011.

The Ertel PV can be approximated as follows (Klinger and Haine, 2019):

$$\text{PV} \approx (f + \zeta) \frac{N^2}{g}, \quad (3.3)$$

where N is the Brunt-Väisälä frequency, and g is the gravitational acceleration.

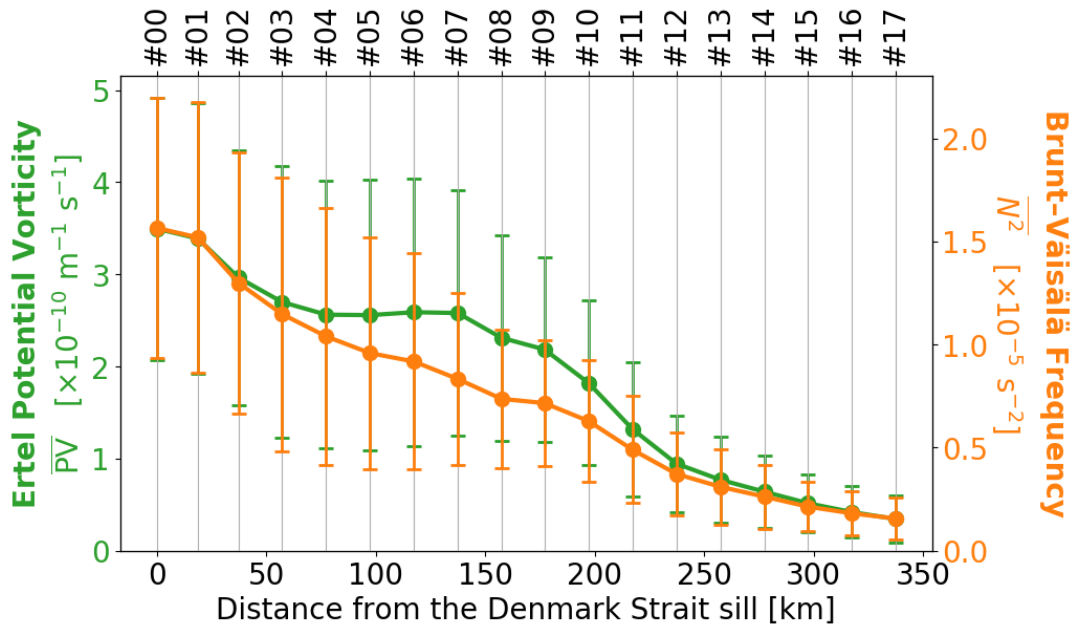


Figure 3.11: Composites of area-weighted mean Ertel Potential Vorticity (green, left vertical axis) and Brunt-Väisälä frequency (orange, right axis) along the DSO path. Error bars represent the area-weighted standard deviation. Fields have been extracted along the σ -level at a depth of $5H/8$.

The variability of the PV is controlled by the changes in N^2 and ζ along the DSO path. The Brunt-Väisälä frequency, which is defined by $N^2 = -\frac{g}{\rho_0} \frac{\partial \sigma_\theta}{\partial z}$, decreases as the cyclones move downstream (orange curve in Figure 3.11). Therefore, the water in the mid-level layer becomes less stratified as the cyclones descend into the Irminger Basin. The PV of the DSO cyclones (green curve in Figure 3.11) is strongly affected by the decrease of N^2 . However, during the growth stage of the DSO cyclones (between stations #03 and #07), the high relative vorticity of the eddies counterbalances the low stratification due to the stretching of the water column. In particular, the PV only changes by $0.12 \times 10^{-10} \text{ m}^{-1} \text{ s}^{-1}$ in this region. It follows that, downstream of the DSS station (#02), the PV associated with the DSS cyclones is only conserved

during the growth phase.

3.4 Summary and discussion

This chapter focuses on mesoscale anomalies characteristic of the dense overflow descending from Denmark Strait into the Irminger Basin. We use a high-resolution realistic general circulation model to investigate dynamically relevant quantities associated with these anomalies, including the Ertel PV, the Brunt-Väisälä frequency, the relative vorticity, and the strain rate.

The two dominant mesoscale features at the Denmark Strait sill – boluses and pulses – are detected using the objective method outlined in Chapter 2. DSO cyclones, the mesoscale features controlling the variability downstream of Denmark Strait, are identified along terrain-following levels using a vortex detection algorithm based on the OW parameter. The statistics of boluses and pulses in the model are in good agreement with their description provided by von Appen et al., 2017. We find that boluses are coupled with positive relative vorticity events, whereas pulses are coupled with anticyclonic relative vorticity events. Specifically, more than 70% of the cyclones (anticyclones) near the sill occur within 48 hours of a bolus (pulse), and the seasonal distribution of boluses (pulses) across the year matches the frequency of occurrence of the cyclones (anticyclones). Furthermore, composite vertical sections of cyclones and anticyclones at the sill are consistent with the properties of boluses and pulses, respectively. Regardless of their initial sense of rotation, both boluses and pulses trigger the formation of DSO cyclones downstream of Denmark Strait. These findings are consistent with the one-to-one relationship between

high-transport events and [DSO](#) cyclones hypothesized by von Appen et al., 2017.

The cyclonic relative vorticity associated with boluses initially increases as these features move downstream. In agreement with Spall and Price, 1998 and von Appen et al., 2014b, the additional positive relative vorticity gained by these mesoscale features can be explained using conservation of [PV](#) arguments. Specifically, the generation of cyclonic vorticity results from the pronounced stretching of the mid-level layer above the [DSO](#) interface, where [DSO](#) cyclones are detected. Interestingly, we find that the mechanisms controlling the formation of [DSO](#) cyclones associated with pulses are different. The along-stream direction of pulses is oriented toward Greenland compared to the orientation of boluses. As the pulses approach shallower regions, their negative relative vorticity is sustained by compression of the water column. The pulses slow down and begin to collapse near the East Greenland shelfbreak. Simultaneously, bands of positive relative vorticity surround the anticyclones. As the anticyclones weaken, the peripheral bands of positive relative vorticity strengthen and trigger the formation of [DSO](#) cyclones to the southwest. Then, the [DSO](#) cyclones associated with pulses move southward following the [DSO](#) path, and gain cyclonic relative vorticity in order to conserve their [PV](#). Regardless of their mechanism of formation, the [DSO](#) cyclones detected are found to have similar geometry and strength.

The relative vorticity of the cyclones increases over the first 150 km downstream of the sill, then decreases. The eddies are preceded by downwelling and followed by upwelling, meaning that the leading (trailing) edge of the

cyclones is directed downslope (upslope). The highest vertical velocities coincide with the peak of the cyclones' vorticity. The mean stratification of the DSO cyclones decreases during their full life cycle, while their initial increase in relative vorticity due to stretching is followed by a decrease. As a result, the growth and decay phases of the cyclones are associated with different dynamics, and PV is only materially conserved in the first 150 km downstream of Denmark Strait.

Dense overflows are ubiquitous features in the World Ocean, and our findings could apply to other regions, including the Strait of Gibraltar, the Faeroe Bank Channel, and the Strait of Sicily. An open question is why the PV associated with DSO cyclones is only conserved during their growth phase. Girton and Sanford, 2003 and Voet and Quadfasel, 2010 described an increase in DSO entrainment in the region where we find the transition from DSO cyclone growth to decay. In this same region, Koszalka et al., 2017 found the largest warming rate of the overflow. The decrease in PV can only be explained by diabatic and frictional processes. Therefore, these abrupt changes, combined with the enhanced entrainment and dissipation rates associated with high-transport events (i.e., boluses and pulses; North et al., 2018), might dictate which dynamics dominate the DSO cyclones' evolution at different stages of their life cycle. Further work using a combined Lagrangian-Eulerian approach is needed to fully characterize the three-dimensional structure of the DSO cyclones, and to understand how the processes discussed in this chapter affect the variability downstream of our study region, between the SJ section and the southern tip of Greenland.

Chapter 4

East Greenland Current variability north of the strait

The along-stream decrease in temperature of the Atlantic-origin Water carried by the [East Greenland Current \(EGC\)](#) intensifies rapidly south of a breakpoint located at 69°N. We find that the enhanced modification is related to the bifurcation of the [EGC](#) and is regulated by the eddy activity downstream of the breakpoint. The model reveals that large eddy activity corresponds to an offshore shift of the surface freshwater layer characteristic of the East Greenland shelf. The strength of the eddy activity regulates the density and the hydrographic properties of the [Denmark Strait Overflow Water \(DSOW\)](#) transported by the [EGC](#) system.

This chapter is published by the *Journal of Physical Oceanography* (Håvik et al., 2019). Here we discuss in more detail results based on the high-resolution, realistic, general circulation model that support and extend the observational analysis presented in the paper.

4.1 Introduction

The shelfbreak EGC is the strongest current flowing into Denmark Strait (Våge et al., 2013; Harden et al., 2016). However, the EGC system exhibits high temporal and spatial variability. The variability is more pronounced at the northern end of Blosseville Basin. In this region the shelfbreak EGC periodically bifurcates and a second branch, the separated EGC, flows southward along the base of the Iceland slope (Figure 4.1). Våge et al., 2013 and Harden et al., 2016 proposed two possible mechanisms controlling the separation of the EGC. (i) One hypothesis suggests that the separated EGC is the easternmost part of an intermittent anticyclonic gyre, which is induced by negative wind stress curl across Blosseville Basin. (ii) The second hypothesis suggests that baroclinic instabilities arising at the northern end of Blosseville Basin generates a train of eddies. These eddies then coalesce along the base of the Iceland slope forming the separated EGC.

The Atlantic Water transiting northward through the eastern Nordic Seas is modified by heat and salt fluxes. The modified Atlantic Water, which merges with the EGC below the fresh Polar Surface Water (PSW), is one of the largest component of the DSOW (Mauritzen, 1996; Eldevik et al., 2009). In line with previous studies (e.g., Våge et al., 2011), we use the term Atlantic-origin Water for all intermediate water masses with a potential temperature warmer than 0°C. This is mostly recirculated Atlantic Water from Fram Strait, although part of it is Atlantic Water which has circulated around the Arctic Ocean (Buch et al., 1996; Mauritzen, 1996; Rudels et al., 2002; Rudels et al., 2005).

The Atlantic-origin Water can be recognized in the EGC by the intermediate

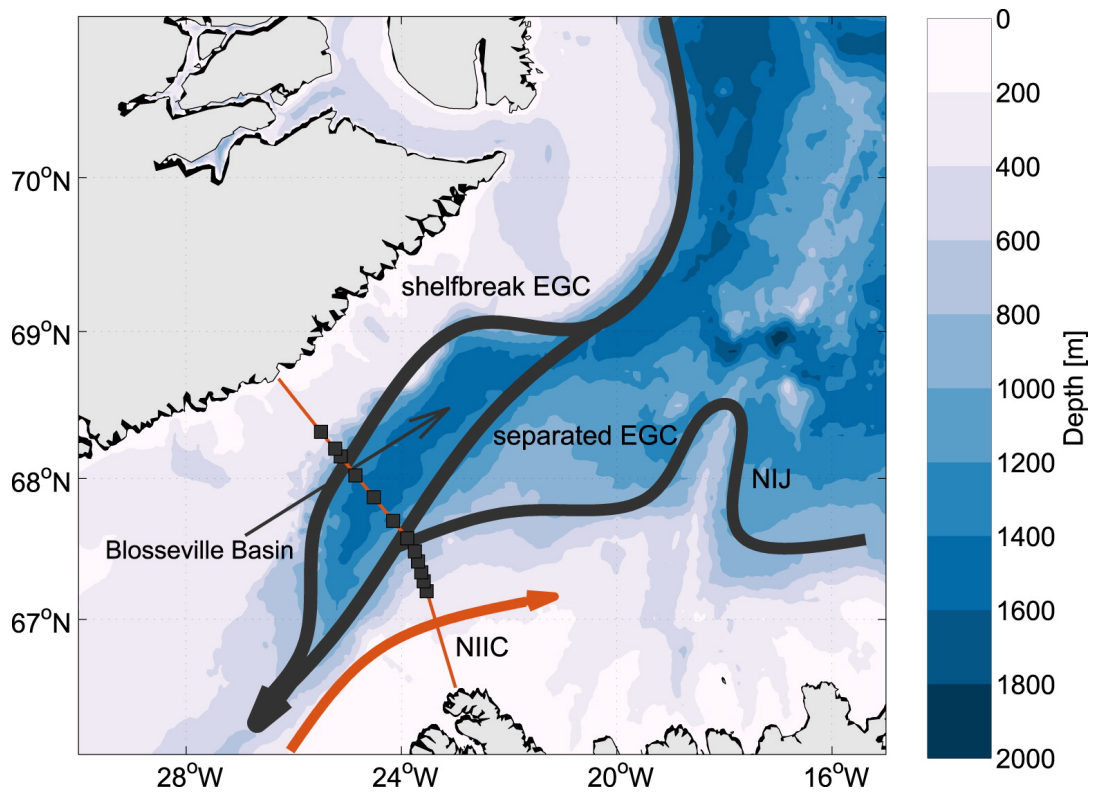


Figure 4.1: Schematic overview of the currents flowing across the Kögur mooring array marked by the orange line between Greenland and Iceland. The abbreviations are East Greenland Current (EGC), North Icelandic Jet (NIJ), North Icelandic Irminger Current (NIIC).

temperature and salinity maxima. As the hydrographic properties of the water masses transported by the [EGC](#) are modified during the transit from Fram Strait to Denmark Strait, the local maxima vary with latitude. The intermediate water masses are modified through (i) isopycnal mixing with the water masses in the interior of the basin ([Strass et al., 1993](#)), and (ii) direct contact with the atmosphere ([Våge et al., 2018](#)). These modifications might affect the density of the [DSOW](#), and ultimately the large-scale circulation of the North Atlantic and the strength of the [Atlantic Meridional Overturning Circulation \(AMOC\)](#).

In this chapter, we characterize the variability of the [EGC](#) system and investigate the mechanisms associated with the formation of the separated [EGC](#). Specifically, we integrate our high-resolution, realistic, general circulation model forced by the [Arctic System Reanalysis version 2 \(ASRv2; Bromwich et al., 2018\)](#) with several observational datasets analysed by [Håvik et al., 2019](#) (see [Chapter 2](#) for more details about the model configuration). Our ultimate goal is to improve the understanding of the connection between the processes modifying the Atlantic-origin Water and the kinematic structure of the [EGC](#) upstream of Denmark Strait. The chapter is organized as follows: In [Section 4.2](#) we compare the model circulation upstream of Denmark Strait with high-resolution measurements. In addition, we characterize the variability of the Atlantic-origin Water carried by the [EGC](#) throughout the year simulated by the model, and we compare the properties of the intermediate layer with historical hydrographic profiles. In [Section 4.3](#) we investigate the variability of the Atlantic-origin Water, relating it to the kinematic structure of the [EGC](#)

system. Finally, we summarize our findings in Section 4.4, where we also discuss the mechanisms associated with the bifurcation of the EGC and possible implications for the large-scale circulation in the North Atlantic.

4.2 Comparison with observations

4.2.1 The Kögur mooring array

To assess the realism of the circulation upstream of Denmark Strait in the model we compare the simulated velocity field with current speeds measured by the Kögur mooring array (<http://kogur.who.edu>; Harden et al., 2016). The array consists of 12 moorings distributed from the outer East Greenland shelf to the Iceland shelfbreak (Figure 4.1). The moorings were deployed from September 2011 to August 2012 and captured the vast majority of the water feeding the Denmark Strait Overflow (DSO).

The yearly-averaged cross-sectional current speeds from the model agree well with the mooring array data (Figure 4.2). The strength of the simulated shelfbreak EGC (Figure 4.2b) is consistent with the measurements (Figure 4.2a), although the model exhibits a wider current. The combination of the separated EGC and the North Icelandic Jet (NIJ) manifests as a surface-intensified current. The core of this southward flow is located on the Iceland slope, approximately above the 600-800 m isobaths. The negative velocities (northwestward) at the upper Iceland slope corresponds to the North Icelandic Irminger Current (NIIC).

The model is generally less dense than the observations, which is consistent with the biases in Denmark Strait discussed in Chapter 2. The characteristic

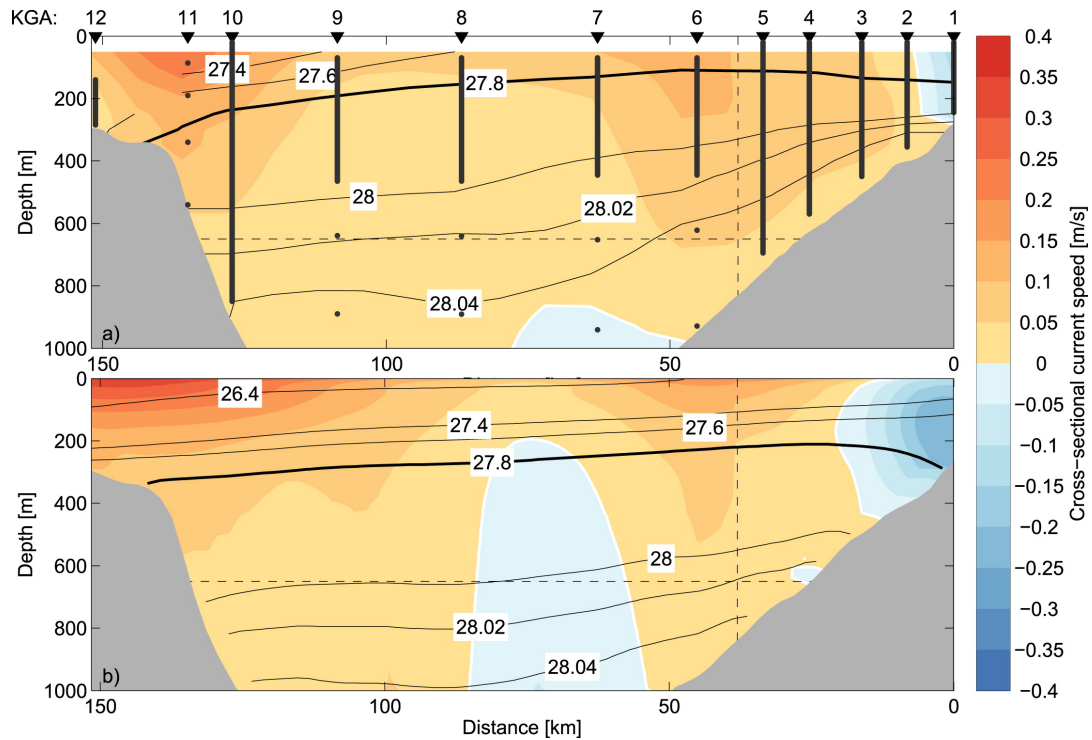


Figure 4.2: Comparison of the mean cross-sectional current speed in (a) the mooring observations and (b) the model at Kögur (see Figure 4.1). Positive current speeds are toward the southwest and distance is increasing along the x -axis from the eastern-most mooring near the Iceland shelfbreak. On top of (a) the mooring locations are numbered (KGA 1-12), and the measurement levels on each mooring are marked by black dots. A selection of isopycnals is contoured in both panels, and the upper limit of DSOw, the 27.8 kg m^{-3} isopycnal, is marked by the thick black contour. The horizontal dashed line indicates the sill depth at Denmark Strait (650 m), and the vertical dashed lines mark the location where the orientation of the transect changes. The data from the mooring array are interpolated using a Laplacian-spline interpolator, and the data from the model are linearly interpolated in the horizontal. The viewer is looking to the north.

divergence of the isopycnals associated with the NIJ is also less pronounced in the model compared to observations (Våge et al., 2011; Harden et al., 2016). As this chapter focuses on the shelfbreak and separated branches of the EGC, we conclude that the model represents well the kinematic structure upstream of Denmark Strait.

4.2.2 Historical hydrographic profiles

The Atlantic-origin Water is the warmest component of the DSO. We identify the Atlantic-origin Water in the EGC by locating the maximum temperatures below the overflow interface along the 700 m isobath (for more details, see Håvik et al., 2019). In line with previous studies, the DSO interface corresponds to $\sigma_\theta = 27.8 \text{ kg m}^{-3}$ ($\sigma_\theta = \rho - 1000 \text{ kg m}^{-3}$; Dickson and Brown, 1994).

In agreement with the historical hydrographic profiles collected from 1980 to 2014 (Våge et al., 2015), the yearly mean maximum temperature of the Atlantic-origin layer decreased from north to south in the model (black line in Figure 4.3). The temperature decrease can be explained by the exchanges with the neighboring water masses, which are of polar and Arctic origin and therefore colder. However, the model shows a narrower temperature range and a weaker decrease (0.04°C per degree of latitude on average compared to 0.1°C per degree of latitude). We note that the model simulated one year only, whereas the measurements along the East Greenland shelfbreak are spread over 35 years but biased toward late summer. The weaker decrease from north to south of the yearly-mean maximum temperature in the model is due to a

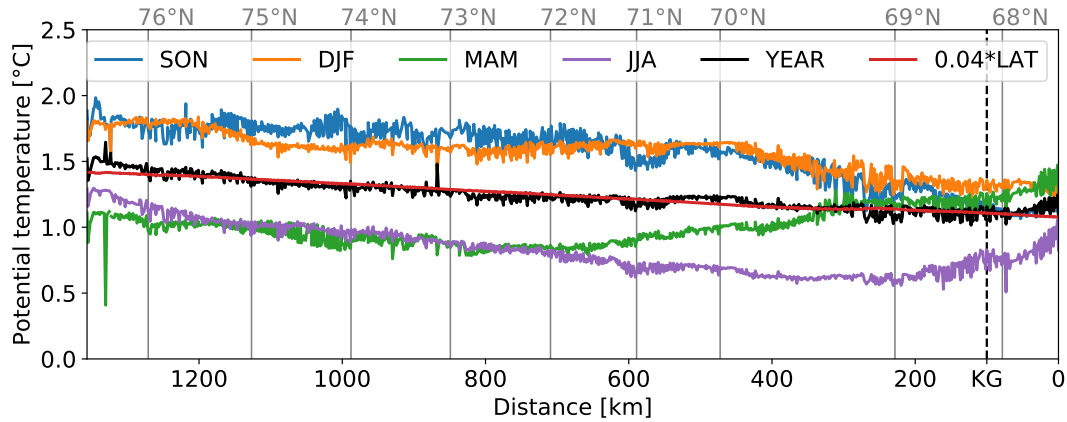


Figure 4.3: Maximum temperature of the Atlantic-origin Water along the 700-m East Greenland isobath averaged over 3-month periods. The black solid line corresponds to the yearly averaged temperatures. The red line is the linear fit of the yearly averaged temperatures. Larger distances correspond to higher latitudes, as shown by the vertical lines. The dashed vertical line marks the latitude of the Kögur section. The 3-month acronyms for seasons are: [September-October-November \(SON\)](#); [December-January-February \(DJF\)](#); [March-April-May \(MAM\)](#); [June-July-August \(JJA\)](#).

pronounced variability characterized by the seasonal time scale (Figure 4.3). In [September-October-November \(SON\)](#) and [December-January-February \(DJF\)](#) the intermediate temperature maximum decreases from north to south in the year simulated by the model. The rate of change in temperature is stronger in these months compared to the yearly mean trend, and is consistent with the trend estimated from observations. However, in [March-April-May \(MAM\)](#) the temperature of the Atlantic-origin Water rapidly decreases only in the northern region, and the along-stream temperature change is not monotonic (i.e., the maximum temperature of the intermediate layer first decreases, then increases). The negative temperature trend from north to south along the EGC path is almost completely reestablished in [June-July-August \(JJA\)](#), but the temperatures of the simulated Atlantic-origin Water are lower compared to the measurements. As the observations are particularly sparse in the seasons

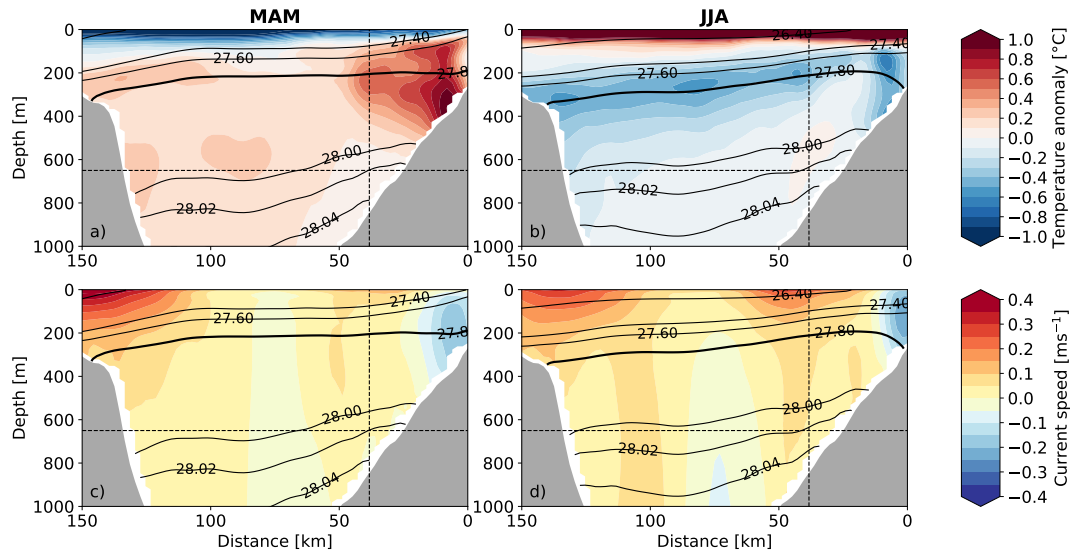


Figure 4.4: Temperature anomalies from the annual mean in (a) **March-April-May (MAM)** and (b) **June-July-August (JJA)** in the model at Kögur. (c) and (d) show the cross-sectional current speed in **MAM** and **JJA**, respectively. A selection of isopycnals is contoured in all panels, and the upper limit of the **DSOW** is marked by the thick black contour. The vertical dashed lines mark the location where the orientation of the transect changes (see Figure 4.1). The horizontal dashed lines mark the depth of the Denmark Strait sill. The viewer is looking to the north.

where the model shows a strong deviation from the yearly average, it is not possible to establish whether or not this is a realistic representation of the **EGC** variability.

In the upstream region, the maximum temperature of the **DSOW** is particularly low in **MAM** and **JJA** (Figure 4.3). A similar cooling occurs in the downstream region in **JJA** only. Therefore, there is a time-lag between the upstream and downstream modification of the Atlantic-origin Water. In Figures 4.4a and 4.4b, we show temperature anomalies from the annual mean in (a) **MAM** and (b) **JJA** at Kögur. The surface layer is characterized by cold (warm) anomalies in **MAM** (**JJA**). By contrast, the model reveals subsurface

warming (cooling) in **MAM** (**JJA**). These positive and negative anomalies originate at different locations and appear to be related to the kinematic structure of the currents flowing across the vertical section. In **MAM**, the warmest anomalies are located on the Iceland shelfbreak and spread west. The core of the positive temperature anomalies coincides with the core of the **NIIC**, which carries subtropical warm water into Blosseville Basin. The **NIIC** simulated by the model in **MAM** is robust and slightly shifted west (Figure 4.4c). In **JJA**, the cold anomalies are concentrated at the edge of the Iceland shelf and in a band extending across the entire basin. The anomalies on the Iceland side of the section are consistent with the eastward shift of the **NIIC**, whereas the anomalies at the interface of the overflow might be associated with the weakening (strengthening) of the shelfbreak (separated) **EGC** (Figure 4.4d). The relation between the temperature of the Atlantic-origin Water and the kinematic structure of the **EGC** system is further investigated in Section 4.3.

4.3 Results

4.3.1 Relationship between eddy activity and temperature of the intermediate layer

In this section we investigate the **Eddy Kinetic Energy (EKE)** variability associated with the maximum temperature of the **DSOW** along the **EGC** path. **EKE** is computed separately at each grid point along the 700-m isobath. The temporal mean **EKE** is defined as follows:

$$\text{EKE} = \frac{1}{2} \overline{[(\bar{u} - u)^2 + (\bar{v} - v)^2]} \quad , \quad (4.1)$$

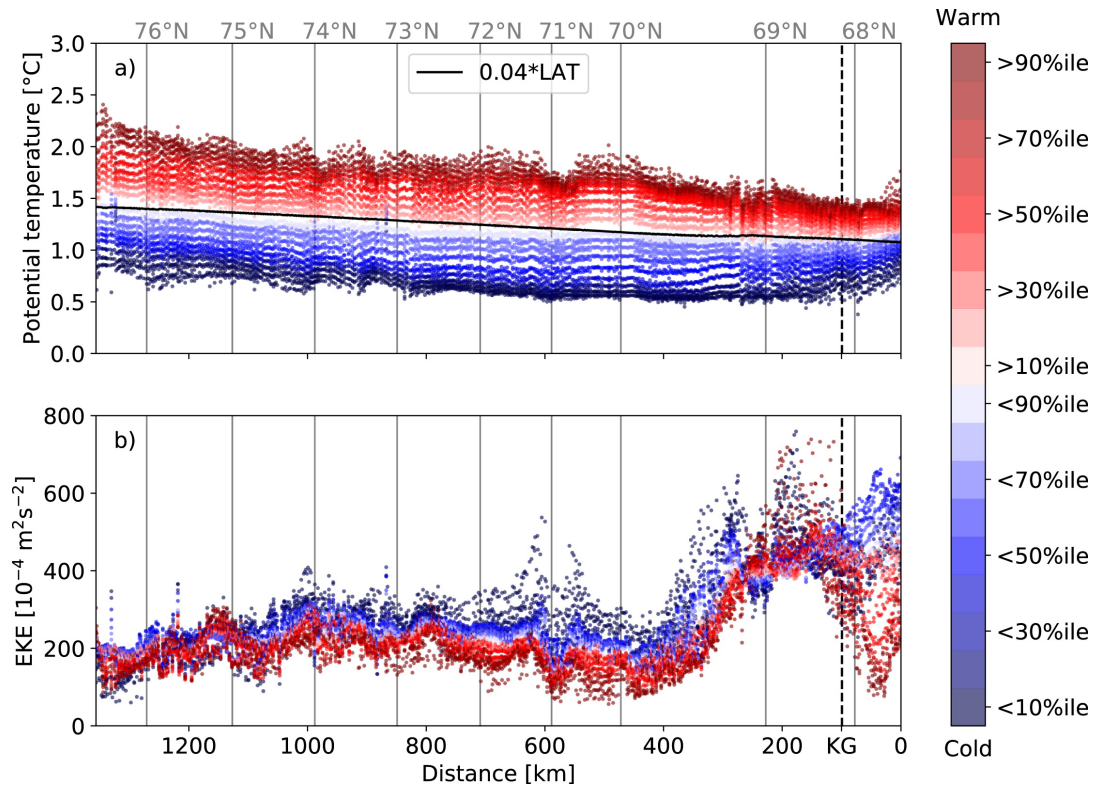


Figure 4.5: (a) Average temperature of the Atlantic-origin Water along the shelfbreak EGC path computed for water warmer (red) and colder (blue) than a range of local percentiles (color bar), and (b) corresponding EKE. The black solid line in (a) is the linear fit of the yearly averaged temperatures. Larger distances correspond to higher latitudes, as shown by the vertical lines. The dashed vertical lines mark the latitude of the Kögur section.

where overlines indicate temporal averages, u is the zonal current speed, and v refers to the meridional current speed.

Figure 4.5 shows the (a) average temperature and (b) EKE of the Atlantic-origin Water along the isobath followed by the shelfbreak EGC. To investigate the cause/effect relationships between eddy activity and water mass modification, we separate the Atlantic-origin Water into warm (red) and cold (blue) modes. Different modes are defined by local percentiles. North of approximately 69.5°N the EKE along the 700-m isobath is low compared to further

south (Figure 4.5). Although the cold mode is generally associated with enhanced eddy activity, the warm and cold modes of the Atlantic-origin Water exhibit similar *EKE* values in the upstream region. By contrast, there is a clear relationship between the core temperature of the Atlantic-origin Water and the strength of the eddy activity in the southern part of the shelfbreak *EGC*. Specifically, the two modes show opposite behaviour south of 68.5°N: The strength of the eddy activity associated with the cold (warm) mode increases (decreases) as the *EGC* approaches Denmark Strait.

The historical hydrographic measurements analysed by Håvik et al., 2019 show a breakpoint (i.e., a change in *EGC* characteristics) located near 69°N. The breakpoint is located in a region characterized by a sharp bend in bathymetry and atmospheric forcing, and coincides with the region where the *EGC* bifurcates. South of the breakpoint, the measured Atlantic-origin Water temperature decreases very rapidly. The model *EKE* shown in Figure 4.5b confirms the existence of a breakpoint around 69°N, and corroborates the hypothesis based on observations that eddies play a key role in the separation of the *EGC*.

To further investigate the relationship between the temperature modes and *EKE*, we construct model composites at the Kögur transect. The composites are obtained by separating the Atlantic-origin Water in the shelfbreak *EGC* into a warm and cold mode (Figure 4.6). The offshore limit of the shelfbreak *EGC* corresponds to the location of the mooring KGA 8 (Figure 4.2a). In step 1, we calculate the cross-sectional area covered by warm and cold Atlantic-origin Water in the shelfbreak *EGC*. The threshold used to distinguish warm and cold Atlantic-origin Water is set to 1°C. The same threshold is used by Håvik

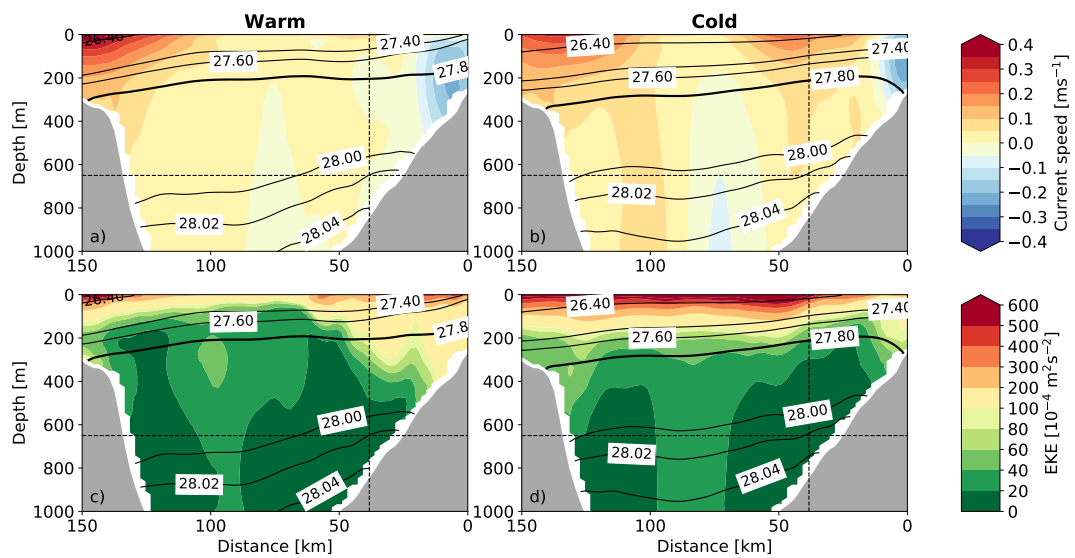


Figure 4.6: Cross-sectional current speed at Kögur during (a) the warm mode and (b) the cold mode in the model. (c) and (d) show the EKE during the warm and cold modes, respectively. Note the nonlinear color bar in (c) and (d). A selection of isopycnals is contoured in all panels, and the upper limit of the DSOW is marked by the thick black contour. The vertical dashed lines mark the location where the orientation of the transect changes (see Figure 4.1). The horizontal dashed lines mark the depth of the Denmark Strait sill. The viewer is looking to the north.

et al., 2019 to perform a similar composite analysis on the observations. It is important to note that the threshold is consistent with the median temperature of the Atlantic-origin Water in the model at Kögur (Figure 4.5a). In step 2, we construct vertical sections of cross-sectional current speed (Figures 4.6a and 4.6b) and EKE (Figures 4.6c and 4.6d) of the periods when one mode dominates the other. The composites show that during warm conditions the shelfbreak EGC is the most pronounced circulation feature across the section (Figures 4.6a), while the separated branch is weak. The corresponding EKE is large in the core of the shelfbreak EGC, and is low further offshore (Figures 4.6c). On the other hand, the separated EGC emerges in the composite vertical section corresponding to the cold mode (Figures 4.6b). In contrast with the warm mode, strong EKE values are present across the entire Blossville Basin (Figures 4.6d) and the largest values coincide with the core of the separated EGC.

4.3.2 Relationship between eddy activity and salinity of the surface layer

We show maps of key surface properties averaged over time in Figures 4.7a, 4.7b, and 4.7c. The mean current speed in the upper 100 m indicates a strong shelfbreak EGC upstream of the Kögur transect (Figure 4.7a). Its average speed exceeds 0.4 m s^{-1} . The core of the shelfbreak EGC weakens progressing southward, and a broader region with enhanced current speed emerges on the East Greenland shelf and near the Denmark Strait sill. The yearly mean velocities do not show a distinct separated EGC as this current is characterized by high fluctuation in time and space (Harden et al., 2016).

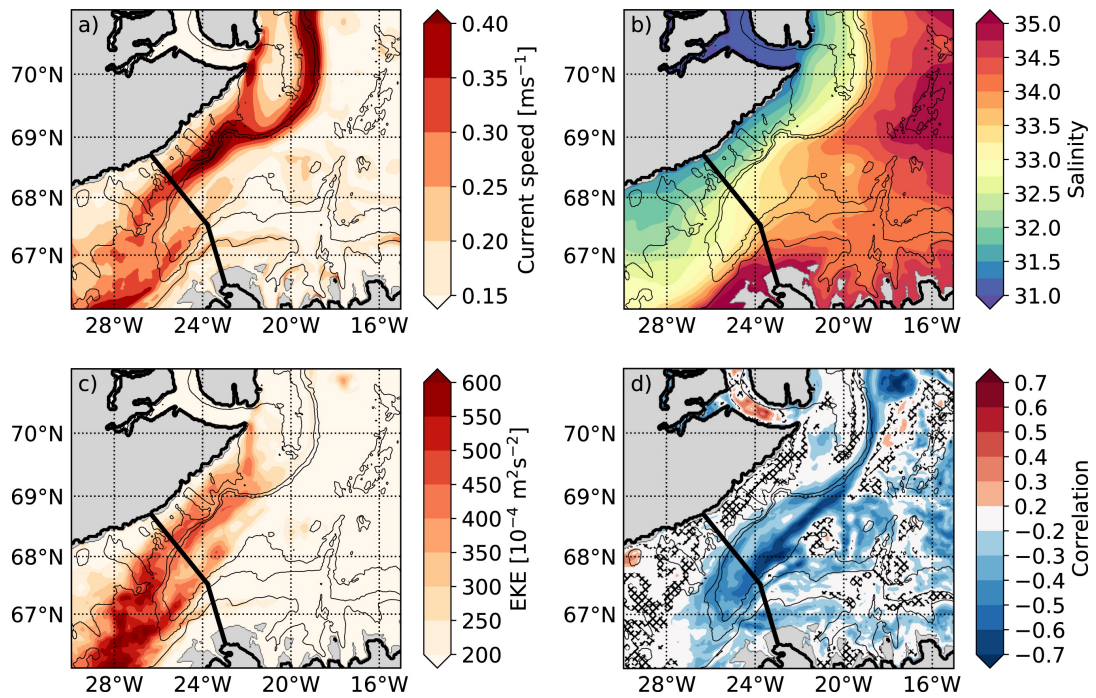


Figure 4.7: Mean (a) horizontal current speed $\left(\sqrt{u^2 + v^2}\right)$, (b) salinity, (c) *EKE*, and (d) Pearson correlation coefficient between salinity and *EKE* in the model over the upper 100 m. The black lines indicate the location of the Kögur transect. The gray contours are 300-, 700-, 1000-, and 2000-m isobaths from the model. Areas shallower than 100 m are masked gray. Hatched areas are not significant at the 5% level (p values < 0.005).

The average surface salinity field (Figure 4.7b) highlights the front between different water masses. The fresh PSW is located on the Greenland shelf, whereas salty water is located offshore. Both the fresh and salty water masses are located near the shelfbreak in the region north of the breakpoint ($\sim 69^\circ\text{N}$). By contrast, south of the breakpoint, the fresh water spreads east of the shelfbreak and the front is weak.

The EKE field shows an enhanced eddy activity south of 69°N (Figure 4.7c), which is consistent with our findings described in Section 4.3.1. Both the order of magnitude and location of the enhanced EKE are consistent with estimates from satellite altimetry (Håvik et al., 2017). The eddy activity is also enhanced south of approximately 68.2°N . As the EKE is particularly strong at the eastern end of Blossville Basin, the model suggests that the eddies erode the shelfbreak EGC, coalesce along the base of the Iceland slope, and form the separated EGC.

We compute the correlation between EKE and salinity at each grid point to investigate the link between the eddy activity, salinity, and kinematic structure of the EGC system in the upper-ocean (Figure 4.7d). We perform two separate tests to estimate the significance of the Pearson correlation coefficients. (i) The first method identifies where the correlation coefficients are not significant at the 5% level (p values < 0.05). Slashes in Figure 4.7d indicate the grid points that do not pass this test. (ii) The second method is based on Wilks, 2016 and is more robust to the effects of spatial correlation. Wilks, 2016 has shown that, when the spatial correlation is moderate or strong, $\alpha_{\text{FDR}} = 2\alpha_{\text{global}}$ is the control level required to perform a solid False Discovery Rate (FDR) test.

Therefore, we choose to set $\alpha_{\text{FDR}} = 0.1$. Backslashes in Figure 4.7d indicate correlation values that do not pass this test.

The correlation coefficients passing the significance tests reveal that enhanced eddy activity is associated with low salinities at the eastern end of Blosseville Basin (Figure 4.7d). This is consistent with the hydrographic measurements at Kögur analyzed by Håvik et al., 2019, which show that the fresh PSW is shifted eastwards when the cold mode of the Atlantic-origin Water dominates. On the other hand, lower EKE is associated with the warm mode of the Atlantic-origin Water and higher salinities. Interestingly, we find a particular strong anticorrelation (~ -0.7) in an elongated band along the base of the Iceland slope. This band overlaps the region where the separated EGC flows.

4.4 Summary and discussion

We use a high-resolution, realistic, general circulation model to investigate the link between the eddy activity, salinity, and kinematic structure of the EGC. This study supports and extends the observational analysis performed by Håvik et al., 2019.

In agreement with observations, the yearly mean temperature of the Atlantic-origin layer in the shelfbreak EGC decreases from north to south. The EKE associated with the intermediate Atlantic-origin Water confirms the existence of a breakpoint around 69°N , south of which Håvik et al., 2019 found an enhanced reduction in temperature of the Atlantic-origin layer. The strong modification south of the breakpoint appears to be the result of enhanced

mixing, which is associated with the bifurcation of the EGC at the northern end of Blosseville Basin.

At Kögur, we find that a relatively warm Atlantic-origin Water is transported by the shelfbreak EGC, whereas the separated EGC transports a more modified and therefore colder Atlantic-origin Water. The total transport (volume flux) of the EGC system is similar during the two modes, but the relative contribution of the separated branch is larger during the cold mode. This supports the hypothesis based on observations that the separated EGC results from a bifurcation of the shelfbreak EGC. In addition to the more vigorous mixing of the intermediate Atlantic-origin Water observed south of 69°N, the model shows that enhanced eddy activity downstream of the breakpoint is associated with fresh PSW offshore of the shelf. Therefore, the eddies are likely due to instabilities in the shelfbreak EGC and advect surface water offshore. Although cold water is generally associated with enhanced eddy activity, south of the breakpoint the EKE associated with the cold mode is twice as large as the EKE in the warm mode.

The location of the sea ice edge on the eastern side of Greenland is of critical importance. Because of the recent retreat of the sea ice edge towards Greenland, part of the Atlantic-origin Water is currently reventilated just offshore of the shelfbreak EGC (Våge et al., 2018). If the sea ice edge continues to retreat towards Greenland, the reventilation of the Atlantic-origin Water might take place directly within the core of the shelfbreak EGC. Our findings suggest that the increased modification of the Atlantic-origin Water in the shelfbreak EGC would alter the relative contribution of the EGC branches, leading to

enhanced offshore transport of fresh water. In this scenario, the density of the [DSOW](#) might change due to enhanced eddy activity and reventilation, affecting the contribution from the Nordic Seas to the deep circulation in the North Atlantic.

Chapter 5

Conclusions

5.1 Summary

This thesis presents three studies that aim at deepening the understanding of the variability characterizing the ocean circulation in the vicinity of Denmark Strait. Our findings are based on a year-long, high-resolution (~ 2 km), realistic general circulation model covering the East Greenland shelf and the Iceland and Greenland Seas. Overall, the agreement between the model and the available observations is excellent.

In Chapter 2, we focus on the high-frequency variability of the [Denmark Strait Overflow \(DSO\)](#) at the sill. We characterize the hydrography and circulation associated with boluses and pulses, which are the two dominant mesoscale features in the strait. We estimate that the yearly mean southward volume flux of the [DSO](#) is about 30% greater in the presence of boluses and pulses. On average, boluses (pulses) are 57.1 (27.5) hour long, occur every 3.2 (5.5) days, and are more frequent during the summer (winter) of the year simulated. Boluses (pulses) increase (decrease) the overflow cross-sectional

area, and temperatures around the overflow interface are colder (warmer) by about 2.6°C (1.8°C). The lateral extent of the boluses is much greater than that of the pulses. In both cases, the along-strait equatorward flow of dense water is enhanced, but more so for pulses. The [Sea Surface Height \(SSH\)](#) rises by 4-10 cm during boluses and by up to 5 cm during pulses. The [SSH](#) anomaly contours form a bowl (dome) during boluses (pulses), and the two features cross the strait with a slightly different orientation. We find that the mean direction of the [DSO](#) and the [SSH](#) anomalies are consistent with a geostrophic flow, whereas the lag between [SSH](#) anomalies and boluses/pulses is consistent with baroclinic instability. Our findings indicate that boluses and pulses play a major role in controlling the properties of the [DSO](#) flowing into the Irminger Sea.

Chapter 3 focuses on the evolution of boluses and pulses as they descend into the Irminger Basin. These mesoscale features cross Denmark Strait with the same frequency as the [DSO](#) cyclones observed farther downstream. To investigate the connection between high-transport events and cyclones, we develop an automated vortex detection algorithm and apply it to the model solutions. The model shows that both the cyclonic boluses and anti-cyclonic pulses produce [DSO](#) cyclones, but the underlying mechanisms are different. Cyclones associated with boluses form at the Denmark Strait sill and, because of potential vorticity conservation and stretching of the water column, grow as they move south. In contrast, cyclones associated with pulses form downstream of the sill, when the slow-moving anticyclones near the East Greenland shelfbreak start collapsing. Regardless of their formation mechanism, [DSO](#)

cyclones progressively weaken starting roughly 150 km downstream of the sill. The mean stratification of the cyclones decreases during their life cycle, while their initial increase in relative vorticity due to stretching is followed by a decrease. As a result, potential vorticity is only materially conserved during the growth phase. Lastly, composite averages of the [DSO](#) cyclones show that they are preceded by downwelling and followed by upwelling, and that the maximum vertical acceleration coincides with the peak of the growth phase. As the [DSO](#) cyclones interact with the dense water masses that descend into the subpolar North Atlantic, they are of critical importance for the [Atlantic Meridional Overturning Circulation \(AMOC\)](#).

In Chapter 4, we focus on the variability in the [East Greenland Current \(EGC\)](#) system upstream of Denmark Strait. In agreement with observations, the yearly mean temperature of the Atlantic-origin layer in the shelfbreak [EGC](#) decreases from north to south. The [Eddy Kinetic Energy \(EKE\)](#) associated with the intermediate Atlantic-origin Water confirms the existence of a breakpoint around 69°N , south of which observations show enhanced reduction in temperature of the Atlantic-origin layer. The strong modification south of the breakpoint is due to enhanced mixing, which is associated with the bifurcation of the [EGC](#) at the northern end of Blosseville Basin. Large eddy activity is associated with a more robust separated [EGC](#) and an offshore shift of the surface freshwater layer that characterizes the Greenland shelf. We find that the intensity of the eddy activity regulates the density and the hydrographic properties of the [Denmark Strait Overflow Water \(DSOW\)](#) transported by the [EGC](#) system. The shelfbreak [EGC](#) transports dense water masses that are

relatively warm, whereas the separated [EGC](#) transports more modified and therefore colder water masses.

5.2 Future Work

We have shown that the high-resolution, realistic, general circulation model developed for this thesis is a useful tool to interpret the sparse observations available near Denmark Strait. Although the numerical domain presented in [Chapter 2](#) includes the entire Iceland Sea to the north as well as Cape Farewell to the southwest, the configuration and the horizontal grid of the models discussed so far are designed to resolve the dynamics associated with the [DSO](#) near the sill.

The densest water masses feeding the [DSOW](#) are hypothesized to form in the Iceland Sea or the southern Greenland Sea as part of an interior overturning loop ([Våge et al., 2013](#); [Våge et al., 2015](#)). As of today, the source of these water masses remains unknown. Therefore, we set up a new configuration of the [Massachusetts Institute of Technology General Circulation Model \(MITgcm; Marshall et al., 1997\)](#) to better understand where, when, and how the densest components of the [DSOW](#) are formed. The model configuration is similar to the setup presented in [Chapter 2](#): The high-resolution, realistic, regional model solves the primitive equations of the ocean and is coupled with a sea ice model ([Losch et al., 2010](#)). The numerical domain extends from south of Cape Farewell to about 79°N, and from Greenland to the Scandinavian Peninsula and Svalbard ([Figure 5.1](#)). The maximum horizontal resolution is about 1.7 km in the Greenland Sea and decreases moving toward the edges of

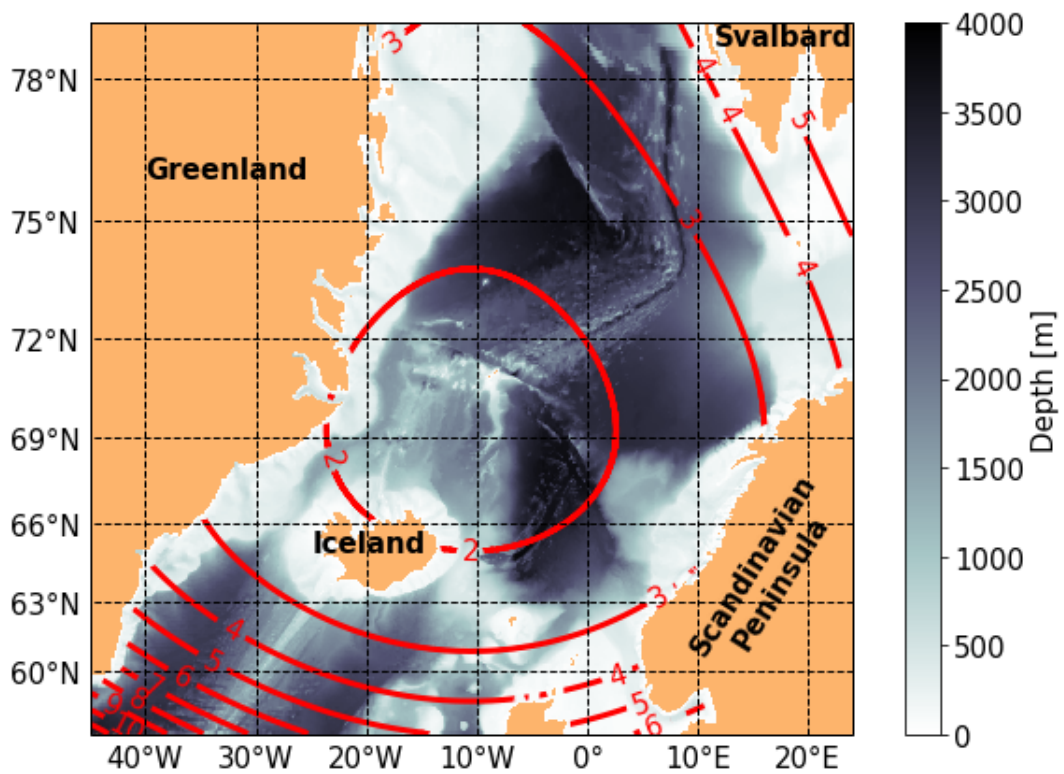


Figure 5.1: Plan view of the numerical domain of the model in support of the [Iceland Greenland Seas Project \(IGP\)](#) superimposed on seafloor bathymetry. Red lines indicate the square root of the horizontal area of the grid-cells in kilometers.

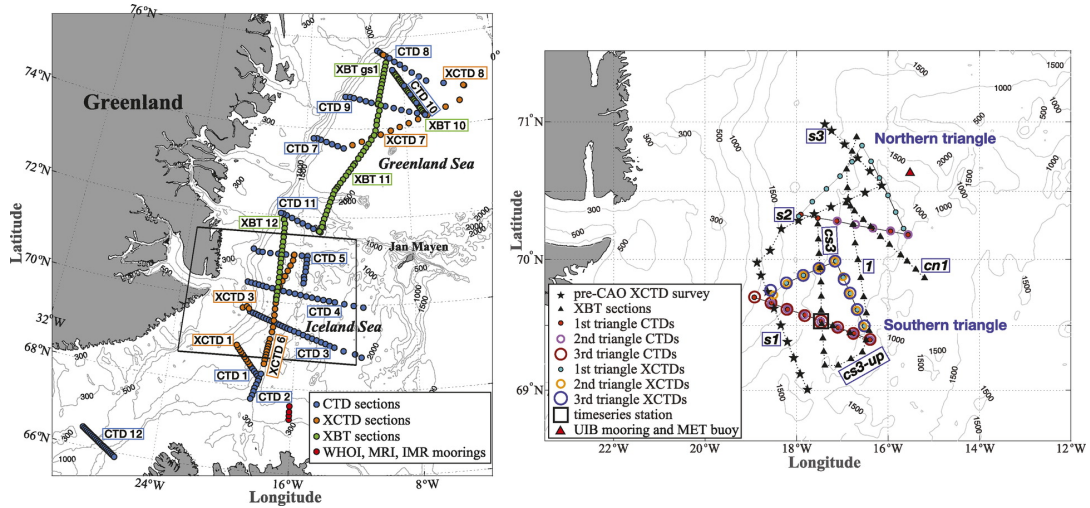


Figure 5.2: (left) The hydrographic sections occupied in the [Iceland Greenland Seas Project \(IGP\)](#). (right) The northwest Iceland Sea and the location of intensive surveys where triangular patterns or lines were repeated several times in coordination with the research aircraft. Source: Renfrew et al., 2019.

the domain. The vertical grid uses partial bottom cells and the rescaled height coordinates z^* (Adcroft et al., 2004). The vertical resolution linearly increases from 2 to 19 m in the upper ~ 200 m and is 19 m thereafter.

In February-March 2018, a 43-day cruise in the northwest Iceland Sea and southwest Greenland Sea collected data to investigate the location and causes of dense water formation (the [IGP](#); Renfrew et al., 2019). The spatial coverage of the measurements is shown in Figure 5.2. As we plan to integrate the model solutions with the [IGP](#) observations, the year-long numerical simulation spans from September 2017 to August 2018 (after an 8-month spinup). Similarly to the model validation discussed in Chapter 2, we will perform a “virtual campaign” resembling the field campaign carried out in winter 2018. This approach will lead to a robust and detailed characterization of the model biases. The virtual campaign will be performed using OceanSpy (Almansi

et al., 2019), the open-source software developed for this thesis. Furthermore, the software will be used to calculate heat and salt budgets, which will allow to determine the relative contribution of advection, diffusion, and surface forcing to the total tendency of the tracers. Finally, we will use OceanSpy to compute accurate fluxes through vertical sections, and we will combine the results with the intensive surveys repeated along closed paths (Figure 5.2-right). This method will allow to characterize the water mass modifications occurring in the regions bounded by closed surveys.

Haine et al., 2009 found that the spatial resolution of the atmospheric fields used to force high-resolution models significantly affects the ocean circulation in Denmark Strait. The model that we will integrate with the IGP measurements is forced with heat, freshwater, and momentum fluxes derived from the ECMWF Re-Analysis version 5 (ERA5; Copernicus Climate Change Service (C3S), 2017), whereas the configurations described in Chapter 2 and 3 are forced with ERA-Interim (Dee et al., 2011) and the Arctic System Reanalysis version 2 (ASRv2; Bromwich et al., 2018), respectively. The wide-ranging spatial resolution of the atmospheric reanalyses used to force the ocean component (15, 25, and 80 km for ASRv2, ERA5, and ERA-Interim, respectively) allows to extend the analysis performed by Haine et al., 2009. Specifically, we will investigate the impact of the atmospheric forcing resolution to the circulation and ventilation further upstream of Denmark Strait.

During the IGP field campaign, the North Atlantic Oscillation (NAO) transitioned from positive to negative conditions. The NAO index (Barnston and

Levezey, 1987) switched sign on February 26, 2018. The transition to negative NAO resulted in a dramatic drop in air temperature, which explains the Cold-Air Outbreak (CAO) over the Iceland Sea that characterized the second half of the IGP campaign (Renfrew et al., 2019). Interestingly, a preliminary analysis of the model circulation at Kögur (see Figure 4.1) reveals sudden changes between February and March 2018 (Figure 5.3). In February, when the monthly mean NAO index is 1.58, both the separated and shelfbreak branches of the EGC system are robust (Figure 5.3a). By contrast, there is an anomalous northward flow at the Greenland shelfbreak in March (Figure 5.3b), when the monthly mean NAO index is -0.93. In this case, northward and southward currents alternate along the section, the North Icelandic Jet (NIJ) at the edge of the Iceland shelf is enhanced, and most of the volume flux associated with the EGC system is concentrated at the center of the transect. We will establish whether or not this circulation patterns are due to the change in sign of the NAO index, extending our study focused on the variability upstream of Denmark Strait (see Chapter 4). We will also assess the effects of this anomalous circulation on the properties of the DSOW, comparing our findings with the Lagrangian analysis performed by Saberi et al., 2020 on the model solutions shown in Chapter 3 and 4. Specifically, we will further investigate the hypothesis that, when the NAO index is particularly high in winter, the contribution to the DSOW of pathways from south of Denmark Strait is relatively large.

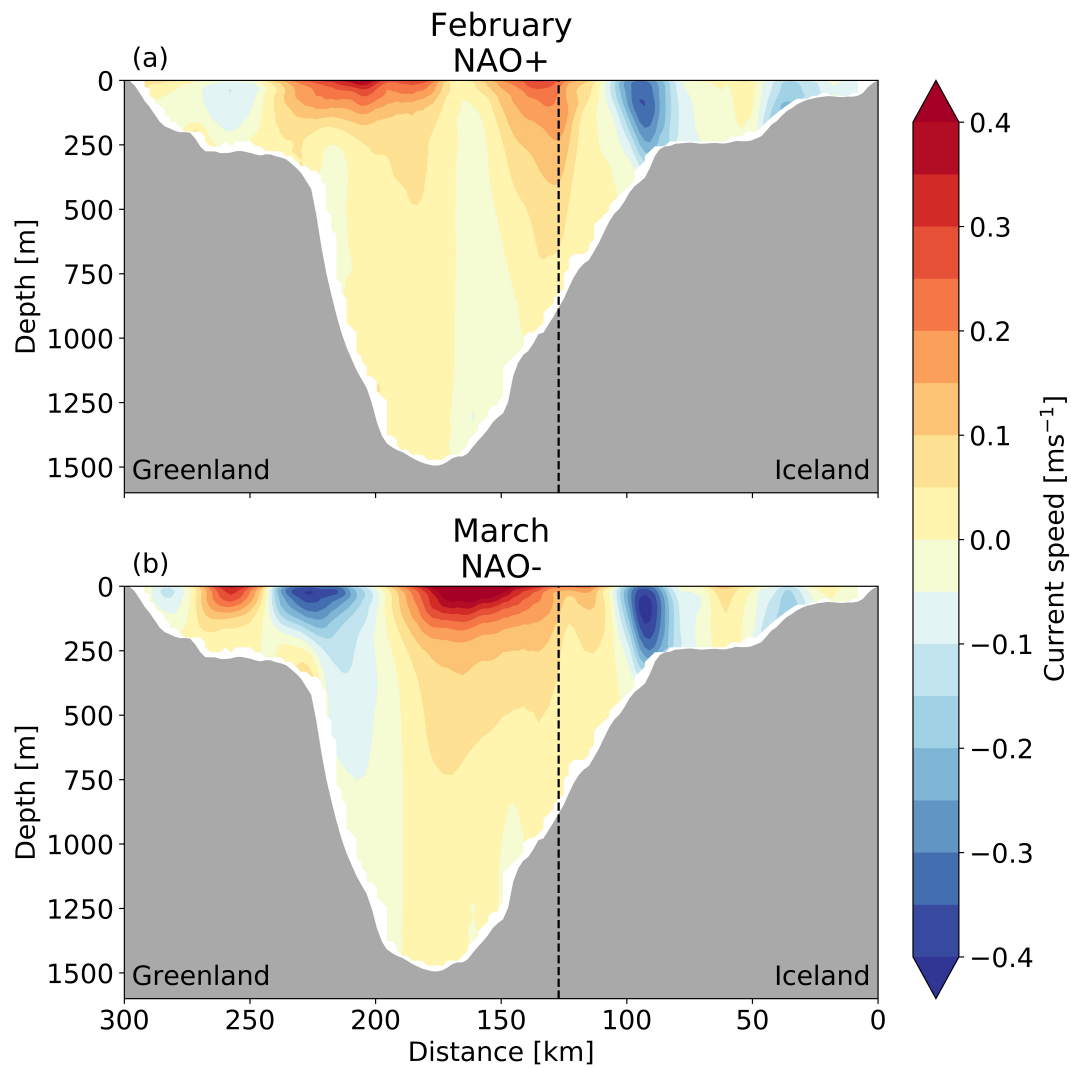


Figure 5.3: Monthly mean cross-sectional current speed in (a) February and (b) March at the Kögur section. The monthly mean NAO is positive in February and negative in March. Positive current speeds are toward the southwest. The vertical dashed lines mark the location where the orientation of the transect changes (see Figure 4.1). The viewer is looking to the north.

References

- Aagaard, K., J. H. Swift, and E. C. Carmack (1985). “Thermohaline circulation in the Arctic Mediterranean Seas”. In: *Journal of Geophysical Research: Oceans* 90.C3, pp. 4833–4846. DOI: [10.1029/JC090iC03p04833](https://doi.org/10.1029/JC090iC03p04833). URL: <https://agupubs.onlinelibrary.wiley.com/doi/abs/10.1029/JC090iC03p04833>.
- Adcroft, Alistair, Jean-Michel Campin, Chris Hill, and John Marshall (2004). “Implementation of an Atmosphere–Ocean General Circulation Model on the Expanded Spherical Cube”. In: *Monthly Weather Review* 132.12, pp. 2845–2863. DOI: [10.1175/MWR2823.1](https://doi.org/10.1175/MWR2823.1). URL: <https://doi.org/10.1175/MWR2823.1>.
- Almansi, M., T. W. N. Haine, R. Gelderloos, and R. S. Pickart (2020). “Evolution of Denmark Strait Overflow Cyclones and Their Relationship to Overflow Surges”. In: *Geophysical Research Letters* 47.4. ISSN: 0094-8276. DOI: [10.1029/2019gl086759](https://doi.org/10.1029/2019gl086759). URL: <https://agupubs.onlinelibrary.wiley.com/doi/abs/10.1029/2019GL086759>.
- Almansi, Mattia, Thomas W. N. Haine, Robert S. Pickart, Marcello G. Magaldi, Renske Gelderloos, and Dana Mastropole (2017). “High-Frequency Variability in the Circulation and Hydrography of the Denmark Strait Overflow from a High-Resolution Numerical Model”. In: *Journal of Physical Oceanography* 47, pp. 2999–3013. ISSN: 0022-3670. DOI: [10.1175/JPO-D-17-0129.1](https://doi.org/10.1175/JPO-D-17-0129.1). URL: <https://doi.org/10.1175/JPO-D-17-0129.1>.
- Almansi, Mattia, Renske Gelderloos, Thomas Haine, Atousa Saberi, and Ali Siddiqui (2019). “OceanSpy: A Python package to facilitate ocean model data analysis and visualization”. In: *Journal of Open Source Software* 4.39, p. 1506. DOI: [10.21105/joss.01506](https://doi.org/10.21105/joss.01506). URL: <http://joss.theoj.org/papers/10.21105/joss.01506>.
- Asthorsson, Olafur S., Gislaon Astthor, and Steingrímur Jonsson (2007). “Climate variability and the Icelandic marine ecosystem”. In: *Deep-Sea Research Part II: Topical Studies in Oceanography* 54.23, pp. 2456–2477. ISSN:

- 0967-0645. DOI: [10.1016/j.dsr2.2007.07.030](https://doi.org/10.1016/j.dsr2.2007.07.030). URL: <https://doi.org/10.1016/j.dsr2.2007.07.030>.
- Bakker, P., C. J. Van Meerbeeck, and H. Renssen (2012). "Sensitivity of the North Atlantic climate to Greenland ice sheet melting during the Last Interglacial". In: *Climate of the Past* 8.3, pp. 995–1009. DOI: [10.5194/cp-8-995-2012](https://doi.org/10.5194/cp-8-995-2012). URL: <https://www.clim-past.net/8/995/2012/>.
- Bamber, Jonathan, Michiel Van Den Broeke, Janneke Ettema, Jan Lenaerts, and Eric Rignot (2012). "Recent large increases in freshwater fluxes from Greenland into the North Atlantic". In: *Geophysical Research Letters* 39.19. DOI: [10.1029/2012GL052552](https://doi.org/10.1029/2012GL052552). URL: <https://agupubs.onlinelibrary.wiley.com/doi/abs/10.1029/2012GL052552>.
- Barnston, Anthony Gaston; and Robert E. Levezey (1987). "Classification, Seasonality and Persistence of Low-Frequency Atmospheric Circulation Patterns". In: *Monthly Weather Review* 115.6, pp. 1083–1126. DOI: [10.1175/1520-0493\(1987\)115%3C1083:CSAPOL%3E2.0.CO;2](https://doi.org/10.1175/1520-0493(1987)115%3C1083:CSAPOL%3E2.0.CO;2). URL: [https://doi.org/10.1175/1520-0493\(1987\)115%3C1083:CSAPOL%3E2.0.CO;2](https://doi.org/10.1175/1520-0493(1987)115%3C1083:CSAPOL%3E2.0.CO;2).
- Behrens, Erik, Kjetil Våge, Benjamin Harden, Arne Biastoch, and Claus W. Böning (2017). "Composition and variability of the Denmark Strait Overflow Water in a high-resolution numerical model hindcast simulation". In: *Journal of Geophysical Research: Oceans* 122.4, pp. 2830–2846. DOI: [10.1002/2016JC012158](https://doi.org/10.1002/2016JC012158). URL: <https://agupubs.onlinelibrary.wiley.com/doi/abs/10.1002/2016JC012158>.
- Bromwich, D. H., A. B. Wilson, L. Bai, Z. Liu, M. Barlage, C. F. Shih, S. Maldonado, K. M. Hines, S. H. Wang, J. Woollen, B. Kuo, H. C. Lin, T. K. Wee, M. C. Serreze, and J. E. Walsh (2018). "The arctic system reanalysis, version 2". In: *Bulletin of the American Meteorological Society* 99.4, pp. 805–828. DOI: [10.1175/BAMS-D-16-0215.1](https://doi.org/10.1175/BAMS-D-16-0215.1). URL: <https://doi.org/10.1175/BAMS-D-16-0215.1>.
- Bromwich, David H., Aaron B. Wilson, Le Sheng Bai, George W K Moore, and Peter Bauer (2016). "A comparison of the regional Arctic System Reanalysis and the global ERA-Interim Reanalysis for the Arctic". In: *Quarterly Journal of the Royal Meteorological Society* 142.695, pp. 644–658. DOI: [10.1002/qj.2527](https://doi.org/10.1002/qj.2527). URL: <https://rmets.onlinelibrary.wiley.com/doi/abs/10.1002/qj.2527>.
- Bruce, J. G. (1995). "Eddies southwest of the Denmark Strait". In: *Deep Sea Research Part I: Oceanographic Research Papers* 42.1, pp. 0967–0637. ISSN: 0967-0637. DOI: [https://doi.org/10.1016/0967-0637\(94\)00040-Y](https://doi.org/10.1016/0967-0637(94)00040-Y). URL: <http://www.sciencedirect.com/science/article/pii/096706379400040Y>.

- Buch, Erik, Svend-Aage Malmberg, and Stefan S. Kristmannsson (1996). "Arctic Ocean deep water masses in the western Iceland Sea". In: *Journal of Geophysical Research: Oceans* 101.C5, pp. 11965–11973. DOI: [10.1029/95JC03869](https://doi.org/10.1029/95JC03869). URL: <https://agupubs.onlinelibrary.wiley.com/doi/abs/10.1029/95JC03869>.
- Campin, Jean-Michel, Alistair Adcroft, Chris Hill, and John Marshall (2004). "Conservation of properties in a free-surface model". In: *Ocean Modelling* 6.3, pp. 221–244. ISSN: 1463-5003. DOI: [https://doi.org/10.1016/S1463-5003\(03\)00009-X](https://doi.org/10.1016/S1463-5003(03)00009-X). URL: <http://www.sciencedirect.com/science/article/pii/S146350030300009X>.
- Cenedese, Claudia, J. A. Whitehead, T. A. Ascarelli, and M. Ohiwa (2004). "A dense current flowing down a sloping bottom in a rotating fluid". In: *Journal of Physical Oceanography* 34.1, pp. 188–203. ISSN: 00223670. DOI: [10.1175/1520-0485\(2004\)034<0188:ADCFDA>2.0.CO;2](https://doi.org/10.1175/1520-0485(2004)034<0188:ADCFDA>2.0.CO;2). URL: [https://doi.org/10.1175/1520-0485\(2004\)034%3C0188:ADCFDA%3E2.0.CO;2](https://doi.org/10.1175/1520-0485(2004)034%3C0188:ADCFDA%3E2.0.CO;2).
- Chelton, Dudley B., Roland A. DeSzoeke, Michael G. Schlax, Karim El Naggar, and Nicolas Siwertz (1998). "Geographical Variability of the First Baroclinic Rossby Radius of Deformation". In: *Journal of Physical Oceanography* 28.3, pp. 433–460. DOI: [10.1175/1520-0485\(1998\)028<0433:gvotfb>2.0.co;2](https://doi.org/10.1175/1520-0485(1998)028<0433:gvotfb>2.0.co;2). URL: [https://doi.org/10.1175/1520-0485\(1998\)028%3C0433:GVOTFB%3E2.0.CO;2](https://doi.org/10.1175/1520-0485(1998)028%3C0433:GVOTFB%3E2.0.CO;2).
- Cooper, LHN (1955). "Deep water movements in the North Atlantic as a link between climatic changes around Iceland and biological productivity of the English Channel and Celtic Sea". In: *Journal of Marine Research* 14, pp. 347–362.
- Copernicus Climate Change Service (C3S) (2017). *RA5: Fifth generation of ECMWF atmospheric reanalyses of the global climate*. Copernicus Climate Change Service Climate Data Store (CDS). URL: <https://cds.climate.copernicus.eu/cdsapp#!/home>.
- Cummings, James A. and Ole Martin Smedstad (2013). "Variational Data Assimilation for the Global Ocean". In: *Data Assimilation for Atmospheric, Oceanic and Hydrologic Applications (Vol. II)*. Ed. by Seon Ki Park and Liang Xu. Berlin, Heidelberg: Springer Berlin Heidelberg, pp. 303–343. ISBN: 978-3-642-35088-7. DOI: [10.1007/978-3-642-35088-7_13](https://doi.org/10.1007/978-3-642-35088-7_13). URL: https://doi.org/10.1007/978-3-642-35088-7_13.
- Dask Development Team (2016). *Dask: Library for dynamic task scheduling*. URL: <https://dask.org>.

- Dee, D. P., S. M. Uppala, A. J. Simmons, P. Berrisford, P. Poli, S. Kobayashi, U. Andrae, M. A. Balmaseda, G. Balsamo, P. Bauer, P. Bechtold, A. C M Beljaars, L. van de Berg, J. Bidlot, N. Bormann, C. Delsol, R. Dragani, M. Fuentes, A. J. Geer, L. Haimberger, S. B. Healy, H. Hersbach, E. V. Hólm, L. Isaksen, P. Kållberg, M. Köhler, M. Matricardi, A. P. McNally, B. M. Monge-Sanz, J. J. Morcrette, B. K. Park, C. Peubey, P. de Rosnay, C. Tavolato, J. N. Thépaut, and F. Vitart (2011). "The ERA-Interim reanalysis: Configuration and performance of the data assimilation system". In: *Quarterly Journal of the Royal Meteorological Society* 137.656, pp. 553–597. ISSN: 00359009. DOI: 10.1002/qj.828. URL: <https://rmets.onlinelibrary.wiley.com/doi/abs/10.1002/qj.828>.
- Dickson, Robert and Juan Brown (1994). "The production of North Atlantic Deep Water : Sources , rates , and pathways la . Worthington ' s scheme conversion paths North Circled numbers are transport estimates in Sverdrups , where lb . The recasting of Worthington ' s scheme by McCartney and". In: *Journal of Geophysical Research* 99.C6, pp. 12319–12341. DOI: 10.1029/94JC00530. URL: <https://agupubs.onlinelibrary.wiley.com/doi/abs/10.1029/94JC00530>.
- Donlon, Craig J., Matthew Martin, John Stark, Jonah Roberts-Jones, Emma Fiedler, and Werenfrid Wimmer (2012). "The Operational Sea Surface Temperature and Sea Ice Analysis (OSTIA) system". In: *Remote Sensing of Environment* 116, pp. 140–158. ISSN: 00344257. DOI: <https://doi.org/10.1016/j.rse.2010.10.017>. URL: <http://www.sciencedirect.com/science/article/pii/S0034425711002197>.
- Eady, E. T. (1949). "Long Waves and Cyclone Waves". In: *Tellus* 1.3, pp. 33–52. ISSN: 0040-2826. DOI: 10.3402/tellusa.v1i3.8507. URL: <https://onlinelibrary.wiley.com/doi/abs/10.1111/j.2153-3490.1949.tb01265.x>.
- Eldevik, Tor, Jan Even Nilsen, Doroteaciro Iovino, K. Anders Olsson, Anne Britt Sandø, and Helge Drange (2009). "Observed sources and variability of Nordic seas overflow". In: *Nature Geoscience* 2.6, pp. 406–410. ISSN: 17520894. DOI: 10.1038/ngeo518.
- Gelderloos, Renske, Thomas W. N. Haine, Inga M. Koszalka, and Marcello G. Magaldi (2017). "Seasonal Variability in Warm-Water Inflow toward Kangerdlugssuaq Fjord". In: *Journal of Physical Oceanography* 47.7, pp. 1685–1699. DOI: 10.1175/JPO-D-16-0202.1. URL: <https://doi.org/10.1175/JPO-D-16-0202.1>.

- Girton, James B. and Thomas B. Sanford (2003). "Descent and Modification of the Overflow Plume in the Denmark Strait". In: *Journal of Physical Oceanography* 33.7, pp. 1351–1364. DOI: [10.1175/1520-0485\(2003\)033<1351:DAMOTO>2.0.CO;2](https://doi.org/10.1175/1520-0485(2003)033<1351:DAMOTO>2.0.CO;2); 2. URL: [https://doi.org/10.1175/1520-0485\(2003\)033%3C1351:DAMOTO%3E2.0.CO;2](https://doi.org/10.1175/1520-0485(2003)033%3C1351:DAMOTO%3E2.0.CO;2).
- Girton, James B., Thomas B. Sanford, and Rolf H. Käse (2001). "Synoptic sections of the Denmark Strait Overflow". In: *Geophysical Research Letters* 28.8, pp. 1619–1622. DOI: [10.1029/2000GL011970](https://doi.org/10.1029/2000GL011970). URL: <https://agupubs.onlinelibrary.wiley.com/doi/abs/10.1029/2000GL011970>.
- Haine, T. W. N. (2010). "High-frequency fluctuations in Denmark strait transport". In: *Geophysical Research Letters* 37.14. DOI: [10.1029/2010GL043272](https://doi.org/10.1029/2010GL043272). URL: <https://agupubs.onlinelibrary.wiley.com/doi/abs/10.1029/2010GL043272>.
- Haine, T. W. N., S. Zhang, G. W. K. Moore, and I. A. Renfrew (2009). "On the impact of high-resolution, high-frequency meteorological forcing on Denmark Strait ocean circulation". In: *Quarterly Journal of the Royal Meteorological Society* 135.645, pp. 2067–2085. DOI: [10.1002/qj.505](https://doi.org/10.1002/qj.505). URL: <https://rmets.onlinelibrary.wiley.com/doi/abs/10.1002/qj.505>.
- Haine, Thomas W.N., Beth Curry, Rüdiger Gerdes, Edmond Hansen, Michael Karcher, Craig Lee, Bert Rudels, Gunnar Spreen, Laura de Steur, Kial D. Stewart, and Rebecca Woodgate (2015). "Arctic freshwater export: Status, mechanisms, and prospects". In: *Global and Planetary Change* 125, pp. 13–35. ISSN: 0921-8181. DOI: <https://doi.org/10.1016/j.gloplacha.2014.11.013>. URL: <http://www.sciencedirect.com/science/article/pii/S0921818114003129>.
- Hamilton, Lawrence C., Steingrímur Jónsson, Helga Ögmundardóttir, and Igor M. Belkin (2004). "Sea changes ashore: The ocean and iceland's herring capital". In: *Arctic* 57.4, pp. 325–335. ISSN: 00040843. DOI: [10.14430/arctic511](https://doi.org/10.14430/arctic511).
- Hansen, Bogi, Karin Margretha Husgaro, Hjálmar Hátún, and Svein Østerhus (2016). "A stable Faroe Bank Channel overflow 1995-2015". In: *Ocean Science* 12.6, pp. 1205–1220. DOI: [10.5194/os-12-1205-2016](https://doi.org/10.5194/os-12-1205-2016). URL: <https://www.ocean-sci.net/12/1205/2016/>.
- Harden, B.E., R.S. Pickart, Héðinn Valdimarsson, Kjetil Våge, Laura de Steur, Clark Richards, Frank Bahr, Dan Torres, Eli Børve, Steingrímur Jónsson, Andreas Macrander, Svein Østerhus, Lisbeth Håvik, and Tore Hattermann (2016). "Upstream sources of the Denmark Strait Overflow: Observations from a high-resolution mooring array". In: *Deep-Sea Research Part I: Oceanographic Research Papers* 112, pp. 94–112. ISSN: 0967-0637. DOI: <https://doi.org/10.1016/j.dsrp.2016.05.001>.

- org/10.1016/j.dsr.2016.02.007. URL: <http://www.sciencedirect.com/science/article/pii/S0967063715301266>.
- Harvey, J. G. (1961). "Overflow of Cold Deep Water across Iceland–Greenland Ridge". In: *Nature* 189.4768, pp. 911–913. DOI: 10.1038/189911a0. URL: <https://doi.org/10.1038/189911a0>.
- Håvik, L., K. Våge, R. S. Pickart, B. Harden, W. J. Von Appen, S. Jónsson, and S. Østerhus (2017). "Structure and variability of the shelfbreak East Greenland current North of Denmark Strait". In: *Journal of Physical Oceanography* 47.10, pp. 2631–2646. ISSN: 15200485. DOI: 10.1175/JPO-D-17-0062.1. URL: <https://doi.org/10.1175/JPO-D-17-0062.1>.
- Håvik, Lisbeth, Mattia Almansi, Kjetil Våge, and Thomas W. N. Haine (2019). "Atlantic-origin overflow Water in the East Greenland Current". In: *Journal of Physical Oceanography* 49.9, pp. 2255–2269. DOI: 10.1175/jpo-d-18-0216.1. URL: <https://doi.org/10.1175/JPO-D-18-0216.1>.
- Helfrich, Karl R. and Lawrence J. Pratt (2003). "Rotating Hydraulics and Upstream Basin Circulation". In: *Journal of Physical Oceanography* 33.8, pp. 1651–1663. DOI: 10.1175/1520-0485(2003)033<1651:RHAUBC>2.0.CO;2. URL: <https://journals.ametsoc.org/doi/abs/10.1175/1520->
- Hoyer, Stephan and Joseph J. Hamman (2017). "xarray: N-D labeled Arrays and Datasets in Python". In: *Journal of Open Research Software* 5, pp. 1–6. DOI: 10.5334/jors.148.
- Isern-Fontanet, Jordi, Emilio García-Ladona, and Jordi Font (2006). "Vortices of the Mediterranean Sea: An Altimetric Perspective". In: *Journal of Physical Oceanography* 36.1, pp. 87–103. ISSN: 0022-. DOI: 10.1175/jpo2826.1. URL: <https://doi.org/10.1175/JPO2826.1>.
- Jackett, David R. and Trevor J. McDougall (1995). "Minimal Adjustment of Hydrographic Profiles to Achieve Static Stability". In: *Journal of Atmospheric and Oceanic Technology* 12.2, pp. 381–389. DOI: 10.1175/1520-0426(1995)012<0381:MAOHPT>2.0.CO;2. URL: [https://doi.org/10.1175/1520-0426\(1995\)012%3C0381:MAOHPT%3E2.0.CO;2](https://doi.org/10.1175/1520-0426(1995)012%3C0381:MAOHPT%3E2.0.CO;2).
- Jakobsson, Martin, Larry Mayer, Bernard Coakley, Julian A. Dowdeswell, Steve Forbes, Boris Fridman, Hanne Hodnesdal, Riko Noormets, Richard Pedersen, Michele Rebesco, Hans Werner Schenke, Yulia Zarayskaya, Daniela Accettella, Andrew Armstrong, Robert M. Anderson, Paul Bienhoff, Angelo Camerlenghi, Ian Church, Margo Edwards, James V. Gardner, John K. Hall, Benjamin Hell, Ole Hestvik, Yngve Kristoffersen, Christian Marcussen, Rezwan Mohammad, David Mosher, Son V. Nghiem, Maria

- Teresa Pedrosa, Paola G. Travaglini, and Pauline Weatherall (2012). "The International Bathymetric Chart of the Arctic Ocean (IBCAO) Version 3.0". In: *Geophysical Research Letters* 39.12. DOI: 10.1029/2012GL052219. URL: <https://agupubs.onlinelibrary.wiley.com/doi/abs/10.1029/2012GL052219>.
- Jochumsen, Kerstin, Detlef Quadfasel, Heðinn Valdimarsson, and Steingrímur Jónsson (2012). "Variability of the Denmark Strait overflow: Moored time series from 1996-2011". In: *Journal of Geophysical Research: Oceans* 117.C12. DOI: 10.1029/2012JC008244. URL: <https://agupubs.onlinelibrary.wiley.com/doi/abs/10.1029/2012JC008244>.
- Jochumsen, Kerstin, Martin Moritz, Nuno Nunes, Detlef Quadfasel, Karin M.H. Larsen, Bogi Hansen, Hedinn Valdimarsson, and Steingrímur Jónsson (2017). "Revised transport estimates of the Denmark Strait overflow". In: *Journal of Geophysical Research: Oceans* 122.4, pp. 3434–3450. DOI: 10.1002/2017JC012803. URL: <https://agupubs.onlinelibrary.wiley.com/doi/abs/10.1002/2017JC012803>.
- Jónsson, Steingrímur and Hedinn Valdimarsson (2004). "A new path for the Denmark Strait overflow water from the Iceland Sea to Denmark Strait". In: *Geophysical Research Letters* 31.3. DOI: 10.1029/2003GL019214. URL: <https://agupubs.onlinelibrary.wiley.com/doi/abs/10.1029/2003GL019214>.
- Jungclauss, Johann H., Janko Hauser, Rolf H. Käse, Johann H. Jungclauss, Janko Hauser, and Rolf H. Käse (2001). "Cyclogenesis in the Denmark Strait Overflow Plume". In: *Journal of Physical Oceanography* 31.11, pp. 3214–3229. DOI: 10.1175/1520-0485(2001)031<3214:CITDSO>2.0.CO;2. URL: [https://doi.org/10.1175/1520-0485\(2001\)031%3C3214:CITDSO%3E2.0.CO;2](https://doi.org/10.1175/1520-0485(2001)031%3C3214:CITDSO%3E2.0.CO;2).
- Käse, R. H., James B. Girton, and Thomas B. Sanford (2003). "Structure and variability of the Denmark Strait Overflow: Model and observations". In: *Journal of Geophysical Research* 108.C6. DOI: 10.1029/2002JC001548. URL: <https://agupubs.onlinelibrary.wiley.com/doi/abs/10.1029/2002JC001548>.
- Käse, R.H. and A. Oschlies (2000). "Flow through Denmark Strait". In: *Journal of Geophysical Research: Oceans* 105.C12, pp. 28527–28546. ISSN: 21699291. DOI: 10.1029/2000JC900111.
- Klinger, Barry A. and Thomas W. N. Haine (2019). *Ocean Circulation in Three Dimensions*. Cambridge: Cambridge University Press. DOI: 10.1017/9781139015721.
- Klocker, Andreas and Ryan Abernathy (2014). "Global Patterns of Mesoscale Eddy Properties and Diffusivities". In: *Journal of Physical Oceanography* 44.3, pp. 1030–1046. DOI: 10.1175/jpo-d-13-0159.1. URL: <https://doi.org/10.1175/JPO-D-13-0159.1>.

- Köhl, Armin, Rolf H. Käse, Detlef Stammer, and Nuno Serra (2007). "Causes of Changes in the Denmark Strait Overflow". In: *Journal of Physical Oceanography* 37.6, pp. 1678–1696. DOI: 10.1175/JPO3080.1. URL: <https://doi.org/10.1175/JPO3080.1>.
- Kösters, F., R. H. Käse, A. Schmittner, and P. Herrmann (2005). "The effect of Denmark Strait overflow on the Atlantic Meridional Overturning Circulation". In: *Geophysical Research Letters* 32.4. DOI: 10.1029/2004GL022112. URL: <https://agupubs.onlinelibrary.wiley.com/doi/abs/10.1029/2004GL022112>.
- Koszalka, Inga M., Thomas W. N. Haine, and Marcello G. Magaldi (2013). "Fates and Travel Times of Denmark Strait Overflow Water in the Irminger Basin". In: *Journal of Physical Oceanography* 43.12, pp. 2611–2628. DOI: 10.1175/JPO-D-13-023.1. URL: <https://doi.org/10.1175/JPO-D-13-023.1>.
- Koszalka, Inga M., Thomas W. N. Haine, and Marcello G. Magaldi (2017). "Mesoscale mixing of the Denmark Strait Overflow in the Irminger Basin". In: *Ocean Modelling* 112, pp. 90–98. ISSN: 1463-5003. DOI: 10.1016/j.ocemod.2017.03.001. URL: <http://www.sciencedirect.com/science/article/pii/S1463500317300264>.
- Krauss, W. (1996). "A note on overflow eddies". In: *Deep-Sea Research Part I: Oceanographic Research Papers* 43.10, pp. 1661–1667. ISSN: 0967-0637. DOI: [https://doi.org/10.1016/S0967-0637\(96\)00073-8](https://doi.org/10.1016/S0967-0637(96)00073-8). URL: <http://www.sciencedirect.com/science/article/pii/S0967063796000738>.
- Krauss, Wolfgang and Rolf H. Käse (1998). "Eddy formation in the Denmark Strait overflow". In: *Journal of Geophysical Research: Oceans* 103.C8, pp. 15525–15538. DOI: 10.1029/98jc00785. URL: <https://agupubs.onlinelibrary.wiley.com/doi/abs/10.1029/98jc00785>.
- Kuhlbrot, T., A. Griesel, M. Montoya, A. Levermann, M. Hofmann, and S. Rahmstorf (2007). "On the driving processes of the Atlantic meridional overturning circulation". In: *Reviews of Geophysics* 45.2. DOI: 10.1029/2004RG000166. URL: <https://agupubs.onlinelibrary.wiley.com/doi/abs/10.1029/2004RG000166>.
- Large, W. G., J. C. McWilliams, and S. C. Doney (1994). "Oceanic vertical mixing: A review and a model with a nonlocal boundary layer parameterization". In: *Reviews of Geophysics* 32.4, pp. 363–403. DOI: 10.1029/94RG01872. URL: <https://agupubs.onlinelibrary.wiley.com/doi/abs/10.1029/94RG01872>.

- Legg, Sonya, Robert W. Hallberg, and James B. Girton (2006). "Comparison of entrainment in overflows simulated by z-coordinate, isopycnal and non-hydrostatic models". In: *Ocean Modelling* 11.1-2, pp. 69–97. ISSN: 1463-5003. DOI: 10.1016/j.ocemod.2004.11.006. URL: <http://www.sciencedirect.com/science/article/pii/S1463500304001064>.
- Legg, Sonya, Bruce Briegleb, Yeon Chang, Eric P. Chassignet, Gokhan Danabasoglu, Tal Ezer, Arnold L. Gordon, Stephen Griffies, Robert Hallberg, Laura Jackson, William Large, Tamay M. Özgükmen, Hartmut Peters, Jim Price, Ulrike Riemenschneider, Wanli Wu, Xiaobiao Xu, and Jiayan Yang (2009). "Improving oceanic overflow representation in climate models: The Gravity Current Entrainment Climate Process Team". In: *Bulletin of the American Meteorological Society* 90.5, pp. 657–670. DOI: 10.1175/2008BAMS2667.1. URL: <https://doi.org/10.1175/2008BAMS2667.1>.
- Lian, Zhan, Baonan Sun, Zexun Wei, Yonggang Wang, and Xinyi Wang (2019). "Comparison of eight detection algorithms for the quantification and characterization of mesoscale eddies in the South China Sea". In: *Journal of Atmospheric and Oceanic Technology* 36.7, pp. 1361–1380. DOI: 10.1175/jtech-d-18-0201.1. URL: <https://doi.org/10.1175/JTECH-D-18-0201.1>.
- Livingston, Hugh D., James H. Swift, and H. Gote Ostlund (1985). "Artificial radionuclide tracer supply to the Denmark Strait overflow between 1972 and 1981". In: *Journal of Geophysical Research* 90.C4, pp. 6971–6982. DOI: 10.1029/jc090ic04p06971. URL: <https://agupubs.onlinelibrary.wiley.com/doi/abs/10.1029/JC090iC04p06971>.
- Logemann, K., J. Ólafsson, Á. Snorrason, H. Valdimarsson, and G. Marteinsdóttir (2013). "The circulation of Icelandic waters - A modelling study". In: *Ocean Science* 9.5, pp. 931–955. DOI: 10.5194/os-9-931-2013. URL: <https://www.ocean-sci.net/9/931/2013/>.
- Losch, Martin, Dimitris Menemenlis, Jean Michel Campin, Patick Heimbach, and Chris Hill (2010). "On the formulation of sea-ice models. Part 1: Effects of different solver implementations and parameterizations". In: *Ocean Modelling* 33.1, pp. 129–144. ISSN: 1463-5003. DOI: 10.1016/j.ocemod.2009.12.008. URL: <http://www.sciencedirect.com/science/article/pii/S1463500309002418>.
- Macrander, A., U. Send, H. Valdimarsson, S. Jónsson, and R. H. Käse (2005). "Interannual changes in the overflow from the Nordic Seas into the Atlantic Ocean through Denmark Strait". In: *Geophysical Research Letters* 32.6. DOI: 10.1029/2004GL021463. URL: <https://agupubs.onlinelibrary.wiley.com/doi/abs/10.1029/2004GL021463>.

- Macrander, Andreas, Rolf H. Käse, Uwe Send, Héðinn Valdimarsson, and Steingrímur Jónsson (2007). "Spatial and temporal structure of the Denmark Strait Overflow revealed by acoustic observations". In: *Ocean Dynamics* 57.2, pp. 75–89. DOI: 10.1007/s10236-007-0101-x. URL: <https://doi.org/10.1007/s10236-007-0101-x>.
- Magaldi, M. G., T. W. N. Haine, and R. S. Pickart (2011). "On the Nature and Variability of the East Greenland Spill Jet: A Case Study in Summer 2003". In: *Journal of Physical Oceanography* 41.12, pp. 2307–2327. DOI: 10.1175/JPO-D-10-05004.1. URL: <https://doi.org/10.1175/JPO-D-10-05004.1>.
- Marshall, John, Alistair Adcroft, Chris Hill, Lev Perelman, and Curt Heisey (1997). "A finite-volume, incompressible Navier Stokes model for studies of the ocean on parallel computers". In: *Journal of Geophysical Research: Oceans* 102.C3, pp. 5753–5766. DOI: 10.1029/96JC02775. URL: <https://agupubs.onlinelibrary.wiley.com/doi/abs/10.1029/96JC02775>.
- Martínez-Moreno, Josué, Andrew McC. Hogg, Andrew E. Kiss, Navid C. Constantinou, and Adele K. Morrison (2019). "Kinetic energy of eddy-like features from sea surface altimetry". In: *Journal of Advances in Modeling Earth Systems* 11.10, pp. 1–19. DOI: 10.1029/2019MS001769. URL: <https://agupubs.onlinelibrary.wiley.com/doi/abs/10.1029/2019MS001769>.
- Mastropole, Dana, Robert S. Pickart, Héðinn Valdimarsson, Kjetil Våge, Kerstin Jochumsen, and James Girton (2017). "On the hydrography of Denmark Strait". In: *Journal of Geophysical Research: Oceans* 122.1, pp. 306–321. DOI: 10.1002/2016JC012007. URL: <https://agupubs.onlinelibrary.wiley.com/doi/abs/10.1002/2016JC012007>.
- Mauritzen, Cecilie (1996). "Production of dense overflow waters feeding the North Atlantic across the Greenland-Scotland Ridge. Part 1: Evidence for a revised circulation scheme". In: *Deep-Sea Research Part I: Oceanographic Research Papers* 43.6, pp. 769–806. DOI: 10.1016/0967-0637(96)00037-4. URL: <http://www.sciencedirect.com/science/article/pii/0967063796000374>.
- Medvedev, Dmitry, Gerard Lemson, and Mike Rippin (2016). "SciServer Compute: Bringing Analysis Close to the Data". In: *Proceedings of the 28th International Conference on Scientific and Statistical Database Management*. Budapest, Hungary: ACM, 27:1–27:4. ISBN: 978-1-4503-4215-5. DOI: 10.1145/2949689.2949700. URL: <http://doi.acm.org/10.1145/2949689.2949700>.
- Nikolopoulos, Anna, Karin Borenäs, Riikka Hietala, and Peter Lundberg (2003). "Hydraulic estimates of Denmark Strait overflow". In: *Journal of*

- Geophysical Research* 108.C3. DOI: 10.1029/2001JC001283. URL: <http://www.agu.org/pubs/crossref/2003/2001JC001283.shtml>.
- Noël, Brice, Willem Jan van de Berg, Horst Machguth, Stef Lhermitte, Ian Howat, Xavier Fettweis, and Michiel R. van den Broeke (2016). “A daily, 1 km resolution data set of downscaled Greenland ice sheet surface mass balance (1958-2015)”. In: *The Cryosphere* 10.5, pp. 2361–2377. DOI: 10.5194/tc-10-2361-2016. URL: <https://www.the-cryosphere.net/10/2361/2016/>.
- North, Ryan P, Kerstin Jochumsen, and Martin Moritz (2018). “Entrainment and energy transfer variability along the descending path of the Denmark Strait overflow plume”. In: *Journal of Geophysical Research: Oceans* 123.4, pp. 2795–2807. DOI: 10.1002/2018JC013821. URL: <https://agupubs.onlinelibrary.wiley.com/doi/abs/10.1002/2018JC013821>.
- Okubo, Akira (1970). “Horizontal dispersion of floatable particles in the vicinity of velocity singularities such as convergences”. In: *Deep-Sea Research and Oceanographic Abstracts* 17.3, pp. 445–454. ISSN: 0011-7471. DOI: [https://doi.org/10.1016/0011-7471\(70\)90059-8](https://doi.org/10.1016/0011-7471(70)90059-8). URL: <http://www.sciencedirect.com/science/article/pii/0011747170900598>.
- Østerhus, Svein, Rebecca Woodgate, Héðinn Valdimarsson, Bill Turrell, Laura De Steur, Detlef Quadfasel, Steffen M. Olsen, Martin Moritz, Craig M. Lee, Karin Margretha H. Larsen, Steingrímur Jónsson, Clare Johnson, Kerstin Jochumsen, Bogi Hansen, Beth Curry, Stuart Cunningham, and Barbara Berx (2019). “Arctic Mediterranean exchanges: A consistent volume budget and trends in transports from two decades of observations”. In: *Ocean Science* 15.2, pp. 379–399. DOI: 10.5194/os-15-379-2019. URL: <https://www.ocean-sci.net/15/379/2019/>.
- Pedlosky, J. (1979). *Geophysical fluid dynamics*. Springer-Verlag. ISBN: 3540903682. DOI: 10.4171/owr/2017/23.
- Pickart, Robert S, Daniel J Torres, and Paula S Fratantoni (2005). “The East Greenland Spill Jet”. In: *Journal of Physical Oceanography* 35.6, pp. 1037–1053. DOI: 10.1175/JP02734.1. URL: <https://doi.org/10.1175/JP02734.1>.
- Renfrew, I. A., R. S. Pickart, K. Våge, G. W. K. Moore, T. J. Bracegirdle, A. D. Elvidge, E. Jeansson, T. Lachlan-Cope, L.T. McRaven, L. Papritz, J. Reuder, H. Sodemann, A. Terpstra, S. Waterman, H. Valdimarsson, A. Weiss, M. Almansi, F. Bahr, A. Brakstad, C. Barrell, J. K. Brooke, B.J. Brooks, I. M. Brooks, M. E. Brooks, E. M. Bruvik, C. Duscha, I. Fer, H. M. Golid, M. Hallerstig, I. Hessevik, J. Huang, L. Houghton, S. Jónsson, M. Jonassen, K. Jackson, K. Kvalsund, E. W. Kolstad, K. Konstali, J. Kristiansen, R. Ladkin,

- P. Lin, A. Macrander, A. Mitchell, H. Olafsson, A. Pacini, C. Payne, B. Palmason, M. D. Pérez-Hernández, A. K. Peterson, G. N. Petersen, M. N. Pisareva, J. O. Pope, A. Seidl, S. Semper, D. Sergeev, S. Skjelsvik, H. Søiland, D. Smith, M. A. Spall, T. Spengler, A. Touzeau, G. Tupper, Y. Weng, K. D. Williams, X. Yang, and S. Zhou (2019). "The Iceland Greenland Seas Project". In: *Bulletin of the American Meteorological Society* February. ISSN: 0003-0007. DOI: [10.1175/bams-d-18-0217.1](https://doi.org/10.1175/bams-d-18-0217.1).
- Reszka, MK K, G E Swaters, and Bruce R. Sutherland (2002). "Instability of abyssal currents in a continuously stratified ocean with bottom topography". In: *Journal of Physical Oceanography* 32.12, pp. 3528–3550. DOI: [10.1175/1520-0485\(2002\)032%3C3528:IOACIA%3E2.0.CO;2](https://doi.org/10.1175/1520-0485(2002)032%3C3528:IOACIA%3E2.0.CO;2). URL: [https://doi.org/10.1175/1520-0485\(2002\)032%3C3528:IOACIA%3E2.0.CO;2](https://doi.org/10.1175/1520-0485(2002)032%3C3528:IOACIA%3E2.0.CO;2).
- Ross, CK (1984). "Temperature-salinity characteristics of the "overflow" water in Denmark Strait during "OVERFLOW'73"". In: *Rapp. PV Reun. Cons. Int. Explor. Mer* 185, pp. 111–119.
- Rudels, Bert, Patrick Eriksson, Hannu Grönvall, Riikka Hietala, and Jouko Launiainen (1999). "Hydrographic observations in Denmark Strait in fall 1997, and their implications for the entrainment into the overflow plume". In: *Geophysical Research Letters* 26.9, pp. 1325–1328. DOI: [10.1029/1999GL900212](https://doi.org/10.1029/1999GL900212). URL: <https://agupubs.onlinelibrary.wiley.com/doi/abs/10.1029/1999GL900212>.
- Rudels, Bert, Eberhard Fahrback, Jens Meincke, Gereon Budéus, and Patrick Eriksson (2002). "The East Greenland Current and its contribution to the Denmark Strait overflow". In: *ICES Journal of Marine Science* 59.6, pp. 1133–1154. DOI: [10.1006/jmsc.2002.1284](https://doi.org/10.1006/jmsc.2002.1284). URL: <https://doi.org/10.1006/jmsc.2002.1284>.
- Rudels, Bert, Göran Björk, Johan Nilsson, Peter Winsor, Iréne Lake, and Christian Nohr (2005). "The interaction between waters from the Arctic Ocean and the Nordic Seas north of Fram Strait and along the East Greenland Current: Results from the Arctic Ocean-02 Oden expedition". In: *Journal of Marine Systems* 55.1-2, pp. 1–30. DOI: [10.1016/j.jmarsys.2004.06.008](https://doi.org/10.1016/j.jmarsys.2004.06.008). URL: <http://www.sciencedirect.com/science/article/pii/S0924796304002015>.
- Saberi, Atousa, Thomas W. N. Haine, Renske Gelderloos, Femke de Jong, Heather Furey, and Amy Bower (2020). "Lagrangian Perspective on the Origins of Denmark Strait Overflow". In: *Journal of Physical Oceanography*.
- Saenko, Oleg A. (2009). "Sensitivity of the subpolar Atlantic climate to local winds". In: *Geophysical Research Letters* 36.3. ISSN: 00948276. DOI: [10.1029/](https://doi.org/10.1029/)

- 2008GL036308. URL: <https://agupubs.onlinelibrary.wiley.com/doi/abs/10.1029/2008GL036308>.
- Sakov, P., F. Counillon, L. Bertino, K. A. Lister, P. R. Oke, and A. Korabely (2012). "TOPAZ4: An ocean-sea ice data assimilation system for the North Atlantic and Arctic". In: *Ocean Science* 8.4, pp. 633–656. DOI: 10.5194/os-8-633-2012. URL: <https://www.ocean-sci.net/8/633/2012/>.
- Semper, Stefanie, Kjetil Våge, Robert S. Pickart, Héðinn Valdimarsson, Daniel J. Torres, and Steingrímur Jónsson (2019). "The emergence of the North Icelandic Jet and its evolution from northeast Iceland to Denmark Strait". In: *Journal of Physical Oceanography* 49.10, pp. 2499–2521. DOI: 10.1175/jpo-d-19-0088.1. URL: <https://doi.org/10.1175/JPO-D-19-0088.1>.
- Shapiro, G. I., J. M. Huthnance, and V. V. Ivanov (2003). "Dense water cascading off the continental shelf". In: *Journal of Geophysical Research: Oceans* 108.C12. DOI: 10.1029/2002jc001610. URL: <https://agupubs.onlinelibrary.wiley.com/doi/abs/10.1029/2002JC001610>.
- Smith, Walter H. F. and David T. Sandwell (1997). "Global Sea Floor Topography from Satellite Altimetry and Ship Depth Soundings". In: *Science* 277.5334, pp. 1956–1962. ISSN: 0036-8075. DOI: 10.1126/science.277.5334.1956. URL: <https://science.sciencemag.org/content/277/5334/1956>.
- Souza, J. M.A.C., C. De Boyer Montégut, and P. Y. Le Traon (2011). "Comparison between three implementations of automatic identification algorithms for the quantification and characterization of mesoscale eddies in the South Atlantic Ocean". In: *Ocean Science* 7.3, pp. 317–334. DOI: 10.5194/os-7-317-2011. URL: <https://www.ocean-sci.net/7/317/2011/>.
- Spall, Michael a. and James F. Price (1998). "Mesoscale Variability in Denmark Strait: The PV Outflow Hypothesis". In: *Journal of Physical Oceanography* 28.8, pp. 1598–1623. DOI: 10.1175/1520-0485(1998)028<1598:MVIDST>2.0.CO;2. URL: [https://doi.org/10.1175/1520-0485\(1998\)028%3C1598:MVIDST%3E2.0.CO;2](https://doi.org/10.1175/1520-0485(1998)028%3C1598:MVIDST%3E2.0.CO;2).
- Spall, Michael A., Robert S. Pickart, Peigen Lin, Wilken-Jon von Appen, Dana Mastropole, H. Valdimarsson, Thomas W. N. Haine, and Mattia Almansi (2019). "Frontogenesis and variability in Denmark Strait and its influence on overflow water". In: *Journal of Physical Oceanography* 49.7, pp. 1889–1904. DOI: 10.1175/jpo-d-19-0053.1. URL: <https://doi.org/10.1175/JPO-D-19-0053.1>.
- Srokosz, M. a. and H. L. Bryden (2015). "Observing the Atlantic Meridional Overturning Circulation yields a decade of inevitable surprises". In: *Science* 348.6241. ISSN: 0036-8075. DOI: 10.1126/science.1255575. URL:

http://www.sciencemag.org.libezproxy.open.ac.uk/content/348/6241/1255575.full%5Cnhttps://twitter.com/icey_mark/status/611787119204433920.

- Strass, Volker H., Eberhard Fahrback, Ursula Schauer, and Lutz Sellmann (1993). "Formation of Denmark Strait overflow water by mixing in the East Greenland Current". In: *Journal of Geophysical Research: Oceans* 98.C4, pp. 6907–6919. DOI: 10.1029/92JC02732. URL: <https://agupubs.onlinelibrary.wiley.com/doi/abs/10.1029/92JC02732>.
- Sutherland, David A., Fiammetta Straneo, Garry B. Stenson, Fraser J M Davidson, Mike O. Hammill, and Aqqalu Rosing-Asvid (2013). "Atlantic water variability on the SE Greenland continental shelf and its relationship to SST and bathymetry". In: *Journal of Geophysical Research: Oceans* 118.2, pp. 847–855. DOI: 10.1029/2012JC008354. URL: <https://agupubs.onlinelibrary.wiley.com/doi/abs/10.1029/2012JC008354>.
- Swift, J. H. (1984). "A Recent θ -S Shift in the Deep Water of the Northern North Atlantic". In: *Climate Processes and Climate Sensitivity* 29, pp. 39–47. DOI: 10.1029/gm029p0039. URL: <https://agupubs.onlinelibrary.wiley.com/doi/abs/10.1029/GM029p0039>.
- Swift, James H., Knut Aagaard, and Svend Aage Malmberg (1980). "The contribution of the Denmark strait overflow to the deep North Atlantic". In: *Deep Sea Research Part A, Oceanographic Research Papers* 27.1, pp. 29–42. ISSN: 0198-0149. DOI: [https://doi.org/10.1016/0198-0149\(80\)90070-9](https://doi.org/10.1016/0198-0149(80)90070-9). URL: <http://www.sciencedirect.com/science/article/pii/0198014980900709>.
- "The GIUK Gap's strategic significance" (2019). In: *Strategic Comments* 25.8, pp. i–iii. ISSN: 13567888. DOI: 10.1080/13567888.2019.1684626. URL: <https://doi.org/10.1080/13567888.2019.1684626>.
- Våge, Kjetil, Robert S. Pickart, Michael A. Spall, Héðinn Valdimarsson, Steingrímur Jónsson, Daniel J. Torres, Svein Østerhus, and Tor Eldevik (2011). "Significant role of the North Icelandic Jet in the formation of Denmark Strait overflow water". In: *Nature Geoscience* 4.10, pp. 723–727. ISSN: 1752-0894. DOI: 10.1038/ngeo1234. URL: <https://www.nature.com/articles/ngeo1234.pdf>.
- Våge, Kjetil, Robert S. Pickart, Michael A. Spall, G. W K Moore, Héethinn Valdimarsson, Daniel J. Torres, Svetlana Y. Erofeeva, and Jan Even Ø Nilsen (2013). "Revised circulation scheme north of the Denmark Strait". In: *Deep-Sea Research Part I: Oceanographic Research Papers* 79, pp. 20–39.

- DOI: <https://doi.org/10.1016/j.dsr.2013.05.007>. URL: <http://www.sciencedirect.com/science/article/pii/S0967063713001040>.
- Våge, Kjetil, G. W.K. Moore, Steingrímur Jónsson, and Hédinn Valdimarsson (2015). "Water mass transformation in the iceland sea". In: *Deep-Sea Research Part I: Oceanographic Research Papers* 101, pp. 98–109. ISSN: 09670637. DOI: 10.1016/j.dsr.2015.04.001. URL: <http://www.sciencedirect.com/science/article/pii/S0967063715000680>.
- Våge, Kjetil, Lukas Papritz, Lisbeth Håvik, Michael A. Spall, and G. W.K. Moore (2018). "Ocean convection linked to the recent ice edge retreat along east Greenland". In: *Nature Communications* 9.1. ISSN: 20411723. DOI: 10.1038/s41467-018-03468-6. URL: <http://dx.doi.org/10.1038/s41467-018-03468-6>.
- Vallis, Geoffrey K. (2017). *Atmospheric and oceanic fluid dynamics: Fundamentals and large-scale circulation, second edition*. 2nd ed. Cambridge: Cambridge University Press. ISBN: 9781107588417. DOI: 10.1017/9781107588417.
- Voet, G and D Quadfasel (2010). "Entrainment in the Denmark Strait overflow plume by meso-scale eddies". In: *Ocean Science* 6.1, pp. 301–310. DOI: 10.5194/osd-6-2625-2009. URL: www.ocean-sci.net/6/301/2010/.
- Von Appen, Wilken-Jon (2013). "Moored observations of shelfbreak processes at the inflow to and outflow from the Arctic Ocean". PhD thesis. MASSACHUSETTS INSTITUTE OF TECHNOLOGY and WOODS HOLE OCEANOGRAPHIC INSTITUTION. DOI: 10.1575/1912/5822. URL: <https://hdl.handle.net/1912/5822>.
- Von Appen, Wilken-Jon, Inga M. Kozalka, Robert S. Pickart, Thomas W. N. Haine, Dana Mastropole, Marcello G. Magaldi, Hédinn Valdimarsson, James Girton, Kerstin Jochumsen, and Gerd Krahnemann (2014a). "The East Greenland Spill Jet as an important component of the Atlantic Meridional Overturning Circulation". In: *Deep Sea Research Part I: Oceanographic Research Papers* 92, pp. 75–84. ISSN: 0967-0637. DOI: 10.1016/j.dsr.2014.06.002. URL: <http://www.sciencedirect.com/science/article/pii/S0967063714001022>.
- Von Appen, Wilken Jon, Robert S. Pickart, Kenneth H. Brink, and Thomas W N Haine (2014b). "Water column structure and statistics of denmark strait overflow water cyclones". In: *Deep-Sea Research Part I: Oceanographic Research Papers* 84, pp. 110–126. DOI: <https://doi.org/10.1016/j.dsr.2013.10.007>. URL: <http://www.sciencedirect.com/science/article/pii/S0967063713002197>.

- Von Appen, Wilken-Jon, Dana Mastropole, Robert S. Pickart, Héðinn Valdimarsson, Steingrímur Jónsson, and James B. Girton (2017). "On the Nature of the Mesoscale Variability in Denmark Strait". In: *Journal of Physical Oceanography* 47.3, pp. 567–582. DOI: 10.1175/JPO-D-16-0127.1. URL: <https://doi.org/10.1175/JPO-D-16-0127.1>.
- Weiss, John (1991). "The dynamics of enstrophy transfer in two-dimensional hydrodynamics". In: *Physica D: Nonlinear Phenomena* 48.2, pp. 273–294. ISSN: 0167-2789. DOI: 10.1016/0167-2789(91)90088-Q. URL: <http://www.sciencedirect.com/science/article/pii/016727899190088Q>.
- Whitehead, J. A. (1998). "Topographic control of oceanic flows in deep passages and straits". In: *Reviews of Geophysics* 36.3, pp. 423–440. DOI: 10.1029/98RG01014. URL: <https://agupubs.onlinelibrary.wiley.com/doi/abs/10.1029/98RG01014>.
- Whitehead, John A., Melvin E. Stern, Glenn R. Flierl, and Barry A. Klinger (1990). "Experimental observations of baroclinic eddies on a sloping bottom". In: *Journal of Geophysical Research: Oceans* 95.C6, pp. 9585–9610. DOI: 10.1029/JC095iC06p09585. URL: <https://agupubs.onlinelibrary.wiley.com/doi/abs/10.1029/JC095iC06p09585>.
- Wilkenskjeld, Stiig and Detlef Quadfasel (2005). "Response of the Greenland-Scotland overflow to changing deep water supply from the Arctic Mediterranean". In: *Geophysical Research Letters* 32.21. DOI: 10.1029/2005GL024140. URL: <https://agupubs.onlinelibrary.wiley.com/doi/abs/10.1029/2005GL024140>.
- Wilks, D. S. (2016). "The Stippling Shows Statistically Significant Grid Points": How Research Results are Routinely Overstated and Overinterpreted, and What to Do about It". In: *Bulletin of the American Meteorological Society* 97.12, pp. 2263–2273. ISSN: 00030007. DOI: 10.1175/BAMS-D-15-00267.1. URL: <https://doi.org/10.1175/BAMS-D-15-00267.1>.

Mattia Almansì

CURRICULUM VITAE

March 2020

🌐 malmans2.github.io | 🌐 malmans2 | 🐦 @MattiaAlmansì

✉️ almansì.mattia@gmail.com

Employment

National Oceanography Centre

OCEAN MODELLER

Southampton, UK

April 2020 –

Academic Education

Johns Hopkins University

PH.D. IN PHYSICAL OCEANOGRAPHY

- Thesis title: Denmark Strait Ocean Circulation Variability
- Advisor: Prof. Thomas W. N. HAINE
- Conferral Date: May 21, 2020

Baltimore, USA

2015 – 2020

Johns Hopkins University

M.A. IN EARTH AND PLANETARY SCIENCES

- Committee: Profs. T. W. N. HAINE, A. GNANADESIKAN, D. W. WAUGH

Baltimore, USA

2016

University of Genoa

M.SC. IN MARINE SCIENCES

- Thesis title: Dynamics and Dispersion Around a Rectangular Headland
- Advisor: Dr. Marcello G. MAGALDI
- Grade: 110/110 cum laude

Genoa, Italy

2014

University of Genoa

B.SC. IN ENVIRONMENTAL SCIENCES

Genoa, Italy

2012

Specialized Education

2019	Teaching Academy , Johns Hopkins University	Baltimore, USA
2019	Big Data Visualization Hackathon , IDIES	Baltimore, USA
2016, 2017	FAMOS School , FAMOS	Woods Hole, USA
2016	FDSE Summer School , University of Cambridge & École Polytechnique	Cambridge, UK
2012	ERASMUS Exchange Program , University of Cádiz	Cádiz, Spain

Teaching Experience

2019	Introductory Oceanography , Apprentice Teacher	Johns Hopkins University
2018	Planning the Power System of the Future , Invited Speaker	Johns Hopkins University
2017	Oceans and Atmospheres , Teaching Assistant	Johns Hopkins University
2017	Climate Change: Science and Policy , Teaching Assistant	Johns Hopkins University

Field Experience

2018	Iceland-Greenland Seas Project (IGP) , Iceland-Greenland Seas	Alliance NATO Research Vessel
2014	ICHNUSSA , Western Mediterranean	Urania Research Vessel

Honors & Awards

- 2018 **George S. Benton Graduate Student Award**, Johns Hopkins University
- 2017 **FAMOS Travel Support**, FAMOS
- 2017 **ASOF-ISSG Travel Support**, WRCP - CliC
- 2015 – 2020 **E&PS Fellowship**, Johns Hopkins University
- 2014 **Master's Thesis Award (“Dignità di Stampa”)**, University of Genoa
- 2011 **ERASMUS Scholarship**, European Commission

Publications

Peer-reviewed

- 6 EVOLUTION OF DENMARK STRAIT OVERFLOW CYCLONES AND THEIR RELATIONSHIP TO OVERFLOW SURGES 2020
Almansi, Mattia and Haine, Thomas W. N. and Gelderloos, Renske and Pickart, Robert S. *Geophys. Res. Lett.*
<https://doi.org/10.1029/2019GL086759>
- 5 OCEANSPY: A PYTHON PACKAGE TO FACILITATE OCEAN MODEL DATA ANALYSIS AND VISUALIZATION 2019
Almansi, Mattia and Gelderloos, Renske and Haine, Thomas W. N. and Saberi, Atousa and Siddiqui, Ali H. *J. Open Source Software*
<https://doi.org/10.21105/joss.01506>
- 4 THE ICELAND GREENLAND SEAS PROJECT 2019
Renfrew, I. A. and Pickart, R. S. and Våge, K. and Moore, G. W. K. and Bracegirdle, T. J. and Elvidge, A. D. and Jeansson, E. and Lachlan-Cope, T. and McRaven, L.T. and Papritz, L. and Reuder, J. and Sodemann, H. and Terpstra, A. and Waterman, S. and Valdimarsson, H. and Weiss, A. and Almansi, M. and Bahr, F. and Brakstad, A. and Barrell, C. and Brooke, J. K. and Brooks, B.J. and Brooks, I. M. and Brooks, M. E. and Bruvik, E. M. and Duscha, C. and Fer, I. and Golid, H. M. and Hallerstig, M. and Hessevik, I. and Huang, J. and Houghton, L. and Jónsson, S. and Jonassen, M. and Jackson, K. and Kvalsund, K. and Kolstad, E. W. and Konstali, K. and Kristiansen, J. and Ladkin, R. and Lin, P. and Macrander, A. and Mitchell, A. and Olafsson, H. and Pacini, A. and Payne, C. and Palmason, B. and Pérez-Hernández, M. D. and Peterson, A. K. and Petersen, G. N. and Pisareva, M. N. and Pope, J. O. and Seidl, A. and Semper, S. and Sergeev, D. and Skjelsvik, S. and Søiland, H. and Smith, D. and Spall, M. A. and Spengler, T. and Touzeau, A. and Tupper, G. and Weng, Y. and Williams, K. D. and Yang, X. and Zhou, S. *Bull. Amer. Meteor. Soc.*
<https://doi.org/10.1175/BAMS-D-18-0217.1>
- 3 ATLANTIC-ORIGIN OVERFLOW WATER IN THE EAST GREENLAND CURRENT 2019
Håvik, Lisbeth and Almansi, Mattia and Våge, Kjetil and Haine, Thomas W. N. *J. Phys. Oceanogr.*
<https://doi.org/10.1175/JPO-D-18-0216.1>
- 2 FRONTOGENESIS AND VARIABILITY IN DENMARK STRAIT AND ITS INFLUENCE ON OVERFLOW WATER 2019
Spall, Michael A. and Pickart, Robert S. and Lin, Peigen and Appen, Wilken-Jon von and Mastropole, Dana and Valdimarsson, H. and Haine, Thomas W. N. and Almansi, Mattia *J. Phys. Oceanogr.*
<https://doi.org/10.1175/JPO-D-19-0053.1>
- 1 HIGH-FREQUENCY VARIABILITY IN THE CIRCULATION AND HYDROGRAPHY OF THE DENMARK STRAIT OVERFLOW FROM A HIGH-RESOLUTION NUMERICAL MODEL 2017
Almansi, Mattia and Haine, Thomas W. N. and Pickart, Robert S. and Magaldi, Marcello G. and Gelderloos, Renske and Mastropole, Dana *J. Phys. Oceanogr.*
<https://doi.org/10.1175/JPO-D-17-0129.1>

PhD Thesis

- DENMARK STRAIT OCEAN CIRCULATION VARIABILITY 2020
Almansi, M. *Johns Hopkins University*

Master's Thesis

- DYNAMICS AND DISPERSION AROUND A RECTANGULAR HEADLAND 2014
Almansi, M. *University of Genoa*

Presentations

Invited Talks

- 2019 **ESIP**, Interoperability and Technology *Tech Dive Webinar Series*
- 2018 **CMCC**, Ocean Modelling and Data Assimilation Division *Bologna, Italy*
- 2017 **TRR 181**, Institute of Oceanography, University of Hamburg *Hamburg, Germany*
- 2015 **CNR-ISMAR**, sez. La Spezia *S.S. di Lerici, Italy*

Conferences

2020	Ocean Sciences Meeting	<i>San Diego, USA</i>
2019	Pangeo Community Meeting	<i>Seattle, USA</i>
2019	ASOF-ISSG Meeting and Workshop	<i>Copenhagen, Denmark</i>
2019	EGU General Assembly	<i>Vienna, Austria</i>
2018	IDIES Annual Symposium	<i>Baltimore, USA</i>
2018	E&PS 50th Anniversary Symposium	<i>Baltimore, USA</i>
2018	ASOF-ISSG Meeting and Workshop	<i>Paris, France</i>
2018	Ocean Sciences Meeting	<i>Portland, USA</i>
2017	Irminger Sea Regional Science Workshop	<i>Southampton, UK</i>
2017	FAMOS Workshop	<i>Woods Hole, USA</i>
2017	IDIES Annual Symposium	<i>Baltimore, USA</i>
2017	US AMOC Science Team Meeting	<i>Santa Fe, USA</i>
2017	ASOF-ISSG Meeting and Workshop	<i>Sopot, Poland</i>
2016	FAMOS Workshop	<i>Woods Hole, USA</i>